CALCITE PRECIPITATION FROM AQUEOUS SOLUTION: TRANSFORMATION FROM VATERITE AND ROLE OF SOLUTION STOICHIOMETRY

Gernot Nehrke

CALCITE PRECIPITATION FROM AQUEOUS SOLUTION: TRANSFORMATION FROM VATERITE AND ROLE OF SOLUTION STOICHIOMETRY

CALCIET PRECIPITATIE UIT EEN WATERIGE OPLOSSING: DE OMZETTING VAN VATERIET EN DE ROL VAN DE STOICHIOMETRY VAN DE OPLOSSING

(met een samenvatting in het Nederlands)

KALZIT FÄLLUNG AUS WÄSSRIGER LÖSUNG: DIE UMSETZUNG VON VATERIT UND DIE ROLLE DER STÖCHIOMETRIE DER LÖSUNG

(mit einer Zusammenfassung in deutscher Sprache)

PROEFSCHRIFT

ter verkrijging van de graad van doctor aan de Universiteit Utrecht op gezag van de rector magnificus prof.dr. W.H. Gispen, ingevolge het besluit van het college voor promoties in het openbaar te verdedigen op maandag 29 januari 2007 des ochtends te 10.30 uur

door

Gernot Nehrke

geboren op 14 september 1971 te Iserlohn, Duitsland

Promotor: prof. dr. P. Van Cappellen

Cover: Calcite crystals formed on vaterite framboid (now dissolved)

What we know is a mere droplet;
what we don't know, an ocean.

- Isaac Newton

Contents

1 General Introduction

1.1 The Carbon Cycle

Carbon dioxide (CO_2) present in our atmosphere absorbs the infrared (IR) radiation emitted by the Earth but is transparent to incoming solar radiation. The absorbed IR radiation increases the molecular vibration of the CO_2 molecule, causing a warming of the atmosphere. Due to the analogy to a greenhouse, where the glass of the greenhouse is transparent for the visible light, but blocks the IR radiation emitted from inside the greenhouse, CO_2 is termed a "greenhouse gas". The burning of fossil fuels and deforestation associated with the "industrial revolution" has led to an increase of atmospheric carbon dioxide (CO_2) by 30 %, since the late nineteenth century (Houghton et al., 2001). This has caused heated debates on how rising CO_2 concentrations, human activities and our climate are interrelated. In order to understand how the anthropogenically triggered increase in atmospheric CO_2 can change our climate, a solid understanding of the processes that effect atmospheric CO_2 and the time scales over which they occur is necessary.

Atmospheric CO_2 is an important but minor reservoir in the carbon (C) cycle. Carbon is cycled between the biosphere, geosphere, atmosphere and hydrosphere (Figure 1.1). The time scales on which the biological and geological processes occur are very different. Whereas biological processes operate on short time scales (days

to hundreds of years), geological processes operate on much longer time scales (millions of years).
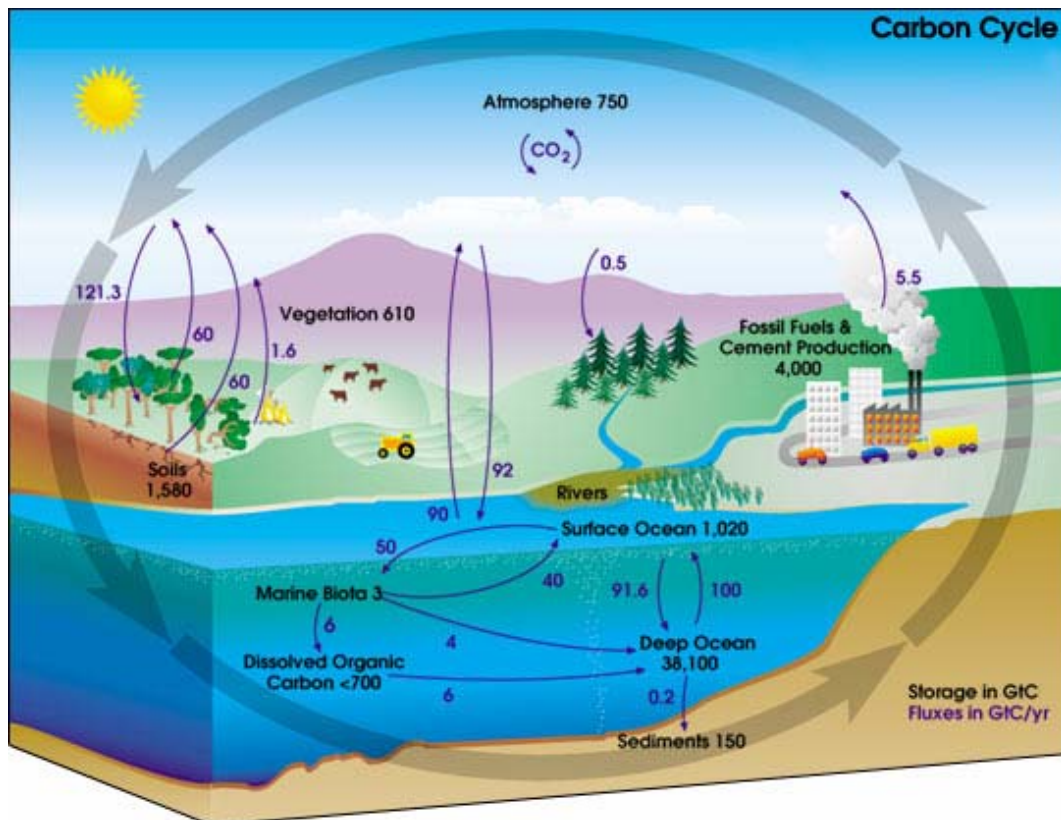
Figure 1.1: Illustration of the global carbon cycle showing the fluxes between ocean, biosphere, and atmosphere (in giga tons (Gt) C per year), as well as the different C reservoirs (in Gt). (Source: http://earthobservatory.nasa.gov /Library/CarbonCycle/Images/carbon_cycle_diagram.jpg)

Geology

To understand the geological component of the C cycle, it is necessary to go back a few billion years in time, more precisely ~4.5 billion years. That is, when our Solar System came into existence, originating from a cloud of interstellar gas and dust that collapsed under its own gravity. Earth formed when dust particles collided with each other, merging into larger particles which subsequently joined into pebble-sized rocks and so on (Halliday, 2006). During this process heat was produced and the early Earth was probably molten and the densest material migrated toward the center of the planet, while lighter materials floated toward the surface, creating the Earth's crust. The latter consists of the oceanic (denser) and the continental (lighter) crust, floating on the mantle (which has the highest density of all three). Since carbon represents the fourth most abundant element in the Universe, it was also present when Earth was formed. A small part of this C was released to the atmosphere in the form of CO_2, together with water (H_2O) vapor and sulfur dioxide (SO_2), when the

Earth cooled down. Since the earliest times, carbonic acid (a weak acid derived from the reaction of H_2O and CO_2) has been reacting with minerals (weathering) followed by the transport of the reaction products, including calcium (Ca) and magnesium (Mg), to the oceans (erosion). Some of the carbonic acid reacts with Ca or Mg to form carbonates, which eventually settle at the bottom of the oceans.

Due to convective motion of the mantle, "new" oceanic crust is formed at the oceanic ridges and drawn into the mantle at subduction zones; a process known as "plate tectonics". Consequently carbonates buried in marine sediments are drawn into the mantle at subduction zones. The CO_2 is then released back to the atmosphere during volcanic eruptions. This "geologic" carbon cycle balances weathering, subduction, and volcanism over time periods of hundreds of millions of years (Figure 1.2). However, since ~3.5 billion years ago this cycle is influenced by another major event, the appearance of life.
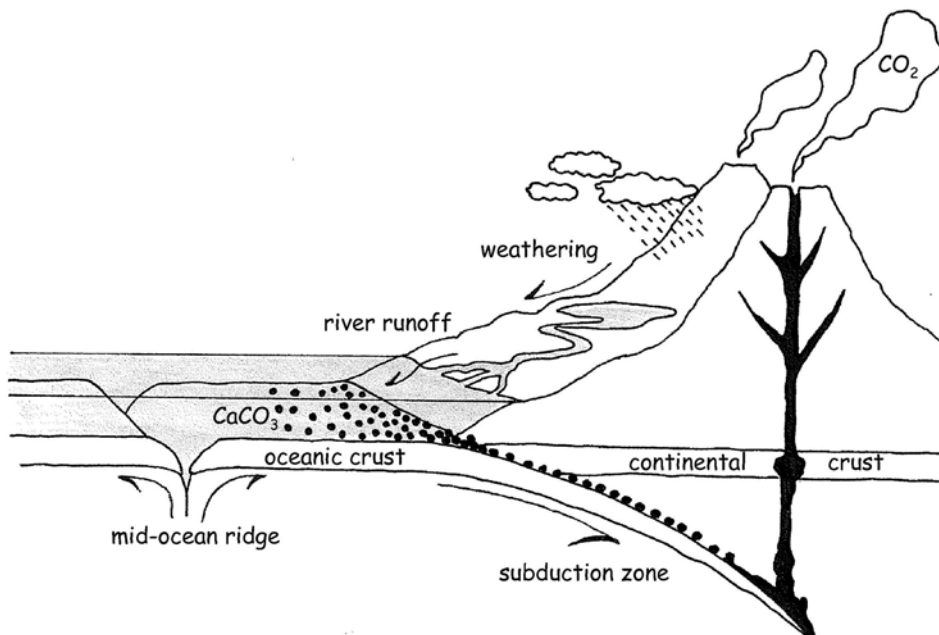
Figure 1.2: Geological carbon cycle. Calcium, together with other weathering products is titrated into the ocean, where it combines with carbonate to form $CaCO_3$. At the subduction zone the oceanic crust, together with its sediments, is drawn into the mantle. Volcanism associated with the processes at a subduction zone releases CO_2 to the atmosphere (Illustration courtesy Karina Kaczmarek).

Biology

About 100 million years after the first fossil evidence of life on Earth, photosynthetic organisms had already evolved (Falkowski and Raven, 1997). These ancestors of modern plants used the radiant energy of the sun to convert simple

inorganic molecules – CO_2 and H_2O – into complex organic molecules, that is, photosynthesis (Figure 1.3).
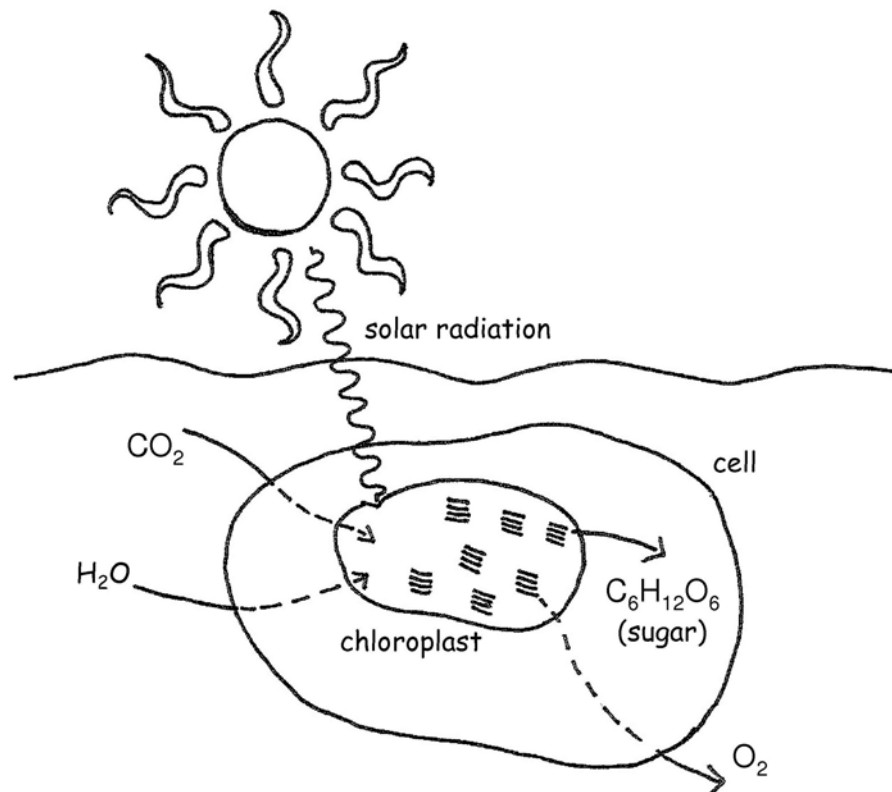
Figure 1.3: Photosynthesis; Sugar and O_2 are produced within a chloroplast from CO_2, H_2O, and the radiant energy from the sun (Illustration courtesy Karina Kaczmarek).

In a series of reactions termed carbon fixation, CO_2 molecules are converted into carbohydrates, which in turn are either converted into other organic molecules, e.g. fatty acids and amino acids, or broken down by the oxygen-utilizing process known as respiration, yielding the energy for cellular metabolism. The oxygen on which aerobic organisms depend is released as a waste product during photosynthesis. During respiration, CO_2 is cleaved from the organic food molecules and returned to the atmosphere and (or) hydrosphere. Not all organic carbon is oxidized back to CO_2 in the course of a plant's life, however. Dead body parts of plants and other organisms become part of the soil organic matter, or sink to the ocean floors where, in many cases, they are consumed by decomposers – small invertebrates, bacteria and fungi – which thereby release CO_2. However, some carbon is removed from the atmosphere/hydrosphere by preservation and burial of organic matter in marine sediments. On a global scale, for the present day situation it is estimated that in the modern ocean burial fluxes of inorganic C (mainly as $CaCO_3$) and organic C are of the same order of magnitude (Sundquist and Visser, 2005).

Biogeochemistry

Even though geological and biological processes in the C cycle occur on significantly different time scales, they are linked to each other. A good example is $CaCO_3$, produced by marine organisms such as coccolithophores and foraminifera (Figure 1.4), which accumulated on the sea floor some time in the geological past, and was later uplifted on land by geological processes, and currently exposed to weathering. The formation of the $CaCO_3$ shells occurs within hours to days, the accumulation and preservation in marine sediments proceeds on time spans of thousands of years, while the formation of mountains (orogenesis) requires millions of years. The previously described scenario becomes a cycle, when the carbonated deposits on land are subject to weathering and erosion, and the carbonate is released back to the ocean, again a process which takes hundreds of thousands of years.
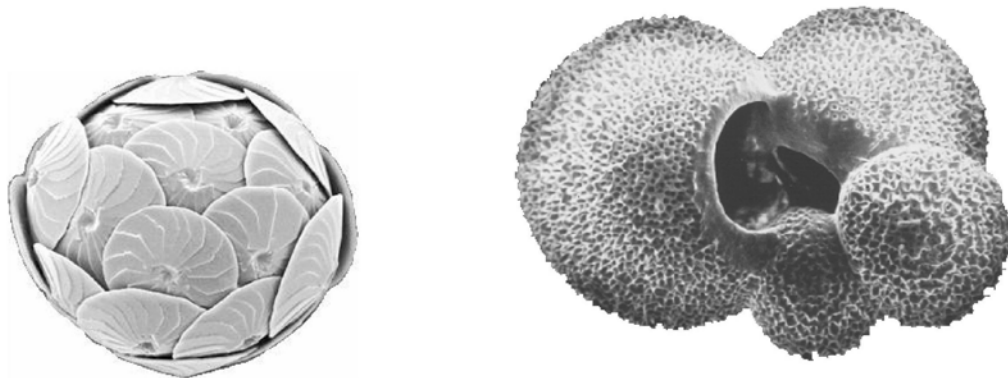
Figure 1.4: The left micrograph shows a coccosphere of the coccolithophore *Calcidiscus leptoporus* made of calcite. The right micrograph shows the test of the planktic foraminifera *Globigerina bulloides* also made of calcite.

If organic remains of plants and/or animals, rather than $CaCO_3$, are buried, coal and oil (containing mainly C) may form. Once buried in the sediment, they undergo the previously described geological processes, leading to a release of the C over very long time spans (millions of years). Due to the burning of fossil fuels by humans, the time span in which C is released to the atmosphere (as CO_2) is drastically decreased in comparison to natural recycling. At the moment, about 5.5 Gt (giga tons) (Houghton et al., 2001) C are released to the atmosphere per year. Some

of this C (~3.3 Gt) remains in the atmosphere as CO_2, where it contributes to the greenhouse effect. The remaining ~2.2 Gt C dissolves in the oceans where it forms carbonic acid, leading to an acidification of the oceans. In order to predict the impact of the artificially increased C cycling in the ocean-atmosphere system, it is necessary to understand how the different geological and biological processes interact. To do so, it is necessary to understand the various underlying processes. Since $CaCO_3$ represents the largest C reservoir, the fundamental processes responsible for the formation and dissolution of $CaCO_3$ will be discussed.

1.2 Calcium Carbonate

Inorganic processes

The partial pressure of CO_2 (pCO_2) of the atmosphere is determined by the carbonate chemistry of the oceans (because they contain 60 times more carbon than the atmosphere). The ocean carbonate chemistry, on the other hand, is determined by weathering of the continents and "titration" of the ocean with weathering products. Since limestone (mainly $CaCO_3$) is ubiquitous, its precipitation and dissolution affect the physico-chemical conditions of many aqueous environments, including groundwater, rivers, lakes and the oceans. Furthermore, because of their high reactivity (dissolution rates of carbonate minerals are much higher than those of most other minerals, mainly silicates), carbonate minerals affect their environment even if only present in relatively small amounts.

The majority of carbonates is not precipitated inorganically but formed by marine calcifying organisms (Sundquist and Visser, 2005). Inorganic precipitation of $CaCO_3$ only occurs under special conditions like calc-sinter formation at hot springs and dripstone formation in some caves. Consequently the inorganic process of $CaCO_3$ dissolution has received more attention from environmental geochemists than inorganic $CaCO_3$ precipitation. However, inorganically precipitated $CaCO_3$ represents an important industrial product, and there is an increased interest in a fundamental understanding of the processes operative during the precipitation of $CaCO_3$. During the last three decades, largely thanks to the development of new micro-focusing methods like Atomic Force Microscopy (AFM), the understanding of $CaCO_3$ formation at the molecular level has advanced significantly. A good example is the

incorporation of divalent cations into calcite. In the early 1980s, the incorporation of trace elements was shown to be a function of growth rate (Lorens, 1981). The development in AFM made it possible to image the surface of growing crystals. Figure 1.5a, shows a so-called growth spiral (or growth hillock), which developed on a growing calcite crystal (for a discussion of crystal growth, see *Chapter 2*). Microscale chemical analysis shows that trace element incorporation varies depending on the crystallographic orientation relative to the growth hillock (Figure 1.5b).
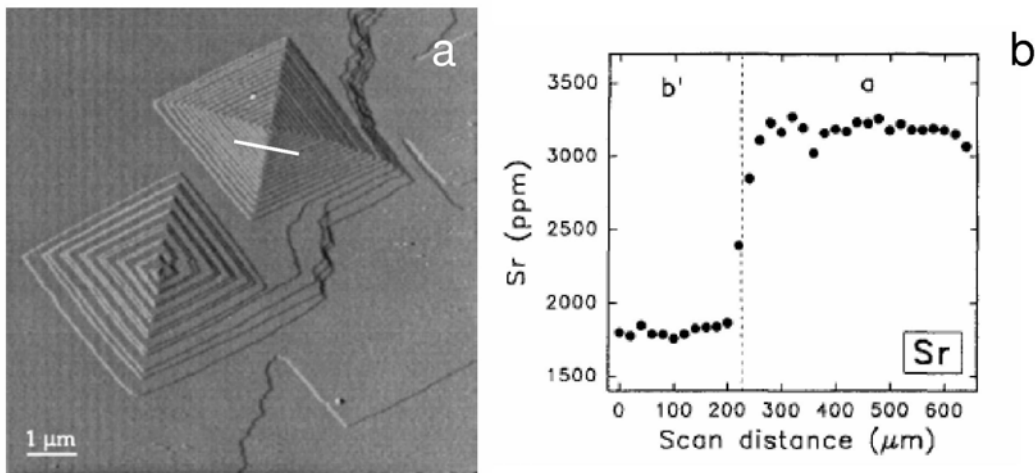
Figure 1.5: The micrograph on the left shows two calcite growth hillocks (from Teng et al., 1999). The Sr concentration profile measured by means of an electron probe across a growth hillock (as indicated by the white line in micrograph (a), is shown in the right plot (from Reeder, 1996).

Many $CaCO_3$ precipitation experiments are conducted as so-called seeded experiments, in which existing calcite crystals are introduced in a supersaturated solution, causing the crystals to grow, like in the AFM study described before. This type of experiments is a powerful tool to elucidate processes occurring at the crystal surface, such as trace element incorporation during calcite growth. However, in many cases it is important to understand the process of calcite nucleation, a process which precedes crystal growth. In unseeded calcite growth experiments, the physico-chemical conditions are often altered beyond the range typically observed in the natural environment. Before a calcite crystal can nucleate from a supersaturated solution, a critical supersaturation has to be reached (see *Chapter 2*). However, in such supersaturated solution it is possible that a precursor, for instance amorphous calcium carbonate (ACC) or vaterite, forms first, which thereupon transforms into calcite. How trace element incorporation into a calcite crystal that formed via a

precursor is altered is not known. Preliminary data on Ca isotope fractionation (a process which, like trace element incorporation, depends on the calcite growth rate) show that calcite formed via the transformation of vaterite exhibits an isotope fractionation reflecting the growth rate of the vaterite precursor, not that of the final products, calcite. The interpretation of the measured fractionation data would remain highly speculative without a knowledge of the transformation pathway and kinetics of the vaterite to calcite transformation.

Biological processes

Next to the major elements Ca, C, and O, many other elements present in seawater are incorporated into $CaCO_3$ precipitated by marine calcifying organisms such as foraminifera. The amounts in which these other elements, mainly divalent cations, are incorporated are very minor relative to Ca. For some organisms it has been shown that the amount of a given element incorporated into the $CaCO_3$ they precipitate, depends linearly on the concentration of the specific element in seawater. For other elements a correlation between temperature (*T*) and trace element incorporation has been found. Based on these observations, the amount of trace elements in the $CaCO_3$ precipitated by specific organisms can be used as so-called paleo-proxy for the reconstruction of past environmental conditions. Trace element incorporation has been shown experimentally to vary significantly between species. The problem associated with the large amount of empirical observations is that the impact of changing environmental parameters, e.g. pH, *T* and ionic strength, on the proxy are difficult to assess. To evaluate the robustness of proxies a more process-based understanding of trace element incorporation during biomineralization of $CaCO_3$ is needed.

This requires one to separate the purely inorganic processes from the biological imprint, the so-called "vital effect". In other words, an "inorganic baseline" is needed, describing how the purely inorganic system would behave, without any biological "interferences". To some extend it is not possible to separate the inorganic from the biological processes since they are partly interrelated. Some organisms for example precipitate a precursor phase which transforms thereupon into calcite. As mentioned before, this is well known for purely inorganic systems that are highly

supersaturated with respect to calcite. Nevertheless, it is not possible to conclude that the solution within the vesicle of a cell (the site of nucleation) is highly supersaturated with respect to calcite if a precursor phase precipitates first, since the nucleation within the vesicle is most likely initiated on an organic matrix, which influences the nucleation process. However, as most data on inorganic calcite precipitation where collected with a different question in mind, little is known on inorganic calcite precipitation under the physico-chemical conditions relevant to intracellular biomineralization. Therefore it is not possible yet to ascertain which processes in the biomineralization of calcite are determined by cell physiological processes and which are not. If one wants to find out if trace element incorporation into biogenic calcite can be explained solely based on inorganic processes, it is necessary to know if physico-chemical parameters like the $[Ca^{2+}]$ to $[CO_3^{2-}]$ solution ratio, which at the site of calcification may differ from those present in most natural aqueous environments, alters the trace element incorporation.

1.3 Outline Thesis

One aim of this thesis was to study the transformation of vaterite into calcite, in order to better characterize a precursor-based reaction pathway for calcite formation. This system forms the basis to further investigate trace element incorporation and Ca isotope fractionation into calcite via a precursor phase. *Chapter 4* describes the formation and properties of framboidal vaterite aggregates, whereas *Chapter 5* describes the kinetics of vaterite transformation into calcite. In biological systems, the $[Ca^{2+}]$ to $[CO_3^{2-}]$ ratio at the site of calcification may differ from the ratio present in the surrounding aqueous environment. To shed light on the question if the $[Ca^{2+}]$ to $[CO_3^{2-}]$ ratio modifies the calcite precipitation rate and trace element incorporation, calcite growth experiments were performed in the presence of Sr (*Chapter 6*). As background, a general introduction on crystal growth and nucleation is provided in *Chapter 2*, supplemented by a detailed description of the $CaCO_3$ system and its polymorphs in *Chapter 3.*

2 Nucleation and Growth of Crystals from Solution

2.1 Introduction

Two steps are required to form a crystal from solution. The first step is the formation of a nucleus; the second is the growth of this nucleus (from this moment on called a crystal). The basic theory of nucleation and growth is discussed in this chapter. The first part presents the thermodynamics of nucleation and growth, whereas the second part deals with the kinetics of these processes.

2.2 Thermodynamics of Nucleation and Growth

2.2.1 Nucleation

Molecules and ions (referred to as "growth units", GU) in solution continuously form small solid-like clusters. The overall Gibbs free energy of formation (ΔG_t) of these clusters consists of two terms. The first term, the surface free energy (ΔG_s), results from the formation of an interface between the new solid phase and the solution. The second term accounts for the Gibbs free energy accompanying the transfer of GU from the solution into the bulk solid phase (ΔG_l). When the solution is supersaturated with respect to the solid phase, the sum of these two terms reaches a maximum value at a particle size called the critical size. A smaller or sub-critical cluster is called an embryo. When the critical cluster size is reached, the cluster is

called a nucleus. Further growth of the cluster (crystal) decreases the Gibbs energy of the system and hence is a spontaneous process.

The mathematical description of the Gibbs free energy of a cluster is given by (Sawada, 1998):

$$\Delta G_t = \Delta G_l + \Delta G_s \qquad (2.1)$$

The bulk energy term, ΔG_l, is proportional to the number of constituent GU, n. Assuming the formation of a spherical cluster we have

$$\Delta G_l = -\frac{4\pi r^3}{3a^3}\Delta\mu \qquad (2.2)$$

where a is the size of individual solid growth units, r is the radius of the cluster, and $\Delta\mu$ is the difference between the chemical potentials of the GU in solution, μ_{soln}, and in the bulk crystal, μ_{cryst}:

$$\Delta\mu = \mu_{soln} - \mu_{cryst} = kT\ln\left(\frac{c}{c_0}\right) \qquad (2.3)$$

where c refers to the concentration of GU in the solution and c_0 denotes the equilibrium concentration of GU in a saturated solution, that is, c/c_0 corresponds to the degree of supersaturation (S):

$$S = \left(\frac{c}{c_0}\right) \qquad (2.4)$$

The surface Gibbs free energy, ΔG_s, is always a positive value and directly proportional to the cluster surface area:

$$\Delta G_s = \left(\frac{4\pi r^2}{a^2}\right)\gamma \qquad (2.5)$$

in which γ is the surface Gibbs energy per unit area, also known as the surface tension. Consequently, the overall change of the total Gibbs free energy of the cluster is given by

$$\Delta G_t = -\Delta\mu \,(4/3)\pi\, r^3/a^3 + \gamma\,(4\pi\, r^2/a^2) \tag{2.6}$$

In Figure 2.1, ΔG_l, ΔG_s and ΔG_t are plotted as a function of the cluster radius, r, for a supersaturated solution. As seen in the figure, ΔG_t is characterised by a maximum. The critical size of the particle, r_{crit}, obeys dΔG_t/dr = 0 and is given by

$$r_{crit} = 2\gamma\, a\,/\,\Delta\mu\ = 2\gamma\, a\,/\,kT\ln\!\left(\frac{c}{c_0}\right) \tag{2.7}$$
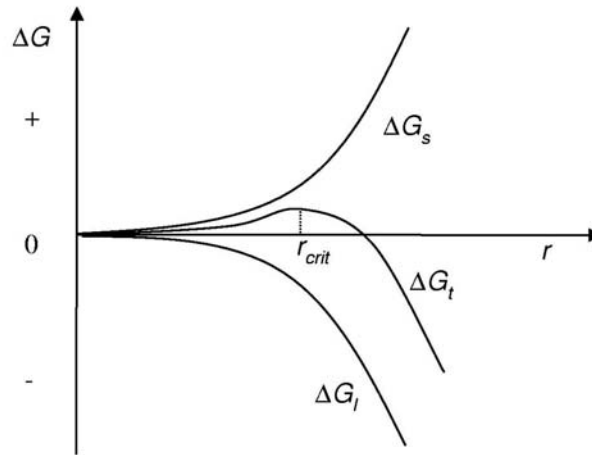
Figure 2.1: Lattice free energy ΔG_l, surface free energy ΔG_s, and overall Gibbs free energy ΔG_t of formation of a cluster, as a function of the radius of the cluster.

The critical activation energy of nucleation can be calculated by inserting Equation (2.7) into Equation (2.6). It can then be expressed as a function of S:

$$\Delta G_{crit} = \frac{16\pi\,\gamma^{\,3}}{3[kT\ln(S)]^2} \tag{2.8}$$

It follows from Equations (2.7) and (2.8) that both r_{crit} and ΔG_{crit} decrease with increasing supersaturation (Figure 2.2).
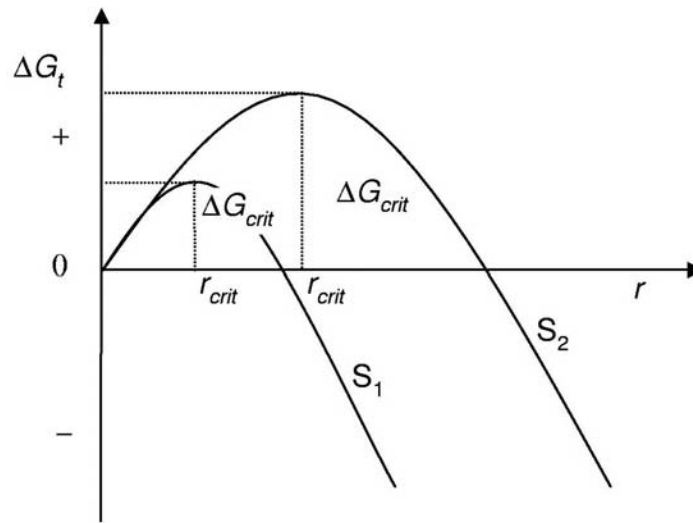
Figure 2.2: ΔG_t versus the cluster radius, r, for different supersaturation, S, where $S_1 > S_2$.

2.2.2 Crystal Growth

A crystal grows by the attachment of growth units (GU) to the cluster surface. Depending on the type of crystal these GU can be ions, atoms or molecules. Kossel (1927) and Stranski (1928) presented a model for a growing crystal surface of a pure ionic crystal (like NaCl). In this model six different surface sites can be distinguished on a crystal surface (Figure 2.3). These sites differ in their potential energy associated with the attachment of GU. Potential energy stored in the lattice bonds lowers the system's Gibbs free energy. As a first order approximation, the strength of bonding at different sites can be calculated as $u = \varphi_l \, e^2 / r$, where e is the ionic charge, r is the distance between neighboring ions, and φ_l is a numerical constant that is analogous to the Madelung constant α. The Madelung constant is a dimensionless constant determined solely by the geometrical arrangement of point charges. It has the same value for all compounds of the same structure type (in the case of NaCl: $\alpha = 1.748$). Values for φ_l are given in Table 2.1.

Table 2.1 The value of φ_l for the attachment of GU to different surface sites of the NaCl-structure (Kleber et al., 1990). The values of the subscripts correspond to the surface sites identified in Figure 2.3.

φ_1	φ_2	φ_3	φ_4	φ_5	φ_6
0.8738	0.4941	0.1806	0.2470	0.0903	0.0662

Attachment of an ion to site »1« is energetically most favourable. This site is known as a "kink site" (KiS). The suggested mechanism for the deposition of a GU on a crystal surface includes the following steps: (i) transport of the GU to the crystal surface and its adsorption onto the surface, (ii) diffusion to a step (StS) site, (iii) diffusion to and incorporation at KiS. If no KiS site is present, position »2« will be the most favoured position and a new row of GU will start to grow along the edge. This crystal growth mechanism results in the advancement of edges over the surface of the crystal. Strictly speaking, the surface structure shown in Figure 2.3 and the growth mechanism described only apply to pure ionic crystals with a cubic lattice structure. For other structures and types of bonding the model requires modifications (Kleber et al., 1990).
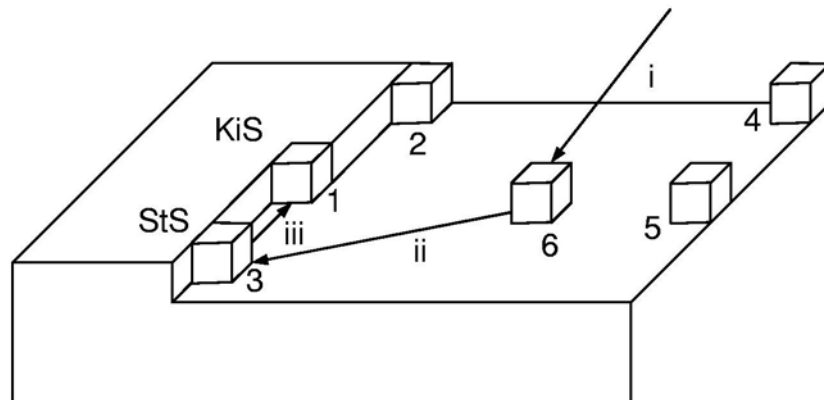
Figure 2.3: Surface sites on a cubic crystal (»Kossel-crystal«) (modified after Sawada, 1998) and possible steps in crystal growth (i, ii, iii). Positions 1 to 6 are characterized by different site energies, corresponding to the different values of φ_l (Table 1). Site 1 is a so-called kink site (KiS), site 3 a step site (StS).

Incorporation of GU into the surface lattice shown in Figure 2.3 will ultimately lead to an atomically flat surface. Further growth then requires the formation of a new layer. The potential energy gained by attaching a single GU to a flat crystal surface (position 6 in Figure 2.3) is relatively low. Therefore, a two-dimensional (2D) cluster island disc must form on the surface. This cluster has to reach a critical cluster radius before it can spontaneously grow ($\Delta G_t < 0$). This process can be compared with the previously described formation of a three-dimensional nucleus from homogeneous

solution: it is called 2D nucleation or heterogeneous nucleation. The overall free energy for the formation of the 2D cluster ΔG_t is given by:

$$\Delta G_t = -\Delta\mu \; r^2/a^2 \; + \gamma \; (2\pi \; r/\; a) \tag{2.9}$$

where the first term corresponds to the Gibbs free energy of formation of the cluster lattice and the second term is the excess energy due to the creation of new mineral-solution interface. The change of ΔG_t with r follows a similar curve to that of three-dimensional nucleation (Figure 2.1). For kinetic reasons, 2D nucleation needs a relatively high degree of supersaturation (see detailed discussion in the following section).

Thus far we considered a crystal as a perfect three-dimensional periodic repetition of atoms. This is an idealized situation. In reality a perfect crystal does not exist. For example an ultra-pure crystal, with a purity of 99.999 %, contains 10^{18} foreign atoms per cm^3, out of a total of 10^{23} atoms per cm^3. The crystal lattice is distorted by these impurities. There are a number of different types of imperfections possible in the crystal structure. For a detailed account on this issue the reader is referred to, e.g., Kleber (1991) and Putnis (1995).

2.3 Kinetics of Nucleation and Growth

2.3.1 Nucleation

In the following discussion, it is important to recall that molecular velocities are on the order of 1 km/s, and atomic dimensions are about 10^{-10} m. The fastest rearrangement of atoms thus requires at least

$$10^{-10} \; m/(1 \; km/s) = (10^{-10} \; m)/10^3 \; m/s) = 10^{-13} \; s \tag{2.10}$$

In other words, the characteristic time scale of a molecular event is on the order of 10^{-13} s. Following Nielsen (1964), let us consider the "equilibrium" concentration of embryos as a function of the degree of supersaturation, S (illustrated in Figure 2.4). At S =10, the concentration of embryos is 10^{-35} clusters cm^{-3} (of size n = 115 GU),

that is one cluster in 10^{35} cm^3 (or 10^7 times the earth's volume). During 10^{-13} s, the possibility of finding a critical embryo is thus renewed every 10^{35} / 10^{13} = 10^{22} s (3 x 10^{14} years). Under these circumstances a solution is metastable, but for practical considerations it will remain stable. If S is increased by a factor of 2 (S = 20), the critical cluster size becomes n = 52 and c = 10^{-12} molecules/ions per cm^3. In this case, per cm^3, nuclei form approximately 10^{13} /10^{12} = 10 times per second.
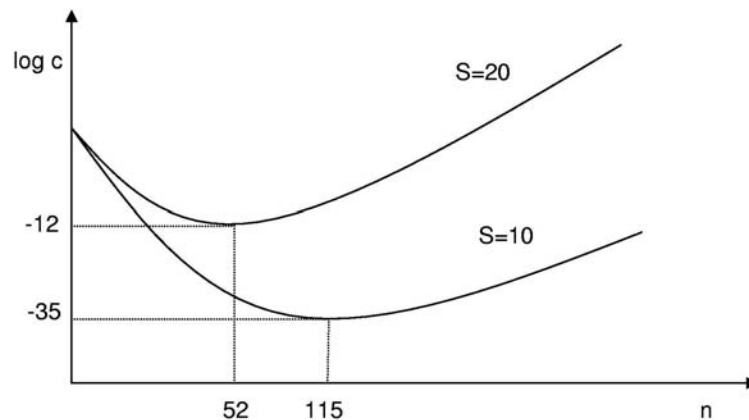
Figure 2.4: The equilibrium concentration (in molecules/ions per cm^3) of embryos as a function of the particle size at S = 10 and S = 20. The following conditions apply to the embryos: shape factor β = 40 (this is a factor taking into account the cluster shape; for example β for a sphere = 16.7, for a cube = 32 and for a regular tetrahedron = 55.8 (for more details see Nielsen, 1964), surface tension σ = 5x10^{-3} mJ/m^2 and volume v = 10^{-22} cm^3.

This example illustrates that a relatively small change in S may create a large increase in the probability to produce critical nuclei and, therefore, the rate of nucleation.

2.3.2 Precursors

Some chemical compounds can precipitate as structurally different solid phases (*polymorphs*). If different polymorphs exist for a chemical compound, the most soluble phase (also called precursor) often precipitates first, and then transforms via other (metastable) phases into the final, (most stable) phase (Figure 2.5). This was first proposed by Ostwald in 1897: *"If the supersaturated state has been spontaneously removed then, instead of a solid phase which is under the given*

conditions thermodynamically stable, a less stable phase will be formed". This is also known as the Ostwald Step Rule (OSR) or (Ostwald) Rule of Stages.
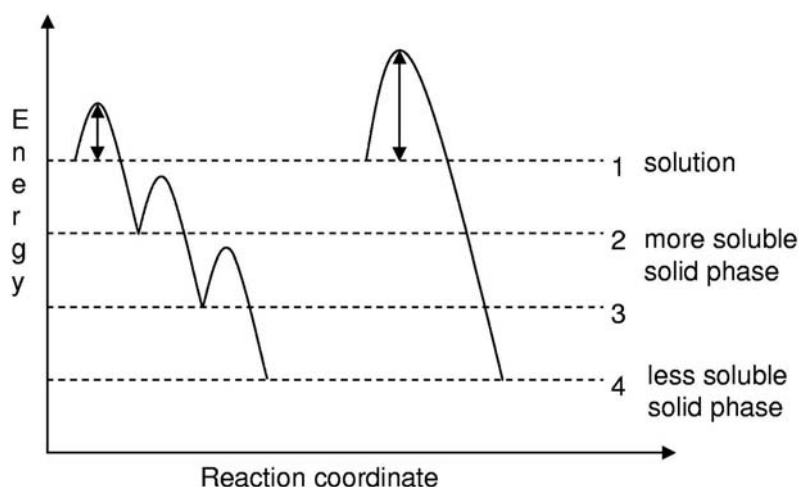
Figure 2.5: Illustration of the OSR. The transformation via a sequence of steps 1 => 2 => 3 => 4 is kinetically more favoured than the direct transformation from 1 to state 4.

Figure 2.5 illustrates the possible pathways of transformation of polymorphs, when large differences in solubility exist between the different phases. In this case the pathway will be more likely from phase 2 via phase 3 to phase 4. In contrast, Figure 2.6 illustrates a situation where the difference in solubility between phase 3 and 4 is very small. Under these circumstances a pathway from phase 2 directly to phase 4 is more likely (pathway B in Figure 2.6).
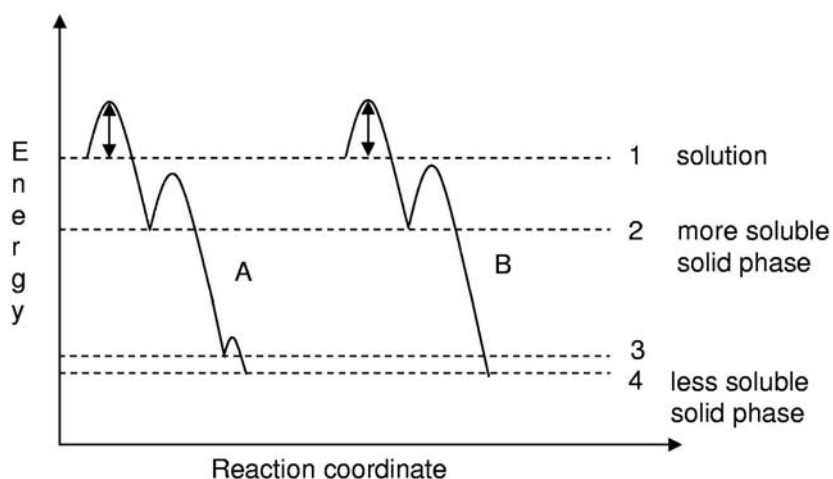
Figure 2.6: Compared to the situation illustrated in Figure 2.5, the difference in solubility of phases 3 and 4 is very small. Under these circumstances pathway B will be more likely than pathway A.

The experimental observation that the system preferentially forms the phase with the fastest precipitation rate, shows that a more soluble phase may be kinetically favoured (Figure 2.5). The mathematical description of this observation (stated in the OSR) is quite difficult. In theory, the nucleation rate depends on the interfacial tension of the nuclei. The interfacial tension of macroscopic crystals can be related to the geometrical shape and surface area of the crystals (Kashchiev, 2000; Nielsen, 1964; Van Cappellen, 1990). A nucleus consists of a small number of GU (10 to 100). For these particles the surface tension probably depends more on their size than on their geometrical shape or surface area. (Nielsen, 1964). The differences in chemical bonding between the GU of the less stable and the more stable phase may account for the difference in surface tension between these phases. For example, most known precursors are hydrated phases (often amorphous). Incomplete dehydration of the GU could lead to significant lower surface tension of the precursor relative to that of the stable phase and, thus, to a faster nucleation rate. This also means that the nucleus size of the precursor is smaller than that of nuclei of the stable phase (Equation (2.7)).

A schematic plot of the free energy of formation of clusters from solution as a function of the number of constituent GU is presented in Figure 2.7. The lower activation energy for nucleation of the more soluble phase derives from its lower solid-solution interfacial tension. This leads to faster precipitation of the most soluble phase (B).
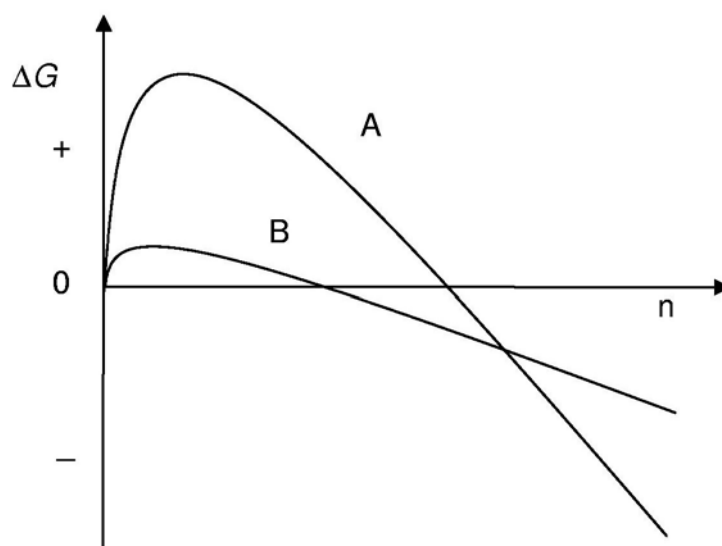
Figure 2.7: Schematic plot of free energy of formation of clusters from solution as a function of the number of constituent GU. Curve A corresponds to the macroscopically stable phase and curve B to the more soluble phase, or precursor phase (from Van Cappellen, 1990).

2.3.3 Crystal Growth

In order to grow a crystal, GU have to be transported to the crystal surface. At the crystal surface the GU may have to dehydrate and rearrange to fit the lattice structure. Thus, crystal growth can be divided into two successive processes: transport through solution and surface reaction. Both of these processes can be growth rate-controlling. The first case is referred to as transport-controlled (*tc*), the second as surface-reaction controlled (*src*).

In *tc* growth, we distinguish between growth controlled by diffusion (transport of matter as a consequence of the thermal motion of the molecules) and by convection (mass movement due to an energetic gradient in the system). Convection-controlled growth has to be considered when particle size is greater than 10µm. For particles < 10µm, convection can be neglected because the velocity of the crystals settling through the solution by normal gravity is very slow (Nielsen, 1964). Surface-controlled growth can be divided into nucleation-controlled (*nc*) and dislocation-controlled (*dic*) growth.
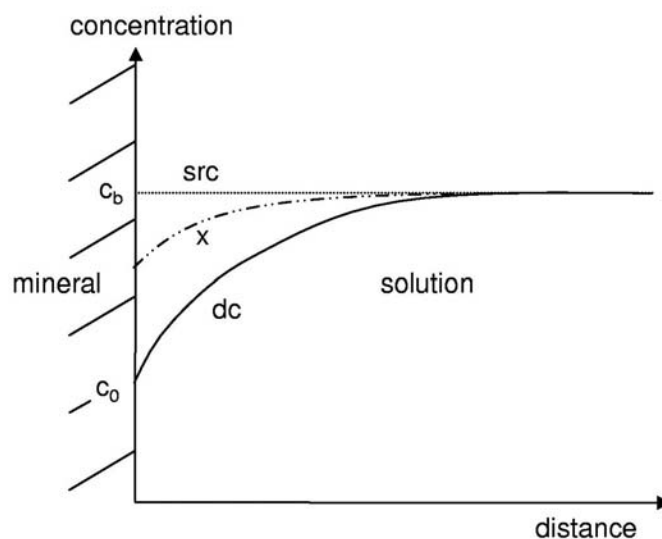
Figure 2.8: Theoretical concentration gradients of GU around a crystal. (dc) Diffusion-controlled growth, (src) surface reaction-controlled growth and (x) mixed diffusion-surface reaction mechanism. The bulk solution and saturation concentration of GU are indicated by c_b and c_0, respectively.

During crystal growth a stationary diffusion concentration field is set up around the crystal. If growth is diffusion-controlled, the concentration at the surface approaches the saturation concentration (solubility). For surface-reaction controlled growth the concentration of GU at the mineral surface approaches the bulk

concentration. This is illustrated in Figure 2.8. The concentration gradients identified as src and dc represents the two end-member cases. Often a combination of both mechanisms controls the growth rate (line x in Figure 2.8).

Different rate laws for crystal growth have been proposed. The following empirical rate law is often used to fit experimental data, especially at high degrees of supersaturation (Kashchiev, 2000; Nielsen, 1964; Stumm, 1992):

$$J = k(S-1)^n \tag{2.11}$$

where J is the linear growth rate (length / time) perpendicular to the crystal surface, and n is an empirical reaction order (not to be confused with the number of GU in a cluster).

The necessity of a critical supersaturation for homogeneous nucleation has already been discussed earlier in this chapter. Similarly, 2D nucleation-controlled crystal growth requires supersaturation in excess of a critical value. Therefore crystal growth via 2D nucleation is not possible at low degrees of supersaturation (Sawada, 1998; Stumm, 1992). In most cases, however, measured growth rates at low S are much faster than predicted by the surface nucleation model (Sawada, 1998).

In 1951, Burton, Cabrera and Frank proposed a model in which a defect, the so-called "screw dislocation", gives rise to a step created at the intersection of the screw dislocation and the crystal surface (also called the BCF model). By attaching GU to this step, the step winds itself around the screw dislocation. Because of the geometric properties of a spiral, the step does not disappear and continuous growth is possible. Under these circumstances 2D nucleation is no longer necessary. This growth mechanism is called "spiral growth" (Figure 2.9), and has been successfully applied to growth from solutions close to saturation (Ogino et al., 1987; Sawada, 1998; Stumm, 1992).
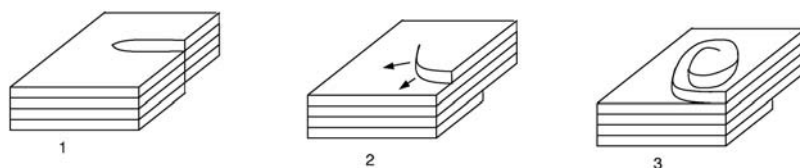
Figure 2.9 Screw dislocation. Due to a lattice defect (1), the formation of a growth spiral (2 and 3) is propagated at the surface of the crystal.

In spiral growth, under conditions of low S, a GU arriving at a step site will be incorporated into the crystal lattice by surface diffusion into a kink site (Figure 2.3). An increase of S will lead to a higher density of kink sites and a higher surface roughness (Sawada, 1998). The growth mechanism then changes into so-called adhesive growth. GU arriving at the surface will be incorporated directly into the lattice without diffusion. A further increase of S will lead to additional formation of amorphous surface precipitates (on details see e.g. Markov, 2003; Nielsen, 1964).

2.4 Mineral Transformation

As described before (Section 2.3.2) some chemical compounds can precipitate as structurally different solid phases (*polymorphs*). The successive processes associated with the solution-mediated transformation of a so-called precursor into a more stable one are: (1) dissolution of the more soluble precursor phase, (2) transport of constitutive ions through the solution, and (3) growth of the less soluble phase. To identify which of these processes is determining the overall transformation rate can be difficult. Rate constants for crystal growth / dissolution have to be determined experimentally and are a function of the ion activity product in the solution. To quantify the interplay between transport, surface reactions, and surface area, a model described by Lasaga (1998), which explicitly accounts for transport processes, will be discussed. As illustrated in Figure 2.10, this model describes the breakdown of mineral B, followed by the transport of the dissolved components over distance L, and the precipitation of the new mineral A.
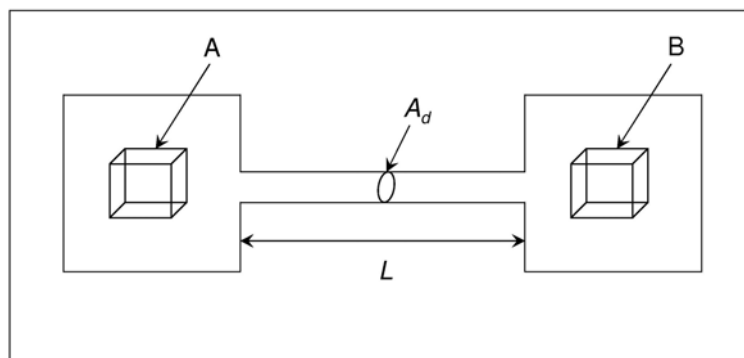
Figure 2.10: Schematic diagram illustrating a simplified model for the breakdown of mineral B, the transport of components along a distance L through a grain boundary network (area A_d), and the growth of mineral A (from Lasaga, 1998).

In the following discussion of the reaction model the following assumptions are made for the sake of simplicity. (1) The solution all around A and B is "stirred" and maintained at uniform concentrations (C_S^A and C_S^B). (2) The transformation process is governed by the transport and reaction of one component (e.g. Ca^{2+}).

The following notation will be used in this discussion:

A:	mineral A
B:	mineral B
A_A and A_B:	surface areas of A and B
C_S^A and C_S^B:	concentrations of the component in the immediate vicinity of A and B
C_{eq}^A and C_{eq}^B:	equilibrium concentrations of the component with respect to A and B
k_A and k_B:	surface reaction rate constants for A and B
R_A and R_B:	surface reaction rates of A and B
L:	distance between A and B
A_d:	cross section of grain boundaries
D:	diffusion coefficient of the component in solution
J:	diffusion flux of the component along the grain boundary
γ_A:	dimensionless variable, $\gamma_A \equiv \dfrac{k_A L}{D A_d} A_A$
γ_B:	dimensionless variable, $\gamma_B \equiv \dfrac{k_B L}{D A_d} A_B$

The surface reaction rates and diffusion flux are given by (Lasaga, 1998):

$$R_A = k_A A_A (C_S^A - C_{eq}^A) \tag{2.12}$$

$$R_B = -k_B A_B (C_{eq}^B - C_S^B) \tag{2.13}$$

$$J = -DA_d \frac{(C_S^B - C_S^A)}{L} \qquad (2.14)$$

After a short transient time, steady state is reached and all the rates become equal (Lasaga, 1998):

$$J = R_A = R_B \qquad (2.15)$$

or

$$DA_d \frac{C_S^B - C_S^A}{L} = k_A A_A (C_S^A - C_{eq}^A) = k_B A_B (C_S^B - C_{eq}^B) . \qquad (2.16)$$

Rearranging (2.16), one can solve for the surface concentrations C_S^A and C_S^B:

$$C_S^A = \frac{\gamma_B C_{eq}^B + (\gamma_B + 1)\gamma_A C_{eq}^A}{(\gamma_B + 1)(\gamma_A + 1) - 1} \qquad (2.17)$$

$$C_S^B = \frac{(\gamma_A + 1)\gamma_B C_{eq}^B + \gamma_A C_{eq}^A}{(\gamma_B + 1)(\gamma_A + 1) - 1} \qquad (2.18)$$

Equations (2.17) and (2.18) will be analyzed (according Lasaga, 1998). If the rate of surface reaction is fast for mineral A, γ_A will become very large. In this case, the numerator in (2.17) becomes $(\gamma_B + 1)\gamma_A$, and the first term in the numerator of Equation (2.17) can be ignored. Therefore, C_S^A equals C_{eq}^A. Similarly, if the rate of surface reaction of mineral B is large, C_S^B will become C_{eq}^B. If both rates are high, $C_S^A = C_{eq}^A$ and $C_S^B = C_{eq}^B$ and we obtain:

$$R_A = R_B = J = \frac{D}{L}(C_{eq}^B - C_{eq}^A)A_d \qquad (2.19)$$

Equation (2.19) is the usual "mass-transport-controlled" model (Lasaga, 1998). In most geological situations, conditions lead to intermediate situations where both surface reaction and diffusion rates control mineral transformation kinetics.

2.5 Summary

- A critical cluster size has to be reached before a nucleus can grow spontaneously into a crystal. Also a critical supersaturation is required to start nucleation. The same requirements hold for crystal growth via 2D surface nucleation.

- Precipitation very often starts with the appearance of a metastable phase which then transforms into the most stable phase. In comparison to the stable phase, nucleation of the metastable phase is kinetically favoured by a lower Gibbs free energy of nucleation.

- The growth mechanism of a crystal depends on the degree of supersaturation. At low to moderate degrees of supersaturation, many crystalline substances grow through the incorporation of GU at kink sites along surface steps. The latter are often associated with lattice defects in the crystal.

3 Calcium Carbonate

3.1 Introduction

Calcium carbonate ($CaCO_3$), mainly under the form of the mineral calcite, is ubiquitous. Calcium carbonate can form purely inorganically or its precipitation can be biologically mediated. It is found in soils, rocks, and sediments. It also plays an important role in mineralized tissues of many organisms and is the most important biogenic component in pelagic marine sediments. Carbonate-rich sediments (>30% $CaCO_3$) form about 55% of the deposits on continental slopes and the deep sea (Schneider et al., 2000). Calcium carbonate is also one of the minerals exhibiting the highest weathering rate (Scheffer and Schachtschabel, 1992). Due to fast weathering and the buffer capacity of the carbonate system, small amounts of $CaCO_3$ can dominate the geochemical behavior of aquatic systems. The reaction of natural waters with carbonate minerals also exerts an important control on the chemistry of the atmosphere and oceans (Morse, 1990).

A variety of divalent metal ions (DMI) show an affinity for sorption and coprecipitation with $CaCO_3$. As DMI are ubiquitous as well, the amounts of DMI in $CaCO_3$ reflect the environmental conditions of formation. The DMI incorporation into marine biogenic calcite has received special interest, bacause it can help to reconstruct past environmental conditions (Boyle, 1981; Boyle, 1988; Lea and Boyle, 1989; Lea and Boyle, 1990; Lea and Spero, 1992; Lea et al., 1995; Mashiotta et al., 1997; Russel et al., 1994; Spero et al., 1997).

The $CaCO_3$ system is not only of major interest for natural systems. Calcium carbonates also play an important role in a broad range of industrial applications.

Just to mention one: $CaCO_3$ scale formation during transport of gas, oil and water can lead to significant obstruction problems and production losses. The interaction between $CaCO_3$ with toxic elements like cadmium (Cd) (e.g. van der Weijden and Comans, 1995) and radionuclides (e.g. Curti, 1997) resulting from human activities may offer new tools in pollution remediation.

Because of its importance and abundance, the $CaCO_3$ system and its interaction with DMI has been intensively investigated over the past 30 years. In recent years, due to the availability of new surface sensitive instrumental techniques like atomic force microscopy (AFM), transmission electron microscopy (TEM), scanning tunneling microscopy (STM) and low energy electron diffraction (LEED), significant progress in our understanding of $CaCO_3$-aqueous solution interactions has been achieved. The aim of this chapter is to present a general description of the $CaCO_3$ system and sorption of DMI.

3.2 Solution Equilibria

Chemical equilibria of $CaCO_3$ in aqueous solution can be described as hydrated carbon dioxide, or carbonic acid, undergoing dissociation (ionization) (Pilson, 1998),

$$CO_2(gas) \xrightleftharpoons{K_H} CO_2(aq) \tag{3.1}$$

$$CO_2(gas) + H_2O \xrightleftharpoons{K_0} H_2CO_3 \tag{3.2}$$

$$H_2CO_3 \xrightleftharpoons{K_1} HCO_3^- + H^+ \tag{3.3}$$

$$HCO_3^- \xrightleftharpoons{K_2} CO_3^- + H^+ \tag{3.4}$$
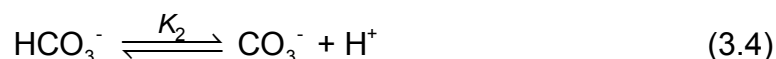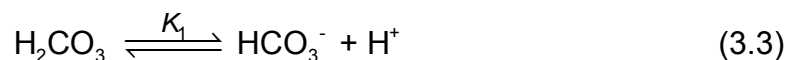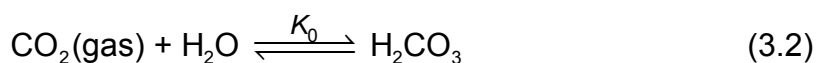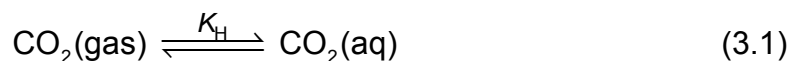
and ion pair formation and hydrolysis of the calcium ions (Sawada, 1998):

$$Ca^{2+} + HCO_3^- \xrightleftharpoons{K_{C1}} CaHCO_3^+ \tag{3.5}$$

$$Ca^{2+} + CO_3^{2-} \xrightleftharpoons{K_{C2}} CaCO_3^0 \tag{3.6}$$

$$Ca^{2+} + OH^- \xrightleftharpoons{K_{C3}} CaOH^+ \tag{3.7}$$
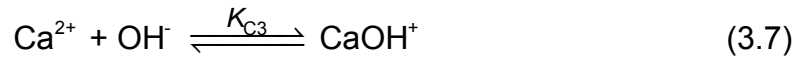
In general, the precipitation of $CaCO_3$ is written as:

$$CaCO_3 \text{ (solid)} \xrightleftharpoons{K_{CC}} Ca^{2+} + CO_3^- \tag{3.8}$$
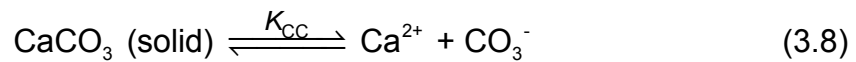
Furthermore, in aqueous systems, the dissociation of water (H_2O) has to be taken into account:

$$H_2O \xrightleftharpoons{K_W} H^+ + OH^- \tag{3.9}$$

The next section describes the different steps involved in the $CaCO_3$ equilibria in more detail. In this discussion, brackets correspond to concentrations, whereas braces indicate activities. The negative logarithm of an equilibrium constant (K) is denoted by the abbreviation pK.

Dissociation of water (Equation 3.9): As can be seen from Equation 3.9, water dissociates into hydrogen (H^+) and hydroxyl (OH^-) Ions. It should be mentioned that free H^+ ions do not exist. Hydrogen is present under the hydrated form, H_3O^+. However, for reasons of simplicity the general way to represent H_3O^+ is to write it as H^+. The pK for the dissociation reaction (Equation 3.10) at $25°C$ is 13.999 (Buttler, 1982).

$$\{H^+\} \times \{OH^-\} = K_w \{H_2O\} \tag{3.10}$$

Henry's Law (Equation 1): Carbon dioxide (CO_2) gas dissolves in water to the extent determined by its partial pressure, and the interactions of dissolved carbon dioxide (denoted by (aq)) with other solutes. The concentration of CO_2 is normally expressed by Henry's Law (Buttler, 1982):

$$[CO_2] = K_H \, pCO_2 \qquad\qquad (3.11)$$

Henry's Law constant K_H is about $10^{-1.5}$ at 25°C, when aqueous concentrations are expressed in moles per liter, and the partial pressure of CO_2 (pCO_2) in bars (Buttler, 1982).

Hydration (Equation 3.2): When CO_2 dissolves in acidified water most of the molecules remain as free, unassociated CO_2 (written as CO_2 (aq)). Some of the molecules combine with water (Equation 3.2). This reaction is slow compared to the ionization reaction. However, at equilibrium $\{H_2CO_3\}$ is only 10^{-3} as large as $\{CO_2$ (aq)$\}$, and has no special significance in the acid-base equilibria, since both CO_2 (aq) and H_2CO_3 are uncharged (Buttler, 1982). Conventionally, the CO_2 (aq) and H_2CO_3 species are treated together as if they were one substance (denoted as CO_2(aq)). For equilibrium calculations the constant K_0 (Equation 3.2) is of minor interest, as the concentration of CO_2 (aq) is directly proportional to pCO_2. It has to be noted, that in alkaline solutions the following reaction becomes significant too:

$$CO_2 \text{ (aq)} + OH^- \rightleftharpoons HCO_3^- \qquad\qquad (3.12)$$

Ionization (Equation 3.3 and 3.4): The ionization of hydrated carbon dioxide gives H^+, HCO_3^- and CO_3^{2-}. The pK value at 25°C and 1.013 bar is 6.681 for K_1 and 10.329 for K_2 (Plummer and Busenberg, 1982) for the following system:

$$\{H^+\} \{HCO_3^-\} = K_1 \{CO_2(aq)\} \{H2O\} \qquad\qquad (3.13)$$

$$\{H^+\} \{CO_3^-\} = K_2 \{HCO_3^-\} \qquad\qquad (3.14)$$

The speciation of the aqueous carbonate species as a function of pH is illustrated in Figure 3.1.
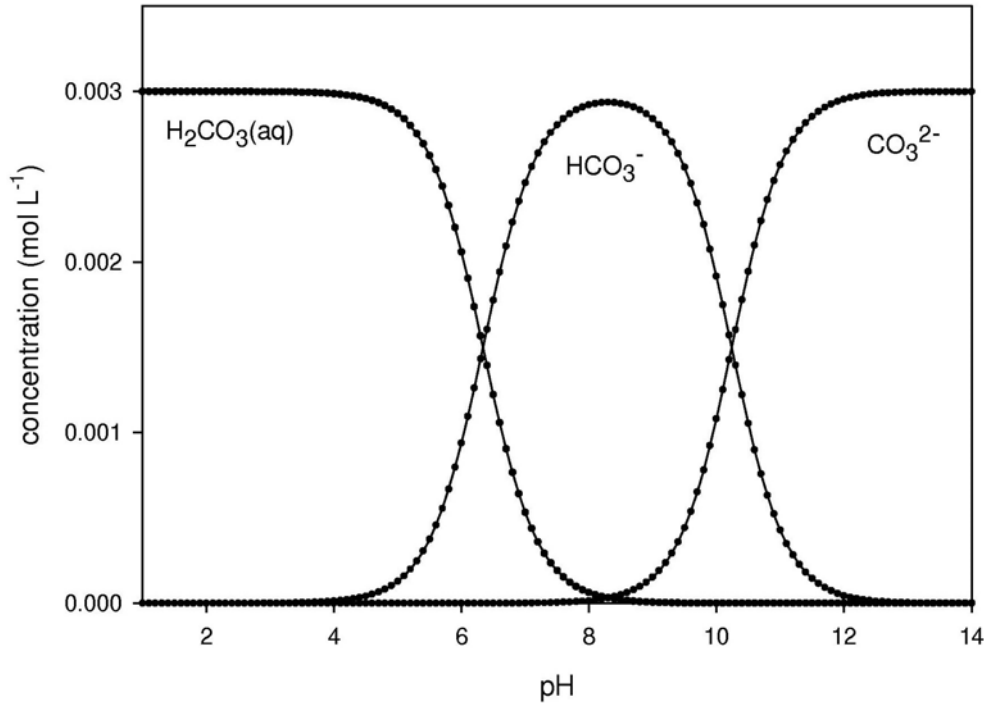
Figure 3.1: Speciation of major carbon species depending on pH (total concentration 0.003 mol L^{-1}, T = 20°C, closed system, and ionic strength I = 0).

If Ca is added to the previously described system, the following additional aqueous species will be present in the system (Equations 3.5, 3.6, and 3.7): Ca^{2+}, $CaHCO_3^+$, $CaCO_3^O$ and $CaOH^+$. The equilibrium constants (pK) are 11.434 for K_{C1}, 3.22 for K_{C2} (Plummer and Busenberg, 1982) and -12.697 for K_{C3} (NIST 46.3) for the following reactions at 25°C:

$$\{CaHCO_3^+\} = K_{C1} \{Ca^{2+}\} \{HCO_3^-\} \tag{3.15}$$

$$\{CaCO_3^0\} = K_{C2} \{Ca^{2+}\} \{CO_3^{2-}\} \tag{3.16}$$

$$\{CaOH^+\} = K_{C3} \{Ca^{2+}\} \{OH^-\} \tag{3.17}$$
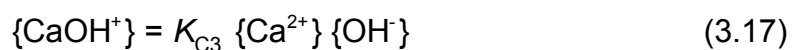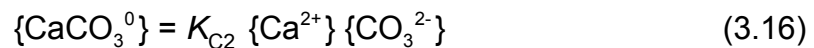
At this point no single equilibrium constant for the formation of $CaCO_3$ according to Equation 3.8 can be given. The reason is the existence of different $CaCO_3$ polymorphs as will be discussed in the next section.

3.3 The Polymorphs of CaCO₃ and their Properties

Calcium carbonate can occur in the form of three anhydrous crystalline polymorphs: vaterite, aragonite and calcite. The solubility products (K) are given in Table 3.1. Three hydrated phases of $CaCO_3$ are known to exist (Elfil and Roques, 2001). Amorphous calcium carbonate (ACC), monohydrate calcium carbonate (MCC) (mineral name monohydrocalcite) and hexahydrate calcium carbonate (HCC) (mineral name ikaite). The solubility products (K) are given in (Table 3.1).

Table 3.1: Solubility constants for the different calcium carbonate polymorphs at 25°C and in general form.

Polymorph	pK at 25°C	log K (T in K and t in °C)	Ref.
ACC	6.28	10 < t < 55°C 6.1987 + 0.00053369 t + 0.0001096 t^2	a*
HCC (Ikaite)	6.59	0 < t < 25°C 0.1598 - 2011.1 / T	b*
MCC (monohydrocalcite)	7.15	15 < t < 50°C 7.050 + 0.000159 t^2	c*
Vaterite	7.913 ± 0.020	0 < t < 90°C -172.1295 - 0.077993 T + 3074.688 / T + 71.595 log T	d*
Aragonite	8.336 ± 0.020	0 < t < 90°C -171.9773 - 0.07793 T + 2903.293 / T + 71.595 log T	d*
Calcite	8.480 ± 0.020	0 < t < 90°C -171.9065 – 0.077993 T + 2839.319 / T + 71.595 log T	d*

(a*) (Brečević and Nielsen, 1989), (b*) (Bischoff et al., 1993), c* (Kralj and Brecevic, 1995), (d*) (Plummer and Busenberg, 1982).

3.3.1 Amorphous Calcium Carbonate

Amorphous calcium carbonate (ACC) is the polymorph with the highest solubility. ACC often exhibits spherical shape with a diameter lower than 1 µm. This phase is unstable and transforms within minutes into crystalline phases: a mixture of vaterite and calcite at lower temperatures (10-30°C), and aragonite at higher temperatures (60-80°C). At intermediate temperature (40-50°C) the formation of all three phases is observed (Ogino et al., 1987). In general, ACC is an intermediate phase in $CaCO_3$ precipitation experiments conducted in the laboratory. Lately, different authors showed that ACC may play an important role in $CaCO_3$ biomineralization processes (e.g. Aizenberg et al., 1997; Beniash et al., 1997). In biological systems, ACC can serve as a precursor for other carbonate phases (like in inorganic systems), or be prevented from transformation by means of organic macromolecules that stabilize ACC.

3.3.2 Hexahydrate Calcium Carbonate

Hexahydrate calcium carbonate (HCC) ($CaCO_3 \cdot 6H_2O$) was already mentioned in 1916 to be one of several $CaCO_3$ polymorphs known from laboratory experiments (Johnston et al., 1916). The natural occurrence of HCC was first reported by Pauly (1963). The mineral was named <u>ikaite</u> after the location of its discovery; the bottom of Ika Fjord in Greenland (Pauly, 1963). Later ikaite was also found in other places. All the natural occurrences appear to be anoxic and have water temperatures of 3°C or lower. For a detailed review, the interested reader is referred to the work of Bischoff et al. (1993). Pauly (1963) suggested that the ikaite columns in the Ika Fjord form by seepage of fresh water from the bottom of the fjord. Buchardt et al. (1997) confirmed this theory by measuring the chemical composition of the seep water. They showed that seep water with high pH and rich in phosphate leeks under low-temperature conditions from underwater springs and mixes with seawater.

HCC has a monoclinic structure (space group C2/c or Cc) with Ca bound more closely to the six H_2O molecules than to the CO_3^{2-} ion, and with a density of 1.8 g cm^{-3} (Bischoff et al., 1993). Crystals prepared according to the method described by Johnston (1916) are described as well-formed prismatic crystals with average

dimensions of about 30 by 30 by 15 µm (Bischoff et al., 1993). The presence of phosphate suppresses the growth of anhydrous $CaCO_3$ crystals enabling the growth of ikaite (Dickens and Brown, 1970). Therefore, most experimental procedures for ikaite synthesis usually include the presence of a substance inhibiting the formation of anhydrated phases, e.g., magnesium cations or sodium polyphosphate (Dickens and Brown, 1970). At temperatures around 0°C ikaite is stable but at warmer temperatures decomposes rapidly to anhydrous phases (vaterite and/or calcite) and water, which causes an increase in mineral density (Mackenzie, 1923). Ikaite has been found to be relatively stable at temperatures of 25°C and pressure of around 5 MPa (Marland, 1975) (Figure 3.2). In contrast to the other $CaCO_3$ phases, the solubility of ikaite increases with increasing temperature (Figure 3.3) (Bischoff et al., 1993).
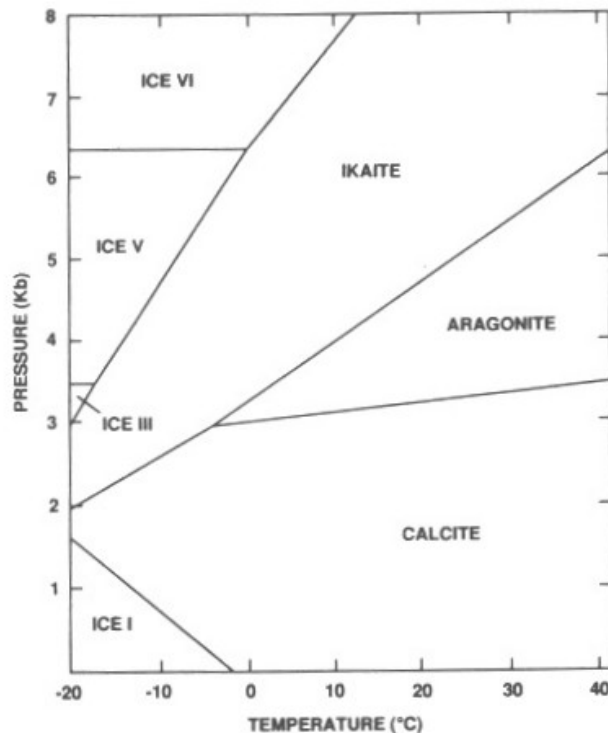
Figure 3.2: P-T phase relations in the water-saturated $CaCO_3$ system (from Bischoff et al., 1993).
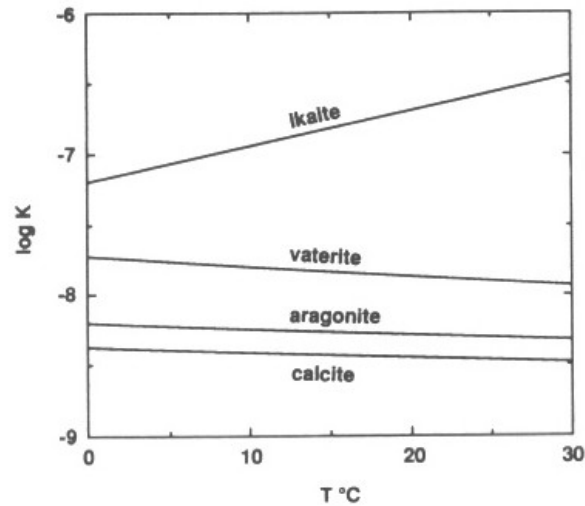
Figure 3.3: Representation of log *K* versus temperature for ikaite, vaterite. aragonite and calcite. At 0°C Ikaite is more soluble than the other phases presented. It is the only phase that shows an increase in solubility with increasing temperature (from Bischoff et al., 1993).

3.3.3 Calcium Carbonate Monohydrate

Calcium carbonate monohydrate (MCC) ($CaCO_3 \cdot H_2O$), like HCC, was first observed in laboratory experiments. MCC has been synthesized by many workers, often as a byproduct during the attempt to precipitate dolomite (for a review, see Taylor, 1975). MCC in the natural environment has been first reported in 1959 (Fleischer, 1969), who found that calcareous encrustations in Lake Issyk-Kul, Kirkistan, consisted entirely of MCC. The mineral name for this phase is monohydrocalcite because of its calcite composition with one molecule of water (Ref. in Fleischer, 1969). Monohydrocalcite was also found in speleothems in a small cave in the Fraenkische Schweiz, Germany (Fischbeck and Müller, 1971), and as component of otoliths of the tiger shark (*Calcocerdo cuvier*) (Carlström, 1963). In Taylor (1975) reported the occurrence of monohydrocalcite in two small lakes in the south-east of South Australia (Taylor, 1975).

Calcium carbonate monohydrate crystals are mostly of spherical shape with a diameter close to 100 µm. The crystal system of MCC is hexagonal (trigonal) (crystal class 32). The density reported for MCC is 2.38 g cm^{-3}.

3.3.4 Vaterite

Vaterite is the most soluble of the three anhydrous calcium carbonate ($CaCO_3$) polymorphs, vaterite, aragonite and calcite. According to Friedman and Schulz (1995), Linck (1903) named the mineral after the discoverer, H. Vater, although this statement could not be verified in the cited reference. The name goes indeed back to H. Vater, but Meigen may have been the first one to use the name vaterite in 1911 for "*Vater's third modification of calcium carbonate*" (Gibson et al., 1925), a $CaCO_3$ of spherical morphology Vater (1897) described in his work. In the latter work, Vater also described lens-shaped aggregates and hexagonal plates among some of his precipitates. These aggregates have been recognized later as a separate form by Johnston et al. (1916) and named μ-calcium carbonate. Wolf et al. (2000) reported that Vater also used the term μ-$CaCO_3$ but this contention could not be confirmed by the cited literature (Vater, 1897; Vater, 1899). A confusing and incoherent use of references on the history of the name vaterite and μ-$CaCO_3$ is pervasive throughout the literature.

Heide (1924) concluded that vaterite is a modification of $CaCO_3$ distinct from aragonite and calcite and less stable than both. He showed that the Debye-Scherrer diagram (X-ray diffraction pattern) of vaterite is different from those of calcite and aragonite, and therewith proved the existence of a third crystalline modification of $CaCO_3$. Gibson et al. (1925) pointed out that the modification Vater described as the "third modification of calcium carbonate" showed the same X-ray diffraction pattern as calcite, whereas $CaCO_3$ crystals of spherical shape prepared after a method described by Heide (1924) showed the same X-ray pattern as the μ-$CaCO_3$ described by Johnston et al. (1916). However, the name vaterite persisted in the literature.

Vaterite is not stable in aqueous solutions under Earth surface conditions, and transforms within a short period of time into calcite or aragonite (depending on temperature) (Ogino et al., 1987). This is one reason why vaterite is rare in the natural environment. Chapter 4 and 5 describe the formation and transformation of vaterite in detail.

Vaterite belongs to the hexagonal crystal system (crystal class 6/m 2/m 2/m) (Kamhi, 1963) and has a density of 2.54 g cm^{-3}.

3.3.5 Aragonite and Calcite

Compared to the other $CaCO_3$ polymorphs the literature available on aragonite and calcite is humongous. Therefore, I forgo a detailed description of these polymorphs, since the interested reader can easily find the appropriate information elsewhere. The basic mineralogical data for aragonite and calcite are given below.

Aragonite is named after the locality "Molina de Aragón" (Guadalajara, Spain), 25 km outside Aragon. Aragonite belongs to the orthorhombic crystal system (crystal class 2/m2/m2/m) and has a density of 2.94 g cm^{-3}. A notable property of aragonite is that its stability decreases with increasing temperature (at 400°C aragonite spontaneously transforms into calcite), but not with increasing pressure. The name Calcite name comes from the Latin word calx (lime). It has a density of 2.71 g cm^{-3} and belongs to the trigonal symmetry system (crystal class-3 2/m).

3.4 Incorporation of Divalent Metal Ions into Calcium Carbonate

During precipitation of a crystal a three-dimensional periodic structure is built and foreign ions can be incorporated in replacement of the major ions of the solid (e.g. Sr^{2+} replacing Ca^{2+} in $CaCO_3$). Two distinct solid solution characteristics can be distinguished with regard to the pure phases of the elements of interest. For some minerals a perfect miscibility between the end-member phases exists. A good example is the perfect miscibility of the two end member phases forsterite ($Mg_2Si_2O_4$) and fayalite ($Fe_2Si_2O_4$) in the mineral olivine ($[Mg, Fe]_2Si_2O_4$). In contrast, otavite ($CdCO_3$) and $CaCO_3$ show a distinct miscibility gap over a wide range of Cd^{2+} / Ca^{2+} ratios, leading to sector zoning (Fernandez-Gonzalez and Prieto, 1999; Prieto et al., 1997).

It is not possible to predict the miscibility of two phases based on theoretical considerations. For example, the similar ionic radii of Cd and Ca (1 and 0.95 Å) could lead to the expectation that both ions are easily exchangeable, allowing for miscibility between calcite and otavite. However, this is not observed. Therefore, it could be that the miscibility gap is caused by the difference in the solubility products of calcite and otavite (log K = 8.36 and 12). If the solution is supersaturated with respect to both

phases (e.g. $CdCO_3$ and $CaCO_3$), there is no guarantee that a homogeneous mixed solid precipitates from solution. This is important to keep in mind when interpreting bulk partition coefficients and distribution constants.

3.4.1 Partition Coefficient and Distribution Constant

The distribution of a trace element (Tr) between two phases is described by the partition coefficient. In aqueous systems these two phases are normally the aqueous solution and a mineral. Typically the partition coefficient is normalized to the value of the partition coefficient for another element. This is normally the main cation (M) of the mineral (Ca for $CaCO_3$). The terminology in this field is far from consistent (Beattie et al., 1993). The terms "partition coefficient", "distribution coefficient", and "exchange coefficient", and the corresponding symbols D, K_d, and K_D, are often interchanged. The definition of the partition coefficient D_{Tr} given by Morse and Bender (1990) will be used here:

$$D_{Tr} = \frac{[Tr]_s / [Tr]_l}{[M]_s / [M]_l}$$ (3.18)

where [Tr] and [M] are the molar concentrations of the trace and major element in the solid (s) and liquid (l) phases.

The partition coefficient represents a phenomenological description of the incorporation of a trace element, and is distinct from the thermodynamic distribution constant $K_{D_{Tr}}$, which describes the distribution of the trace element at equilibrium. At thermodynamic equilibrium the distribution of trace elements is related to the solubility products of the mineral end-member phases. The solubility products of MCO_3 and $TrCO_3$ are related to the distribution constant as follows (McIntire, 1963):

$$K_{D_{Tr}} = \left(\frac{K_{MCO_3}}{K_{TrCO_3}} \right)^{\frac{1}{v_c}} \left(\frac{\gamma_{Tr}}{\gamma_M} \right) \left(\exp \left(\frac{-\Delta\mu}{v_a RT} \right) \right)$$ (3.19)

where K_{MCO_3} and K_{TrCO_3} denote the solubility product of the major element and trace element end-member carbonate mineral, γ_{Tr} and γ_M are the activity coefficient of the major and trace element in aqueous solution, ν_c is the ratio of the number of cations in Tr_nCO_3 to the number of cation in M_mCO_3 so that ν_c is n/m and ν_a the anion ratio. R is the gas constant (8.314 J / mol K) and T the temperature (in K) and $\Delta\mu$ the difference between the chemical potential of $TrCO_3$ in a pure crystal of $TrCO_3$ and its chemical potential as a solid component in MCO_3.

It is difficult to measure or calculate the values for all parameters within this Equation 3.19. Especially the difference in chemical potential $\Delta\mu$ is not known. Rimstidt et al. (1998) tried to estimate the values of $K_{D_{Tr}}$ for many elements by fitting a large dataset collected throughout the literature. Their work, and many other experimental investigations (Kitano and Oomori, 1971; Kitano et al., 1971; Lorens, 1981; Mucci, 1986; Mucci and Morse, 1983; Pingitore and Eastman, 1984; Temmam et al., 2000; Tesoriero and Pankow, 1996), showed that the partition coefficient is influenced by kinetics. Quite a number of experiments have shown that three different exchange behaviors of trace elements can be distinguished (Rimstidt et al., 1998; Tesoriero and Pankow, 1996): (1) the trace element concentration is enriched within the crystal compared to its concentration in solution, i.e., $K_{D_{Tr}} > 1$, (2) the trace element concentration is depleted within the crystal, i.e., $K_{D_{Tr}} < 1$, and (3) no fractionation occurs, i.e., $K_{D_{Tr}} = 1$.

Depending on the distribution behavior of the trace element between solution and crystal, the measured value for the partition coefficient differs from the equilibrium value in the following way. For elements with a $K_{D_{Tr}} > 1$, measured D_{Tr} values will be lower than. For $K_{D_{Tr}} < 1$, the opposite behavior should be observed. In both cases D_{Tr} approaches the equilibrium values with decreasing growth rate. This behavior is illustrated in Figure 3.3. Note that the term "growth at equilibrium" is widely used in the literature to describe a behavior not influenced by kinetics.
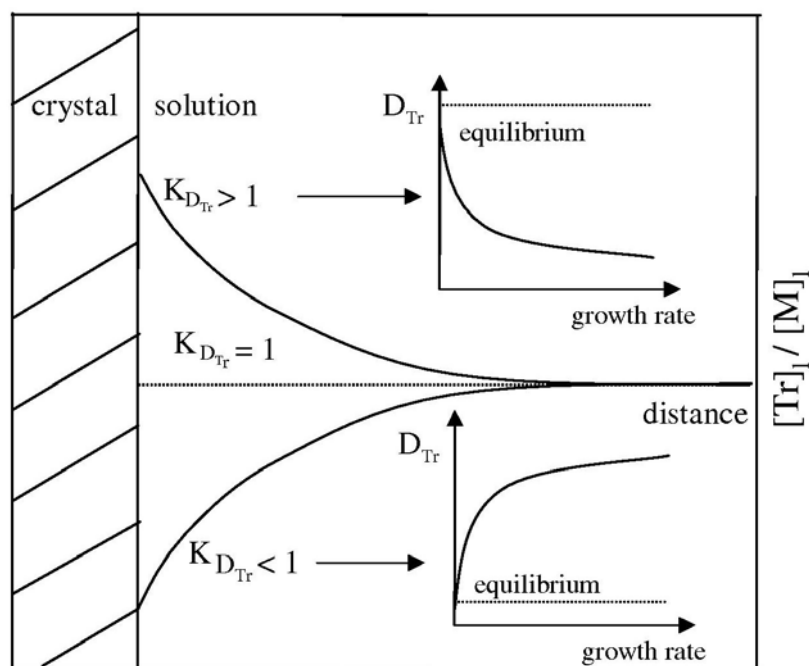
Figure 3.3: Different exchange behaviors of trace elements. For $K_{D_{Tr}} > 1$, the value [Tr] / [M] is higher in the crystal than in the bulk solution. A $K_{D_{Tr}}$ value < 1 shows the opposite exchange behavior. If the incorporation into the crystal shows the same ratio as the bulk medium, $K_{D_{Tr}} = 1$. For $K_{D_{Tr}}$ values > 1, experimentally determined D_{Tr} are in general lower than the predicted equilibrium value, while the opposite holds for experimental values in the case of $K_{D_{Tr}} < 1$ (Modified after Rimstidt et al. 1998).

Paquette and Reeder (1995) and Reeder (1996) showed that at a microscopic scale the incorporation of foreign ions into calcite is controlled by the surface structure. They measured heterogeneous trace element distributions on growth hillocks exhibiting nonequivalent vicinal faces (polygonized growth hillocks result from spiral growth). Most trace elements show a strong preferential incorporation when comparing nonequivalent vicinal faces.

In general, the concentration of a trace element measured within a crystal can be influenced by the composition of the solution from which the crystal is precipitated, as well as the growth rate and surface structure of the crystal. Furthermore, partition coefficients determined for marine biogenic calcite, are <u>not</u> determined with respect to the solution the crystal has precipitated from. The composition of the solution at the site of precipitation, located somewhere within the organism, is seldom known. For that reason distribution coefficients are calculated relative to seawater composition. This has to be taken into account if partition coefficients of biogenic carbonates are interpreted based on data from inorganic precipitation experiments.

4 Vaterite and its Morphology

4.1 Introduction

The existence of the $CaCO_3$ polymorph vaterite (see 3.3.4) was first observed in laboratory precipitation experiments conducted at high degrees of supersaturation, under which conditions it spontaneously precipitates. Vaterite is not stable in aqueous solution under Earth surface conditions, and transforms within a short period of time into calcite or aragonite (depending on temperature) (Ogino et al., 1987). This is one reason why vaterite is rare in the natural environment. Vaterite is reported to be present in some biological systems, for example, in the static body of mysid shrimp (Wittmann and Ariani, 1996), gallstones (Sutor and Wooley, 1968), fresh water pearls (Ma and Lee, 2006), otoliths of some fish (Gauldie, 1996; Lenaz and Miletic, 2000), and egg shells (Tullett et al., 1976). Furthermore, vaterite has been reported to form naturally in some sediments, and during oilfield drilling (Friedman and Schultz, 1995; Giralt et al., 2001; Lenaz and Miletic, 2000).

The fact that vaterite forms and persists in a number of natural systems seems to contradict its thermodynamic instability. Therefore, some mechanism must prevent vaterite from transforming. The observation that vaterite forms naturally raises the question whether vaterite can serve as a precursor phase of aragonite and calcite in natural systems, as observed in laboratory experiments. Many experiments have been conducted on the precipitation of vaterite (Dickinson et al., 2002; Euvrard et al., 2000; Kralj et al., 1990; Kralj et al., 1994), its transformation (Baitalow et al., 1998; Bischoff, 1968; Kralj et al., 1997; Ogino et al., 1987; Rock and Gordon, 1976; Spanos and Koutsoukos, 1998; Wolf et al., 2000), and the effects of inorganic solutes

(Baitalow et al., 1998; Brečević et al., 1996; Katsifaras and Spanos, 1999; Noethig-Laslo and Brecevic, 1998; Noethig-Laslo and Brecevic, 2000; Tsuno et al., 2001; Tsuno et al., 2002; Wada et al., 1995), amino acids (Manoli et al., 2002), and inorganic or organic substrates (Kanakis and Dala, 2000; Manoli et al., 1997).

Even though numerous experiments have been conducted on vaterite, few have focused on the characteristics of the solid itself. A review of the literature on vaterite and its transformation reveals that detailed descriptions of the morphology of vaterite are rare. Table 4.1 presents a compilation of experimental studies in which vaterite was synthesized and described. Even though the publications in this compilation are from the time vaterite was unambiguously identified (1925) until recent (2001), descriptions of the solid remain quite vague. Frequently, descriptions like "*particles of some spherical shape*, *with an average diameter of 10–40 µm*" are the only information given. In a few cases additional detail is given. Kralj et al. (1994) described the surface as "irregular and rough", while Vecht and Irelend (2000) and Euvrard et al. (2000) mention that the spheres are possibly built up of smaller spheres. This information is in so far of interest that an estimation of the surface area would depend on a good knowledge of the surface morphology and the size of the elementary particles. Plummer and Busenberg (1982), for example, gives a surface area of 7.2 $m^2 g^{-1}$ for crystals having diameters in the range 4–6 µm. As shown later these values are not internally consistent. In many of the published experiments, the amount of material produced is too small to allow direct measurements of the specific surface area, for instance, using the BET adsorption method. The only possible way to an assessment of the specific surface are depends strongly on whether or not the spherical vaterite particles consist of smaller crystals.

Table 4.1: Information about vaterite crystals in selected publications, published from 1925 until 2001.

Ref. (Year)	Preparation method	XRD	size (µm)	Remarks
a (1925)	method of Heide (1924) (not exactly described)	yes	10–15	first comparison with µ-$CaCO_3$
b (1957)	20 ml 1 M $Ca(NO_3)_2$ + 0.1 M Na_2CO_3 and 1 M Na_2CO_3 + 0.1 $Ca(NO_3)_2$	yes	5–20	relation observed between crystal size and ion concentration in stock solution
c (1968)	50 ml NH_4OH + 1 l $CaCl_2$ solution through which CO_2 gas is bubbled	no	?	identified by optical microscopy (spherulites)
d (1971)	no information	no	?	vaterite mentioned but no further information given
e (1982)	1 M $CaCl_2$ + 2 M NH_3 CO_2 bubbling	no	4–6	surface area of 7.2 m^2/g (method not mentioned)
f (1990)	no information	yes	3.2–<5	no information
g (1994)	5 mM $CaCl_2$ + 5 mM Na_2CO_3 sample dried at 105°C	yes	2.7–4.6	sonifier with microtip used during precipitation; surface described as "irregular" and rough; size of spheroids on the photograph shown seem to be 6 µm, dried at 105°C
h (1999)	No information	yes	(≈5)	size taken from picture, not mentioned in text
I (2000)	CO_2 bubbled through 0.11 M $CaCl_2$, when saturated (pH ≈ 2.5) ammonia added	yes	2 - 5	spheroidal aggregates composed of small 50 nm to 100 nm particles
j (2000)	Electro-crystallization	yes	> 1–14	poorly described but photograph indicates spherical aggregates
k (2001)	natural vaterite	yes	125–250	microbial biscuits containing vaterite fibers
l (2001)	5 mM $CaCl_2$ (pH 10, (NaOH) + 5 mM Na_2CO_3 (pH 10, HCl)	yes	?	washed with water, then dried at 100°C (1 h)

a) (Gibson et al., 1925), b) (Wray and Daniels, 1957), c) (Bischoff, 1968), d) (Albright, 1971), e) (Plummer and Busenberg, 1982), f) (Kralj et al., 1990), g) (Kralj et al., 1994), h) (Hobbs and Reardon, 1999), i) (Vecht and Ireland, 2000), j) (Euvrard et al., 2000), k) (Giralt et al., 2001), l) (Dickinson and Mcgrath, 2001)

Given the possible importance of vaterite as a precursor phase in the formation of calcite, this chapter focuses in detail on the morphology of vaterite crystals obtained with different precipitation procedures. Due to its much higher resolution than a conventional $\underline{S}$canning $\underline{E}$lectron $\underline{M}$icroscope (SEM), a $\underline{F}$ield $\underline{E}$mission-$\underline{G}$un $\underline{S}$canning $\underline{E}$lectron $\underline{M}$icroscope (FEG-SEM) was used.

4.2 Materials and Methods

4.2.1 Vaterite Preparation

The literature describes a variety of techniques to prepare vaterite (Hobbs and Reardon, 1999). A method producing relatively large quantities of solid (up to 60 g) is described by Turnbull (1997). Following this procedure (modified by Hobbs and Reardon, 1999), 500 ml of a solution of 1 M $CaCl_2 \cdot H_2O$ and 2 M NH_3 was placed in a wide-mouthed glass Erlenmeyer flask. Pure CO_2 was bubbled slowly through the solution using a fritted glass bubbler. (Note: high bubbling rates produce up to 10 % calcite in the final precipitate, Hobbs and Reardon, 1999.) After approximately 15 minutes, the solution became cloudy. After an additional 15 minutes, the suspension was filtrated through a no. 42 Whatman$^{®}$ filter paper using a Buchner funnel. The filtrate was washed with ethanol and dried for 20 minutes under vacuum, before being placed in a desiccator containing silica gel. The disadvantage of the original precipitation method of Turnbull (1997) is the high chloride concentration of the solid (approximately 24 g/kg). Hobbs and Reardon (1999) therefore proposed an additional cleaning step, which reduced the chloride concentration of the solid by about 84%: the solid was washed with a 0.021 M $Ca(OH)_2$ solution, centrifuged several times, and then dried as described before. The detailed procedure is described elsewhere (Hobbs and Reardon; 1999). This method, including the additional cleaning step, is referred to as **m1**.

A slightly modified method, referred to as **m2**, was applied to investigate the role of CO_2 bubbling. The solution composition was identical to that in **m1**. The solution, however, was placed in a test tube instead of a wide-mouthed glass Erlenmeyer

flask. CO_2 was slowly bubbled into the solution via a glass tube, producing much bigger bubbles than the fritted glass bubbler. The solid was dried and stored as described in **m1**, but without applying the washing procedure. The amount of solid produced with **m2** was about 1 g. A third method, referred to as **m3**, was used based on an experimental procedure described by Wray and Daniels (1957). A 1 M $CaCl_2$ solution was added to a 0.1 M Na_2CO_3 solution (proportion 50 : 50). The precipitate was dried and stored as described for **m1**. All chemicals were of pro analysis quality (Merck[®]), and double distilled water was used for the preparation of all solutions.

In this study fourteen different solids (S1–S14) were produced (Table 4.2), according to methods **m1**, **m2** and **m3**. Two drying methods where used: either the freshly precipitated vaterite was dried in an oven (between 60°C and 105°C), or it was washed witheethanol and dried under vacuum. The drying methods for the different solid are listed in Table 4.2.

Table 4.2: Experimental solids. The last column indicates the modifications from the methods **m1** to **m3** described in the text.

sample	preparation method	modifications
S1	**m1**	$CaCl_2$ instead of $CaCl_2 \cdot H_2O$; solid dried in oven at 60°C after filtration
S2	**m1**	none
S3	**m1**	$CaCl_2$ instead of $CaCl_2 \cdot H_2O$
S4	**m1**	none
S5	**m1**	none
S6	**m1**	bubbling with CO_2 was stopped directly after the solution became visibly cloudy
S7	**m2**	solid dried in oven at 60°C after filtration
S8	**m1**	solid dried in oven at 60°C after filtration
S9	**m1**	solid dried in oven at 60°C after filtration
S10	**m1**	none
S11	**m1**	none
S12	**m1**	none
S13	**m3**	none
S14	**m1**	sonified with micro tip

4.2.2 Characterization of Solids

The solids were characterized by means of powder X-ray diffractometry (XRD), on a Philips PW 1700. The samples were measured at 40 kV and 30 mA using Cu-Kα radiation at a scanning speed of 0.02° 2θ s^{-1} and a time constant of 1 s. The abundance of the two polymorphs vaterite and calcite was calculated from the areas of the main diffraction peaks (Figure 4.1) of vaterite (at 27.0° 2θ) and calcite (at 29.4° 2θ), using the computer program Xfit (Cheary and Coelho, 1996).

The calibration was performed by means of five standards (pure vaterite, pure calcite, and mixtures of vaterite and calcite in 2:3, 1:1 and 3:2 mass ratios). The pure vaterite sample was prepared as described in section 4.2.1. Pure calcite was prepared by adding vaterite to a solution of bi-distilled water. XRD confirmed that after > 24 hours all vaterite was transformed into calcite.
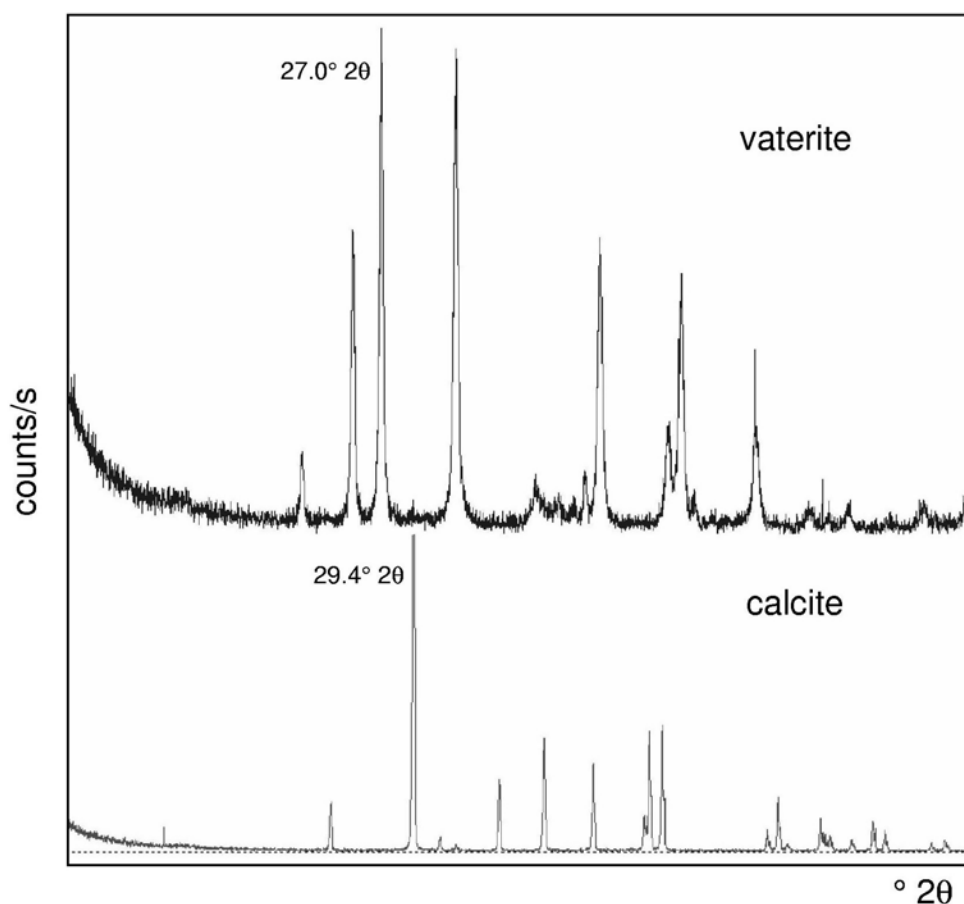
Figure 4.1: XRD patterns of pure vaterite, with a peak at 27.0° 2θ, and pure calcite obtained after complete transformation of vaterite. (The number of total counts for the diffractograms differs as can be seen from the higher background of the vaterite-scan.)

The morphology of the solids was characterized by means of a High Resolution Scanning Electron Microscope equipped with a Field Emission Gun filament (SFEG-SEM, XL30 Philips/FEI®). Samples were fixed with double sided carbon tape on aluminum stubs and coated with 6 nm Platinum/Palladium using a Cressington® 208HR sputter coater combined with a Cressinton® mtm20 thickness controller. The "through the lens detector" (TLD) was used when operating in high–resolution mode.

The particle sizes of the different solids were determined by means of the image analysis computer program analySIS® (Soft Imaging Systems). Since the same software was used to record the picture, the instrument settings of the SEM apparatus were stored within the picture and used for size calibration. Therewith it was possible to define a line across the selected sphere and to measure its exact size. The pictures used for this work were all taken at the same magnification, to ensure comparable results. A rectangle of 10 by 10 particles was defined on the SEM picture of the appropriate solid. Afterwards all 100 particles within this area where measured. The choice of the exact position of the measuring line drawn on the particles is up to the operator performing this task. However, a test wherein six different people analyzed the same picture showed that the results differed by less than 5%.

4.3 Results and Discussion

Fourteen solids (S1–S14) were individually prepared (see Table 4.2) over a time span of two years. Samples of the freshly prepared solids were characterized directly after drying by means of XRD and SFEG-SEM. After two years, all solids were reexamined by XRD and SFEG-SEM.

### 4.3.1 XRD Characterization

As described in Section 4.2.2, a set of standards was prepared for calibration of the XRD measurements. The calibration curve is presented in Figure 4.2. The

calibration showed that the peak intensity for vaterite (at 27.0° 2θ) is 4.2 ± 0.2 times stronger than for calcite (at 29.4° 2θ).
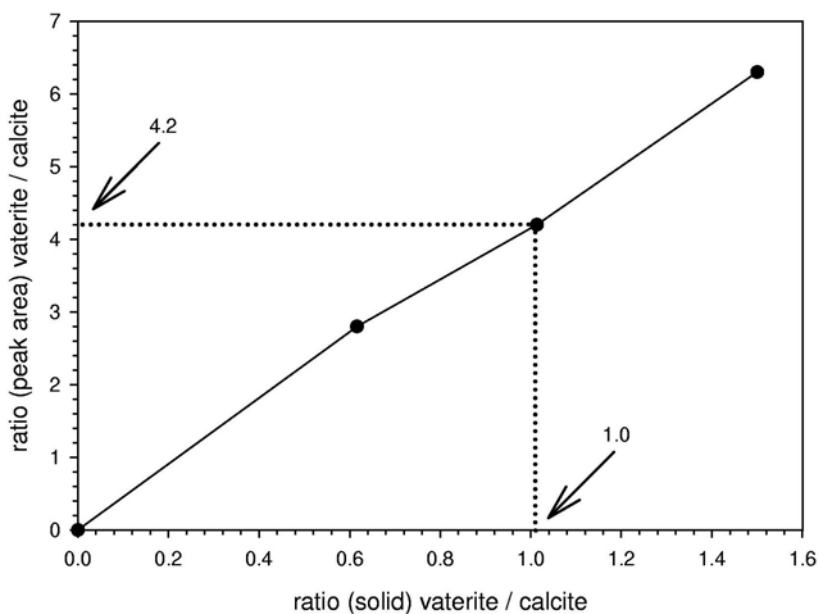
Figure 4.2: Calibration curve for a set of standards containing calcite and vaterite in different mass ratios (error within the symbol size).

The X-ray diffractogram of a standard containing 50% calcite and 50% vaterite is shown in Figure 4.3. The measurement of duplicates indicated an error of 5% when calculating vaterite / calcite concentration ratios in this type of samples. It is important to notice that the dominance of the vaterite peak makes it difficult to detect small (< 5%) concentrations of calcite present in the sample.
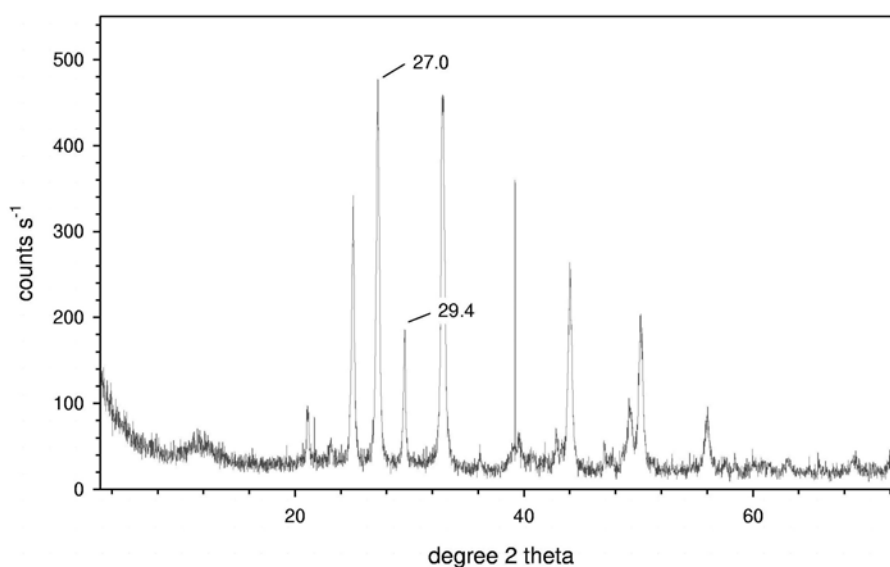
Figure 4.3: Standard containing 50% calcite and 50% vaterite. The signal of the vaterite peak (at 27.0° 2θ) is about four times bigger than that of the calcite peak (at 29.4° 2θ).

The percentages calcite in the 14 solids (S1–S14) are presented in Table 4.3. As already mentioned, all samples were analyzed directly after precipitation and at the end of the two year experimental period. A lowercase e is added to the sample label to identify the 2–year old samples. In all samples the non–calcite phase was vaterite. No other phases were detected by means of XRD. The XRD pattern of sample S7 (Figure 4.4) deviated from the other diffractograms. This sample still contained a significant amount of water, as seen from the broad band around $2\theta=30°$. This band, with a second band of less intensity towards 50°, is typical for the presence of water (van der Gaans, 2003). This was not observed in any of the other samples. Therefore it can be assumed that the other samples were properly dried before storage.

Table 4.3: Amount of calcite (measured by means of XRD) in the solids directly upon precipitation after being dried (SX) and after storage in a desiccator for two years (SXe).

sample	% calcite	sample	% calcite
S1		S1e	84.63
S2	5.56	S2e	---*
S3	4.01	S3e	40.64
S4	10.88	S4e	98.47
S5	24.43	S5e	27.21
S6	37.16	S6e	49.69
S7	unusable XRD-pattern**	S7e	99.92
S8	11.31	S8e	7.77
S9	5	S9e	6.99
S10	36.34	S10e	99.96
S11	31.65	S11e	99.99
S12	1.16	S12e	10.92
S13	99.7	S13e	99.46
S14	1.1	S14e	1.21

* solid used up before the end of the two year period
** probably contained too much water when measured (Figure 4.4)
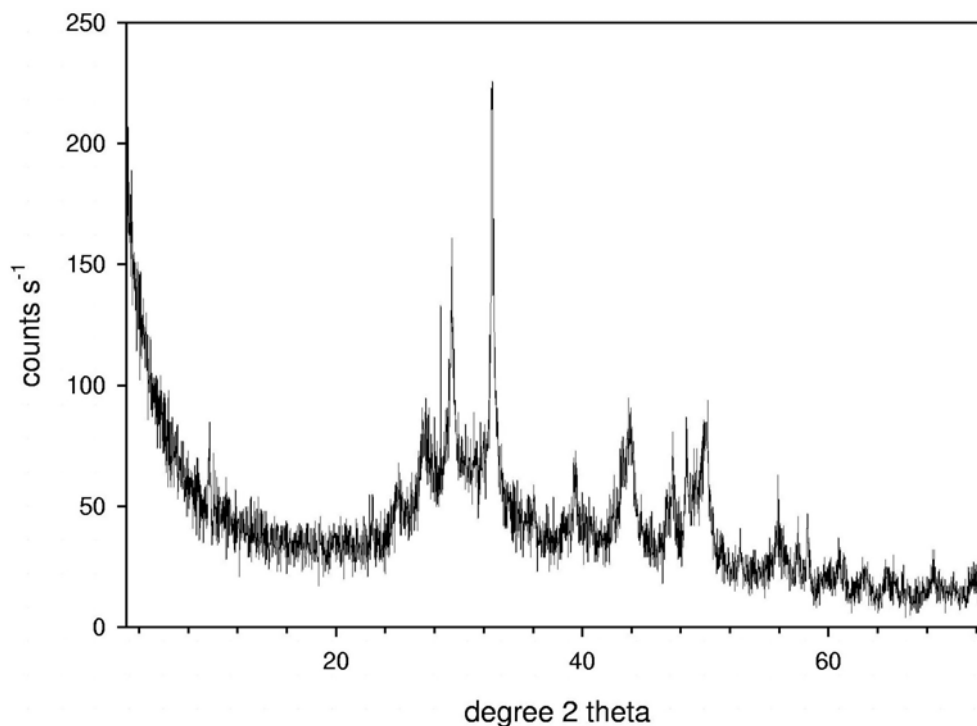
Figure 4.4: XRD pattern of solid S7, showing a broad band at 30° 2θ, followed by a second band of less intensity around 50°.

4.3.2 Vaterite Morphology

Freshly prepared solids (S1–S14) were investigated by means of SFEG-SEM. This investigation revealed a variety of different structures, which are described in detail below. Vaterite is often described as spherical in the literature. An example of this appearance is shown in Figure 4.5. A detailed examination using the high resolution mode of the SFEG-SEM (through the lens mode) showed that these spheroids are composed of smaller, spherical, particles (Figure 4.6). Therefore in this work the term framboid is used to describe spherical vaterite clusters and the term sphere (spheroid) is applied to the smaller particles that constitute the framboids.
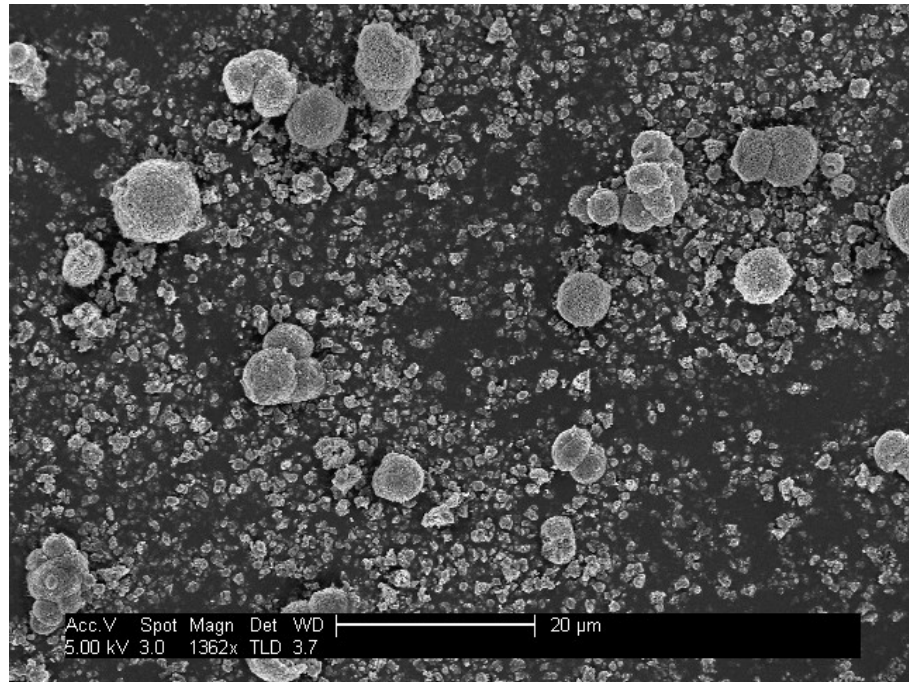
Figure 4.5: SEM picture of solid S9 with typical vaterite aggregates (framboids).
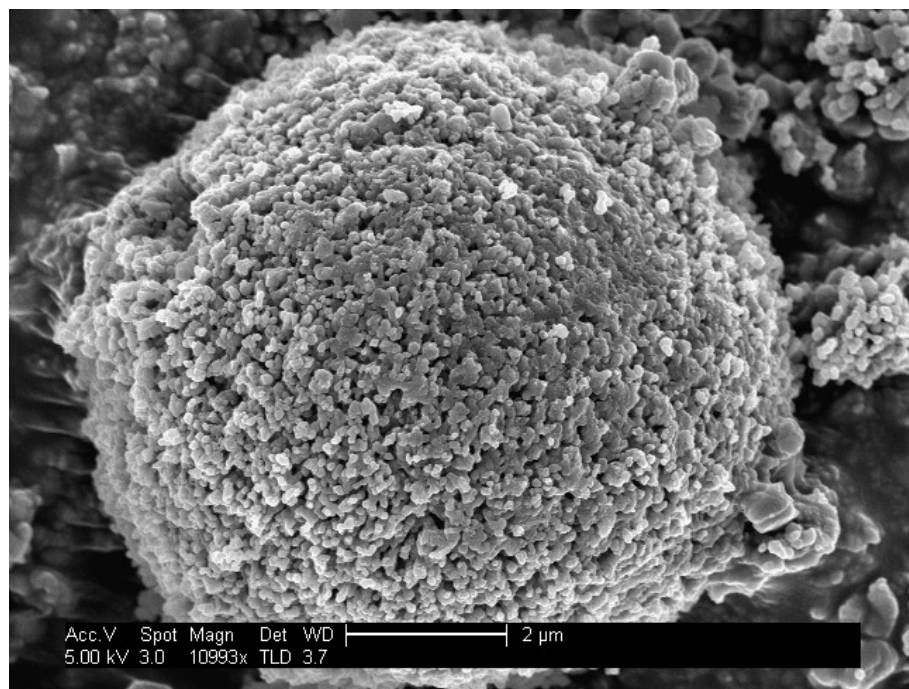
Figure 4.6: Magnification of a particle seen in Figure 4.5 (largest particle in the upper left corner) showing that the framboid is built up by smaller particles (spheres).

The vaterite morphology of the different solids varies significantly. Figure 4.7 and Figure 4.8 show examples of two other possible vaterite aggregate morphologies. In both samples vaterite spheres build bigger clusters of more

irregular, sponge like shapes. The term "irregular aggregate" will be used to distinguish the irregular shaped morphologies from the previously described spherical ones, named framboids.
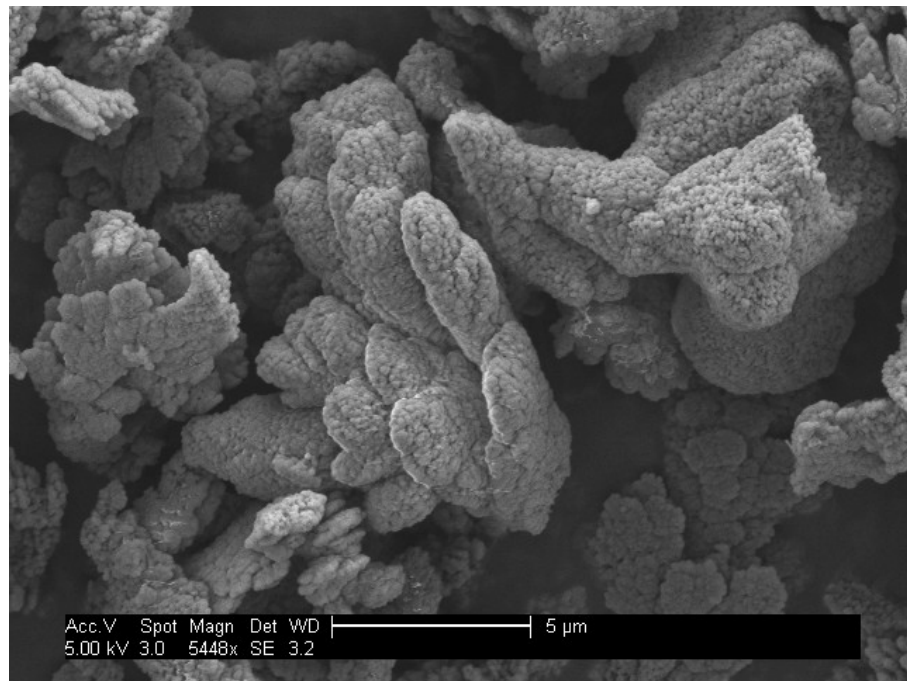
Figure 4.7: Irregular aggregates of vaterite in sample S5.
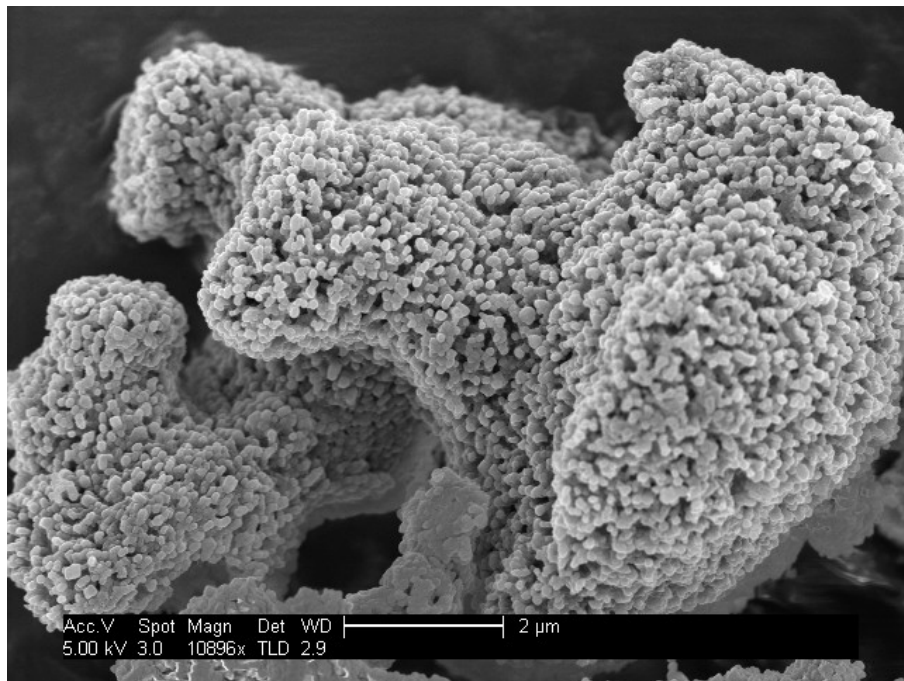
Figure 4.8: Irregular aggregates vaterite in sample S12.

Two types of how the particles are packed can be distinguished on framboidal structures. The first type is characterized by very densely packed spherical particles, resulting in little pore space and a smooth surface of the framboid. An aggregation of this type is shown in Figure 4.9. A second type is characterized by a more open structure with larger pore spaces between the spheres (Figure 4.10).
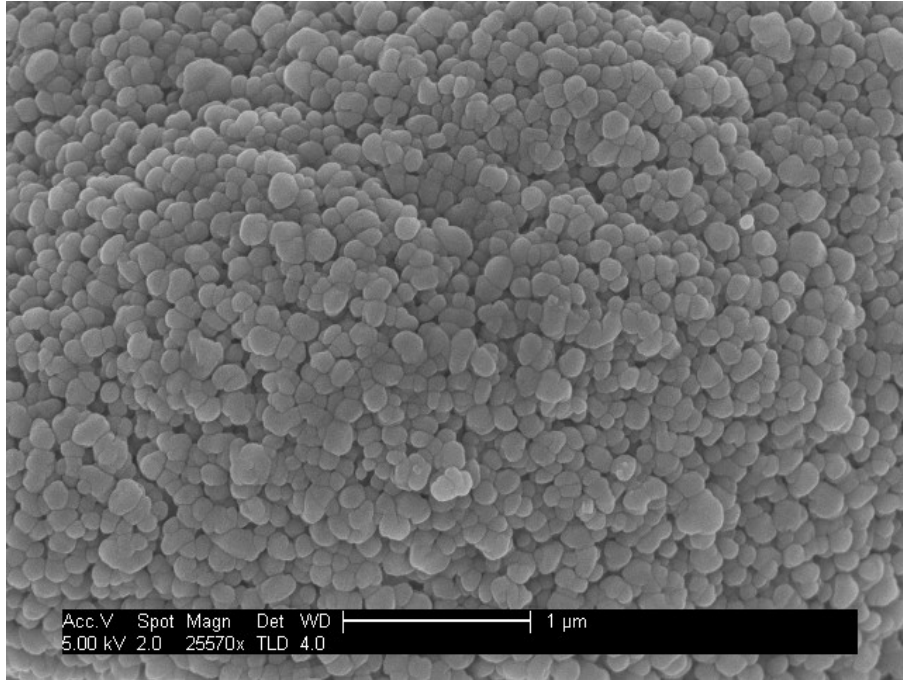
Figure 4.9: Surface of a densely packed framboid in sample S3.
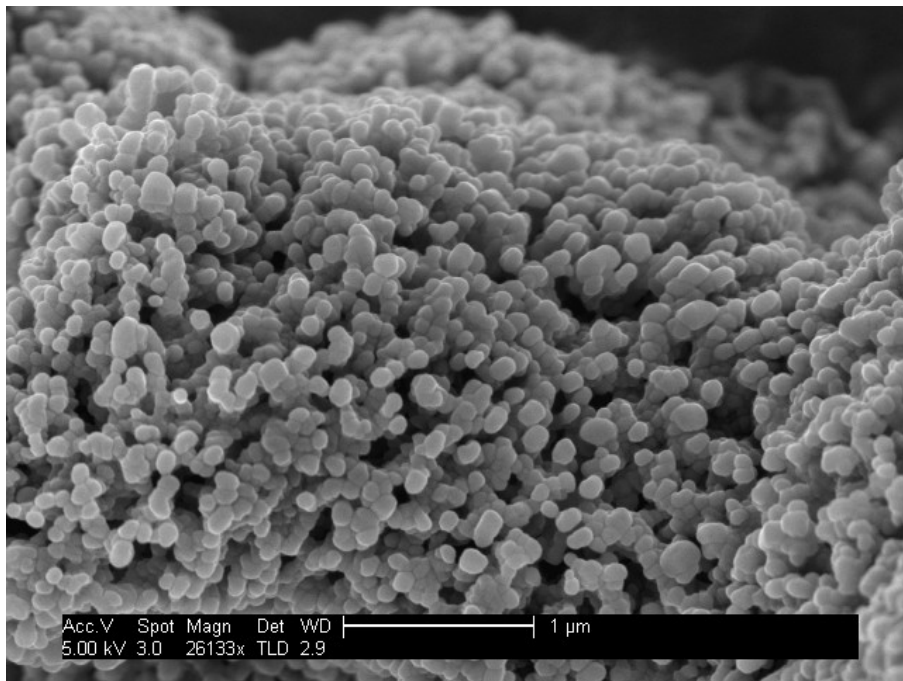
Figure 4.10: Surface of a more loosely-packed vaterite framboid in sample S12.

53

In addition, precipitates such as solid S6showed no aggregation (Figure 4.11).
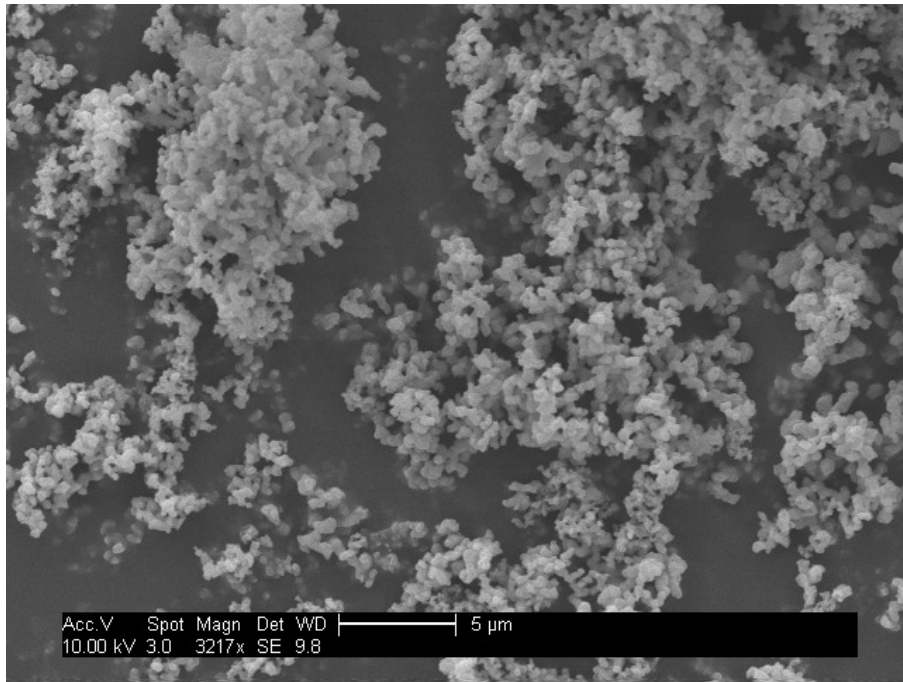
Figure 4.11: Particle in sample S6, showing no aggregation.

Table 4.4 summarizes the results of the SFEG-SEM analysis just after preparation and after the two-year experimental period. Size determinations were done as described in section 4.2.2 by means of the computer program analySIS$^{®}$ (Soft Imaging Systems). Standard deviations ($\bar{X}$) in Table 4.4 were calculated from 100 measurements per sample. Each row contains the data for the freshly prepared (SX) and aged sample (SXe).

Table 4.4: Morphology and size of the precipitated solids (investigated by means on SFEG-SEM) upon precipitation (SX) and after storage in a desiccator for two years (SXe). Abbreviation n.d. denotes "not determined" and n.p. "not present" in the sample.

| solid	spheres	framboids	cubes	size distribution spheres (nm)	size average ($\bar{X}$) spheres (nm)	size distribution framboids (cubes) (µm)	size average ($\bar{X}$) framboids (cubes) (µm)
S1	yes	yes	no	n.d.	---	n.d.	---
S1e	yes	yes	no	75–300	150 ± 37	2.4–5.4	3.9 ± 1.1
S2	n.d.	n.d.	n.d.	n.d.	---	---	---
S2e	yes	yes	no	38–121	67 ± 13	---	---
S3	n.d.	n.d.	n.d.	n.d.	---	n.d.	---
S3e	yes	yes	no	37–84	63 ± 10	----	---
S4	n.d.	n.d.	n.d.	n.d.	---	n.d.	---
S4e	no	no	yes	n.p.	---	≈15 → 50	n.d.
S5	n.d.	n.d.	n.d.	n.d.	---	n.d.	---
S5e	yes	yes	no	65–207	111 ± 20	2.3–6.5	3.9 ± 1.3
S6	yes	no	no	108–496	262 ± 66	n.p.	---
S6e	yes	no	no	32–139	64 ± 17	n.p.	---
S7	yes	no	no	124–540	283 ± 112	n.p.	---
S7e	no	no	yes	n.d.	---	62–300	132 ± 40
S8	yes	yes	no	56–178	115 ± 26	(1.3) not real framb.	n.d.
S8e	yes	no	no	51–156	92 ± 18	n.p.	---
S9	yes	yes	no	74–300	150 ± 37	3.5–6.5	5
S9e	yes	yes	no	74–300	150 ± 37	3.5–6.5	5
S10	n.d.	n.d.	n.d.	n.d.	---	n.d.	----
S10e	no	no	yes	n.d.	---	1.6–10	4.8 ± 1.7
S11	n.d.	n.d.	n.d.	n.d.	---	n.d.	---
S11e	no	no	yes	n.p.	---	5–90	10 ± 2.5
S12	n.d.	n.d.	n.d.	n.d.	---	n.d.	---
S12e	yes	yes	no	44–137	75 ± 16	0.6–5.2	2.2 ± 1
S13	yes	no	no	22–245	75 ± 43	10 - 20	n.d.
S13e	yes	no	no	26–245	82 ± 44	0.25 - 2.5	n.d.
S14	yes	yes	no	20–60	38 ± 9	0.7–4	2.2 ± 0.8
S14e	yes	yes	no	20–60	36 ± 8	1–4	2.6 ± 0.8

When calcite was present in the samples, cubic crystals could be observed in between the framboids. For samples of pure calcite, framboids and spheres were no longer observed (Figure 4.12). The exception was solid S13. XRD analysis showed that this solid consisted of 100 % calcite (Table 4.3), yet mainly spherical particles were observed by means of SFEG-SEM (Figure 4.13). Two additional, otherwise very rarely occurring, morphologies were found in this sample: needle-like structures (Figure 4.13), as well as bigger spherical aggregates with diameters on the order of

10 µm (Figure 4.14). These bigger spheres were different from the previously described framboids, in that they were not built up of smaller spheres. Rather, these spheres were more massive, with plate-like sub-crystals.
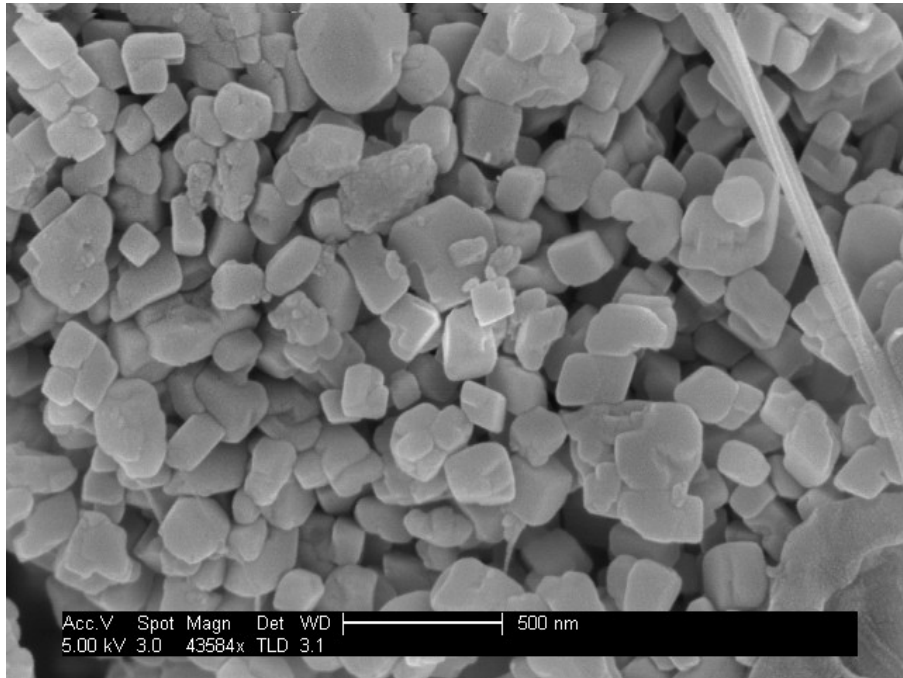
Figure 4.12: SEM photograph of sample S7e. This sample consists of 100% calcite and no framboids/spheres are present.
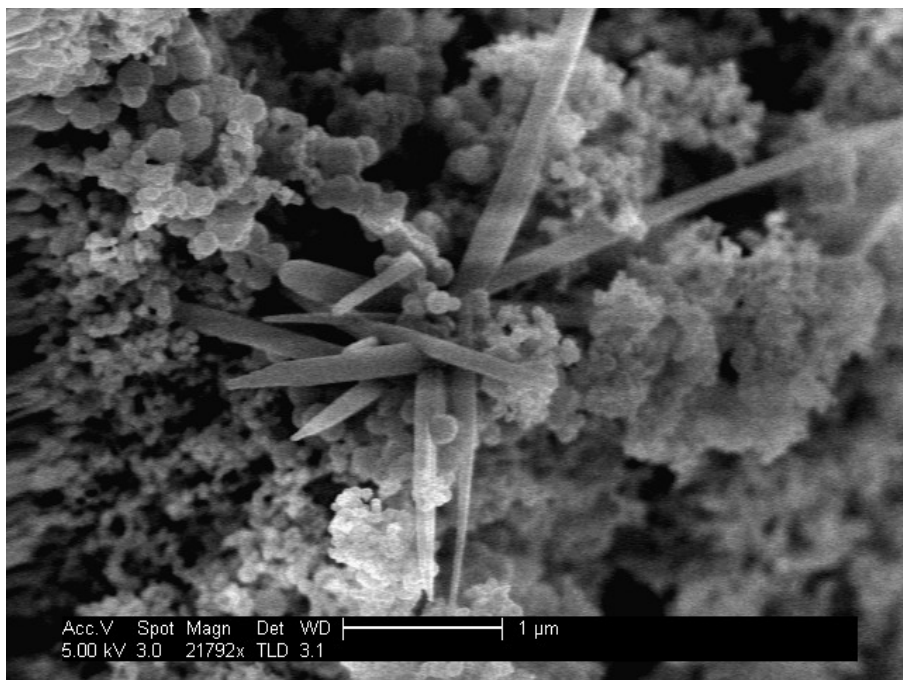
Figure 4.13: SEM photograph showing needle-like structures in solid S13. The dominant morphology observed in this sample is that of little spheres like the ones around the needles.
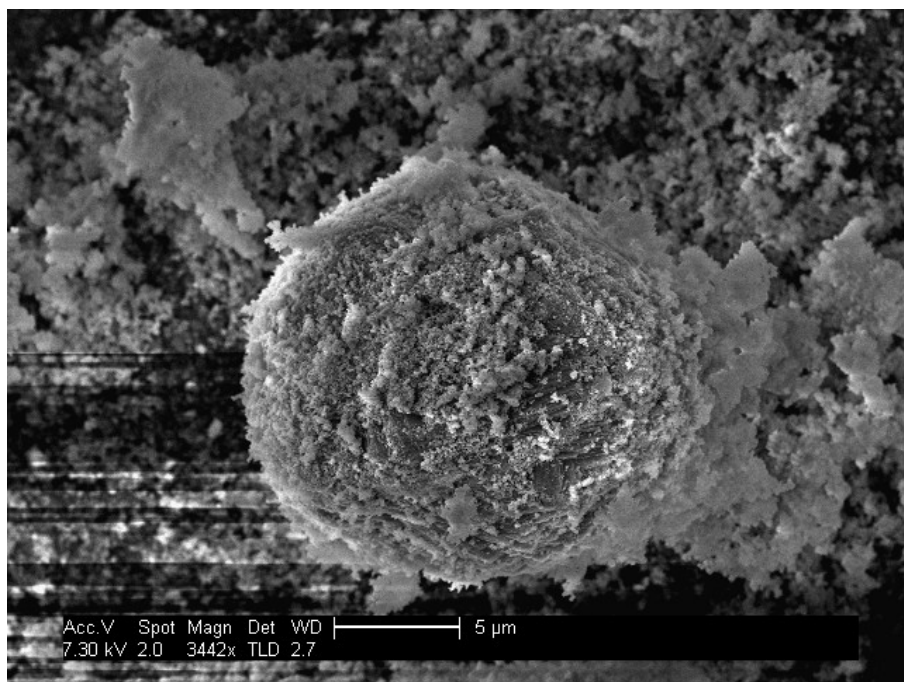
Figure 4.14: SEM photograph of sample S13. This picture shows a massive spherical aggregate built of platelets.

4.3.3 Framboid Formation

The SFEG-SEM investigations of the 14 solids (S1–S14) confirm that vaterite has the tendency to form framboidal structures. These framboidal structures are aggregations of smaller, mostly spherical, particles. The average size of these elementary spheres differs from one precipitation experiment to the other, and is typically comprised between 36 and 150 nm (Table 4.4). The average size of framboids varies between 2.2 and 3.9 µm. The latter size range is in good agreement with that reported in the literature (Table 4.1). Brečević et al. (1996) calculated from XRD measurements a crystallite size between 25 and 35 nm in vaterite aggregates of approximately 4 µm in diameter. As no detailed information on the morphology is given by Brečević it is not possible to say if these crystallites are identical to the spheres described in this work.

The observations raise the question why and when the observed framboidal structures form. The first part of this question, why do framboidal structures form, is difficult to answer. Little is known about the mechanisms leading to the formation of framboidal structures. Framboid formation is also known for other mineral systems. For example, Butler and Rickard (2000) describe framboidal pyrite formation, and Wolthers (2003) discusses framboidal pyrite structures (Figure 4.15).
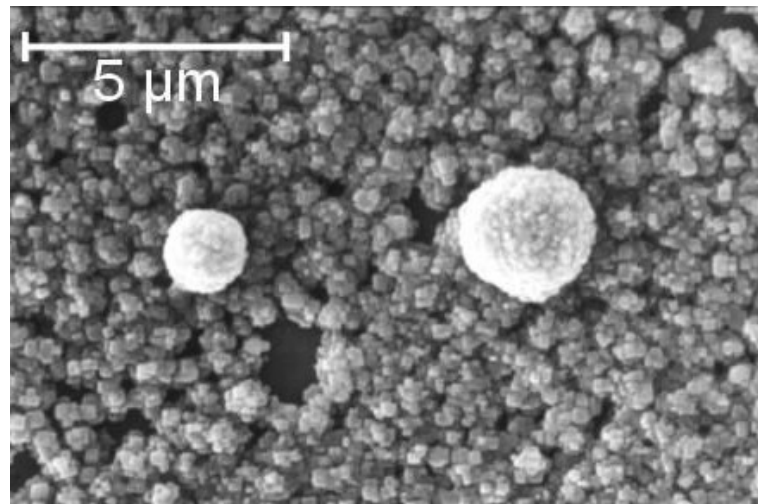
Figure 4.15: Pyrite framboids (from Wolthers, 2003)).

Butler and Rickard (2000) proposes a mechanism where nucleation of new crystals occurs <u>on the surface</u> of the framboids, in systems with high degrees of supersaturation (S). However, even if pyrite framboids show remarkable similarities with the structures observed for vaterite, the data presented here suggest a different mechanism of formation.

We propose the mechanism illustrated in Figure 4.16, where the first $CaCO_3$ nuclei form at the interface between the solution and a CO_2 gas bubble (A). At the interface, OH^- diffusing from the solution reacts with CO_2 to form HCO_3^- ions. The latter then combine with Ca^{++} ions to form $CaCO_3$. The overall reaction can be written as $Ca^{2+}_{(aq)} + CO_{2\ (g)} + 2\ OH^-_{(aq)} \rightarrow CaCO_{3(s)} + H_2O_{(l)}$. A fast growth of the spherical crystals will lead to a depletion of the solution around the crystallites and the crystallites will stop to grow. The formation of spherical structures is typical for transport-controlled reactions (Lasaga, 1998). If the reaction is halted at this early stage, then only individual spheres are formed. This is consistent with the observations on solid S6 (Figure 4.11). Experiment S6 was terminated as soon as

the solution became cloudy and, indeed, no framboidal aggregates formed (the typical small spheres are present, however).
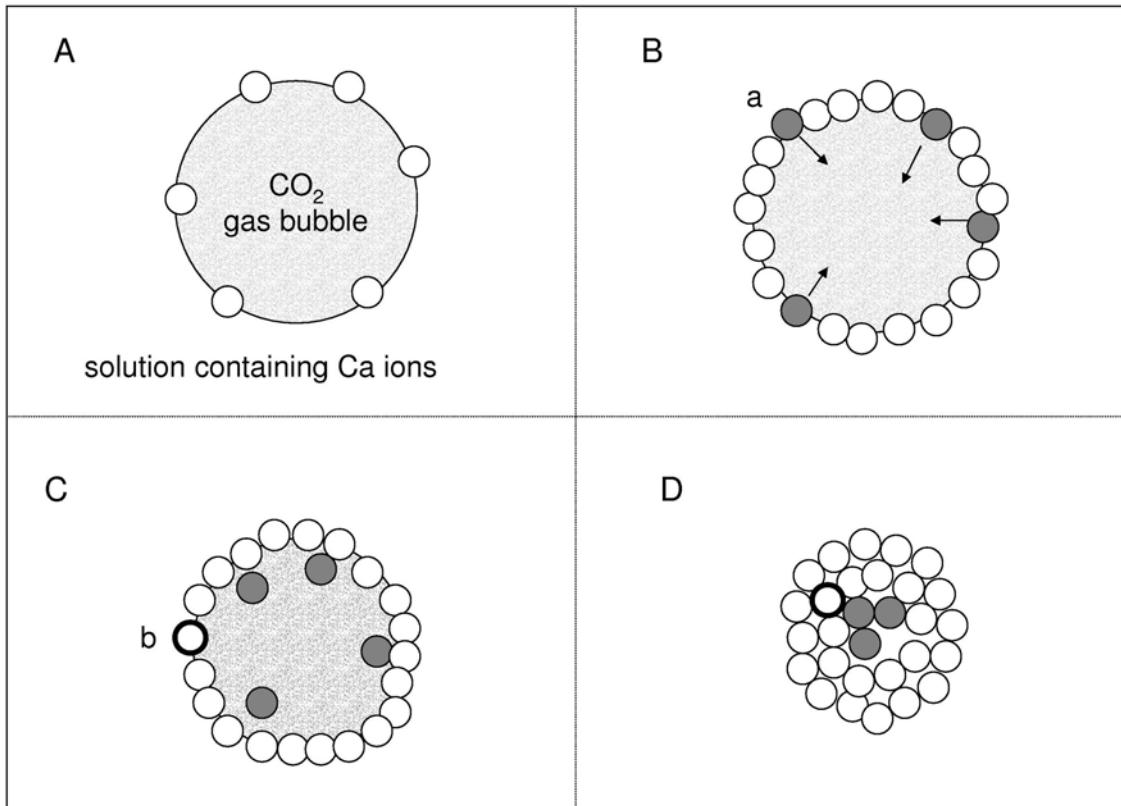
Figure 4.16: Illustration of the hypothesized nucleation mechanism leading to the formation of framboidal aggregates. A) The first spherical particles nucleate at the interface between the solution and the CO_2 gas bubble. B) During nucleation CO_2 is consumed resulting in a decrease of the gas bubble size. The consequence is that some particles (a) are transported into the gas bubble. C) On the interface new particles (b) can form. D) The final state, when all CO_2 is used up, is a framboidal aggregate.

If the nucleation process is not disturbed, it will proceed and lead to a complete occupation of the gas bubble interface (Figure 4.16, situation B). Since during nucleation and growth CO_2 is used up the gas bubble will shrink. Thereby some particles can be pushed to the inside of the gas bubble (particle "a", situation B in Figure 4.16). As the gas bubble collapses, new crystals continue nucleating along the "free" interface (particle "b", situation C Figure 4.16). The process stops when all CO_2 is used up and a framboidal aggregate has formed. Broken vaterite framboids as shown in Figure 4.17 clearly show that the center of the framboidal aggregates is built up by the same small particles as the outer part.
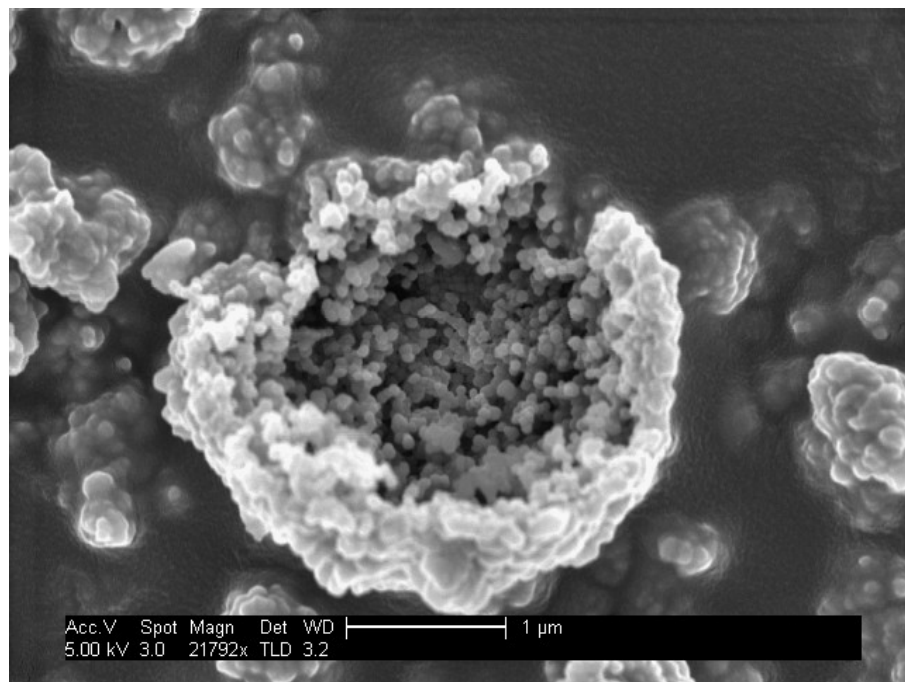
Figure 4.17: SEM picture of an "open" framboidal vaterite aggregate.

A CO_2 bubble of approximately 14 μm in diameter contains the necessary amount of C needed to form a vaterite framboid of 4 μm in diameter. This is calculated using the following parameters: vaterite density of 2.54 g cm^{-3}, framboid porosity of 30%, gas pressure inside the gas bubble equal to that outside the gas bubble (10^5 Pa), and a volume of 22.4 dm^3 per mol CO_2. The sizes of the CO_2 gas bubbles leaving the fritted gas bubbler (see Section 4.2.1) are difficult to constrain. It is possible that the size of CO_2 gas bubbles varied among the different experiments. This could explain some of the observed variability in the size of spheres and framboids (Table 4.4).

To verify the proposed mechanism it would be necessary to demonstrate that in the absence of CO_2 gas bubbles vaterite form no framboidal structures. Unfortunately, solid S13, which was produced via method **m3** (no CO_2 bubbling) consisted entirely of calcite. Furthermore, as already discussed earlier, the data available in the literature (compiled in Table 4.1) are not detailed enough to provide insight into vaterite framboid formation without further investigations using high resolution SEM imaging techniques. During formation, aggregates may collide and break apart. This is consistent with the observation that not only framboidal structures are present in the investigated samples. As mentioned before, a fraction of the

samples is always present in form of non-aggregated spherical particles (e.g. Figure 4.5).

Table 4.45 shows that the size ratio between the framboids and the spheres that constitute them is constant. Only solid S14 (precipitated while the tip of a sonifier was submerged into the solution) exhibited a smaller size ratio. The constant size ratio observed could imply that the number of nucleation sites per gas bubble is constant. As mentioned earlier on, a detailed investigation of the reactions at the gas-liquid interface would be required to get a better understanding of the processes leading to framboid formation. Based on the observations gathered in this study it appears that a regulation of the CO_2 bubble size may be crucial in this respect. Although not fully explained, it is an intriguing observation that the size ratio between the spheres and the framboids that constitute them seems to be constant.

Table 4.5: Ratio between the sphere size and the size of the framboidal structure.

solid	Size ratio spheres : framboid
S1	1 : 25
S3	1 : 25
S5	1 : 28
S9	1 : 28
S12	1 : 28
S14	1 : 60

Spherical and cubic morphologies were not the only ones observed. Figure 4.13 shows an example of needle like structures. This morphology has never been described for vaterite or calcite precipitates, but is typical for aragonite. That aragonite was not detected using XRD is most likely due to its low concentrations in the solid.

4.3.4 Particle Size and Surface Area

Kinetics of mineral transformation processes depend on the specific surface area of the solids involved. A variety of different methods exist to measure the specific surface area of solids. Depending on the characteristics of the solid, the surface area measured can vary significantly depending on the method used. For a detailed account on this issue the reader is referred to (Allen, 1999). As most methods require at least one gram of solid it was not possible to directly measure the surface area of the precipitates synthesized in this study. However, since the vaterite framboids described are built up of nearly spherical particles, it is possible to estimate the geometric specific surface area of the solids. Assuming that the solid consists of spheres of uniform size, the specific (geometric) surface area (A_{sol}) of the solid can be derived from the solid density (2.54 g cm^{-3} for vaterite):

$$A_{sol} = \frac{\frac{1}{\rho}}{\frac{4}{3}\pi\left(\frac{d_{sph}}{2}\right)^3} * 4\pi\left(\frac{d_{sph}}{2}\right)^2 \qquad (4.1)$$

where A_{sol} is the specific surface in m^2 g^{-1}, ρ the density of the solid in g cm^{-3}, and d_{sph} the diameter of the spheres in µm.

Surface roughness and porosity may significantly contribute to the effective surface area of a solid. As Equation 4.1 does not take into account these effects, the values obtained are expected to be lower than those measured by, for example, BET surface measurements. However, for the solids described in this work, SEM analyses show that the smallest particles are of similar size and morphology (see Figures 4.6, 4.8, 4.9, and 4.10), Equation 4.1 can still be used to illustrate relative differences in surface area. Figure 4.18 indicates that below a diameter of 0.1 µm a small decrease in particle size leads to an exponential increase in specific surface area.

Unfortunately, few measured values of the specific surface area of vaterite are available. A value for the specific surface area of vaterite is given in only one of the references cited in Table 4.1. In this publication, A_{sol} = 7.2 m^2 g^{-1} is reported for spherical vaterite particles with sizes between 4 and 6 µm (Plummer and Busenberg,

1982). A specific surface area of 7.2 m^2 g^{-1}, however, corresponds theoretically to a spherical diameter of 0.32 µm. This value (0.32 µm) is of the same order of magnitude as the particle sizes of the elementary spheres obtained in this study (Table 4.4). Thus, the particle sizes reported in Plummer and Busenberg (1982) correspond most likely to aggregates (framboids).
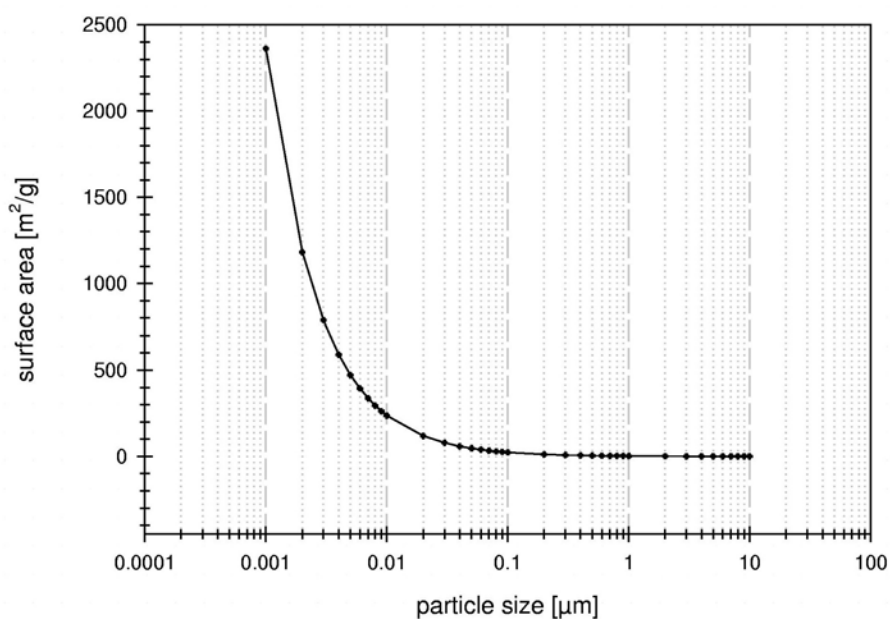
Figure 4.18: Theoretical specific surface area of spherical particles (in m^2 g^{-1}) with a density of 2.54 g cm^{-3} (vaterite), calculated with Equation 4.1.

For the solids used in this study (S1–S14), the calculated A_{sol} values are between 15 m^2 g^{-1} (solid S1) and 85 m^2 g^{-1} (solid S14). For three of the samples (S1, S2, and S14) the predicted specific surface areas are illustrated in Figure 4.19. The error bars indicated correspond to the errors in size determination as given in Table 4.4.
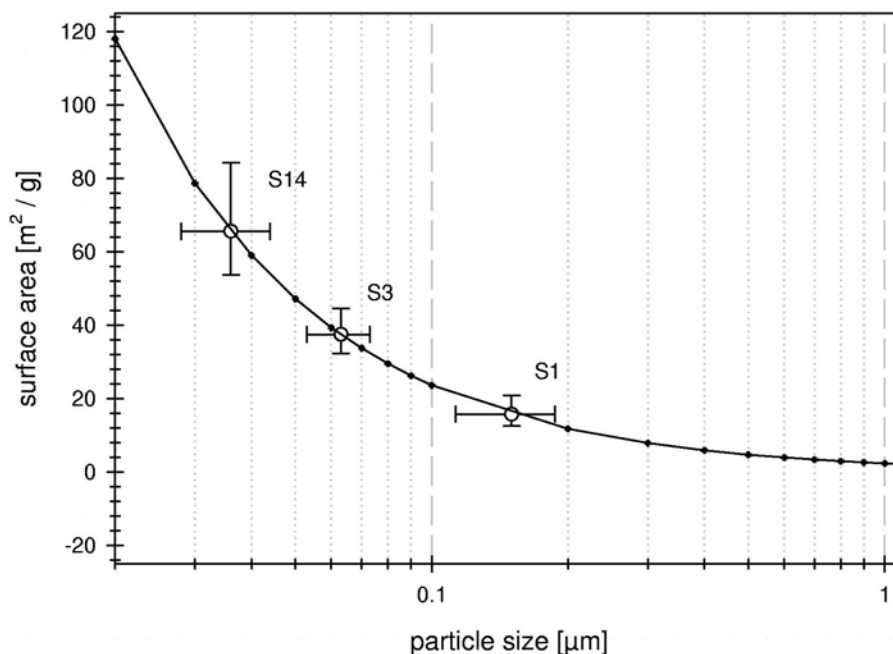
Figure 4.19: Calculated specific surface areas for three of the precipitated solids.

4.4 Synthesis

Vaterite crystals described in this work show a tendency to form framboidal aggregates built of small "spheres". Geometric surface areas estimated from the sizes of the elementary spheres are between 15 m^2 g^{-1} and 85 m^2 g^{-1}. One of the solids (S13) exhibited the morphology of small spheres but was identified as calcite by XRD analysis. This finding demonstrates that is not always possible to distinguish between vaterite and calcite solely based the particle morphology.

A mechanism leading to the formation of framboidal vaterite aggregates, based on a nucleation process starting at the gas-liquid interface of a CO_2 gas bubble, is proposed. The use of CO_2 to precipitate vaterite may be the key element in the formation of vaterite framboids. Since CO_2 gas is often used in laboratory studies of vaterite formation and its subsequent transformation to calcite, the next chapter will focus on how the framboidal morphology influences the vaterite to calcite transformation kinetics.

Furthermore, SEM micrographs of one solid (S13) revealed the presence of small amounts of needle like crystals, even though XRD measurements only detected calcite. The needle like crystals are most likely aragonite. This observation

is in of interest since it demonstrates that within the same precipitation vessel different phases can form simultaneously. This contradicts with the general assumption that under a given set of physico-chemical conditions only one polymorph is formed.

5 Vaterite and its Transformation to Calcite

5.1 Introduction

Vaterite, a calcium carbonate ($CaCO_3$) polymorph, is unstable under Earth-surface conditions and transforms rapidly into the more stable calcium carbonate polymorph calcite. Vaterite does not occur in the environment in significant amounts, but can play an important role as precursor in calcite formation at high supersaturation, as often used in calcite precipitation experiments.

Laboratory experiments can be a powerful tool to elucidate natural processes, such as trace element incorporation during calcite formation. To reveal the underlying mechanisms, however, it is often necessary to alter the physico-chemical conditions beyond the range typically observed in the natural environment. In the present chapter, the mechanism and rate of framboidal vaterite transformation is investigated. To this end, the changes in solution chemistry, mineralogy plus solid morphology are monitored during the transformation process. Changes in solution chemistry are used to determine changes in the saturation state of the system with respect to vaterite and calcite, and therewith follow the evolution of the vaterite dissolution and calcite growth rates. The changes in the phase composition are used to determine net conversion rates at different stages along the transformation process.

5.2 Experiments

5.2.1 Materials and Methods

The solids used in the experiments described here are the framboidal vaterite aggregates characterized in Chapter 4. These framboids are about 4 µm and consist of smaller particles of about 100 nm in size. Their composition and morphology are presented in Tables 4.3 and 4.4 of the previous chapter. The solid phases were characterized by means of powder X-Ray Diffractometry (XRD), on a Philips PW 1700. The samples were measured at 40 kV and 30 mA using Cu-Kα radiation at a scanning speed of 0.02° 2θ s^{-1} and a time constant of 1 s. Analytical details on data processing and calibration can be found in the preceding chapter (sections 4.3.1 and 4.3.2).

The morphology of the solids was characterized by means of a High Resolution Scanning Electron Microscope equipped with a Field Emission Gun filament (SFEG-SEM, XL30 Philips/FEI®). Samples were fixed with double sided carbon tape on aluminum stubs and coated with 6 nm Platinum/Palladium using a Cressington® 208HR sputter coater combined with a Cressington® mtm20 thickness controller. The "Through the Lens Detector" (TLD) was used when operating in high–resolution mode. Details on the image processing can be found in Section 4.2.2.

In addition, the SFEG-SEM was equipped with a Nordlys® CCD camera and HKL Technology® software, which made it possible to get diffractions patterns from areas in the sub-micrometer range. Electron back scatter diffraction (Electron Back Scatter Diffraction, EBSD) occurs when elastically scattered electrons, generated in the interaction volume of a sample become channeled, or preferentially absorbed, by the crystalline structure. This occurs at angles close to the Bragg condition. When a stationary beam is focused at a point in a single crystal, characteristic cones of diffraction are created that have many similarities to Kikuchi patterns in Transmission Electron Microscopy (TEM). The channeling effect is very weak and only those electrons escaping through the uppermost layer (~100 nm) of a material can be detected (Dingley and Randle, 1992). The intersection of the diffraction cones with a flat phosphor screen gives a pattern of bands. The band widths are equal to twice the Bragg angles. EBSD requires a flat, finely polished surface. Preparation of

appropriate powder thin sections is technically very demanding. Therefore thin sections, slightly coated with carbon, of solid S1 (sampled during a transformation experiment) were prepared to test if EBSD measurements on the solids used in this work was possible. This was done by preparing cylinders of about 10 mm diameter of a resin/powder mixture. Afterwards, the hardened cylinders where glued on a glass slide and polished.

5.2.2 Transformation Experiments

The main goal of the experiments was to determine the mechanism and kinetics of transformation of the vaterite framboids into calcite. To reveal the processes operative during this transformation, three different series of experiments were performed. The two first sets of experiments focus on the mineralogical changes during transformation, as well as on the influence of the solid-to-solution ratio and stirring rate on the rate of calcite formation. In the third series of experiments, changes of the solution during transformation are also investigated. The impact of stirring rate and solid-to-solution ratio are evaluated in these experiments.

In the first series of experiments, vaterite was mixed with reverse osmosis water (conductivity below 0.067 µS) in 40 ml PTFE (Savilex$^®$) vessels using different solid-to-solution ratios. Every hour a sample of 1 ml was taken using an Eppendorf$^®$ pipette after homogenizing the suspension by turning the vessel upside down. The sample was filtrated through a 0.2 µm pore size filter, after which the sample was washed with ethanol and dried under vacuum for 10 minutes. All samples were stored in a desiccator containing silica gel. The experimental solids were further investigated by means of XRD and SFEG-SEM. This series of experiments is referred to as exp1 (Table 5.1).

In the second series of experiments, exp2, a number of 4 ml polypropylene sampling vials were filled with mixtures of vaterite and reverse osmosis water. This was done for two different solid-to-solution mass ratios (Table 5.1). Every hour the total content of one of the vials was filtrated through a 0.2 µm pore size filter using a vacuum flask. The drying procedure was the same as for exp1. In the experiments referred to as exp2$_s$, the sample vials were left standing during the experiments (no agitation), whereas in the experiments referred to as exp2$_r$, the vials were rotated

(overhead) at a rate of 10 rpm. Details on the experimental series exp1 and exp2 can be found in Table 5.1.

Table 5.1: Experimental parameters for vaterite transformation experiments in reverse osmosis water (conductivity below 0.067 µS) (all experiments are performed at 25°C).

solid : solution mass ratio	mass of solid (g)	experiment label	experimental procedure	rotated overhead	solid used*
1 : 30	1.0	vattrans01	exp1	no	S1
1 : 125	0.26	vattrans02	exp1	no	S1
1 : 250	0.12	vattrans03	exp1	no	S1
1 : 40	0.1	vattrans04	exp2$_r$	10 rpm	S3
1 : 40	0.1	vattrans05	exp2$_s$	no	S3
1 : 100	0.04	vattrans06	exp2$_r$	10 rpm	S3
1 :100	0.04	vattrans07	exp2$_s$	no	S3
1:40	0.1	vattrans08	exp2$_r$	10 rpm	S14
1:40	0.1	vattrans09	exp2$_s$	no	S14

*See Chapter 4 for detailed description of the solids.

In the third series of experiments, referred to as exp3, vaterite was added to a 360 ml Teflon vessel containing 200 ml of a 0.1 M KCl solution (to minimize changes in the solution electrolyte composition during the transformation process). In this series of experiments the transformation process was followed by monitoring the changes in solution composition. The reaction vessel was placed in a thermostated (25°C) double-walled water jacket and the solution was stirred using a PTFE (Nalgene$^{®}$) floating stir bar. The experiments were performed at different stirring speeds to investigate the influence of stirring on the transformation rate (Table 5.2).

Table 5.2: Experimental conditions for vaterite transformation experiments in 0.1 M KCl of type exp3.

experiment label	solid used	mass of solid (g)	stirring (rpm)
Vatdis01	S14	0.1013	300
Vatdis02	S14	0.0522	300
Vatdis03	S14	0.2027	300
Vatdis04	S14	0.2293	300
Vatdis05	S14	0.1307	900
Vatdis06	S1	0.4839	300
Vatdis07	S1	0.1087	300
Vatdis08	S3	0.104	300
Vatdis09	S3	0.0932	300
Vatdis10	S3	0.1082	600
Vatdis11	S3	0.1055	600

The pH and Ca concentration of the solution during the transformation experiments were monitored by means of a pH electrode (Radiometer®, model HG201 with reference REF201) connected to a pH meter (Orion® A 520), and a Ca sensitive electrode (Orion®, 9700BN) connected to a second pH meter (Orion® A 520). The analog output of the two pH meters was fed into a Digital Multi Meter (DMM) (Keithley® 2000). All data were transferred via an IEEE interface to a personal computer (PC) and processed by a custom-written Visual Basic V5.0 computer code. In addition, sub-samples were taken and analyzed by means of Inductively Coupled Plasma-Optical Emission Spectroscopy (ICP-OES) after filtration of aliquots of suspension through a 0.2 µm pore size filter.

5.3 Results

5.3.1 Phase Transformation

5.3.1.1 Transformation Followed by XRD

As described in section 5.2.2, different sets of experiments were conducted to follow the transformation of vaterite into calcite by means of XRD (Table 5.1 and Table 5.2). Calcite wt. % was calculated from the areas of the main diffraction peaks of vaterite and calcite, using the computer program Xfit (Cheary and Coelho, 1996) (for details see 4.2.2). The results of experiments exp1 and exp2 (Figure 5.1 and Figure 2), show an increase of calcite with time and higher transformation rates at the beginning of the experiments and at higher solid-to-solution ratios. Rotation of the suspensions increased the transformation rate of solid S3 (Figure 2), but not of solid S14 (Figure 5.3).
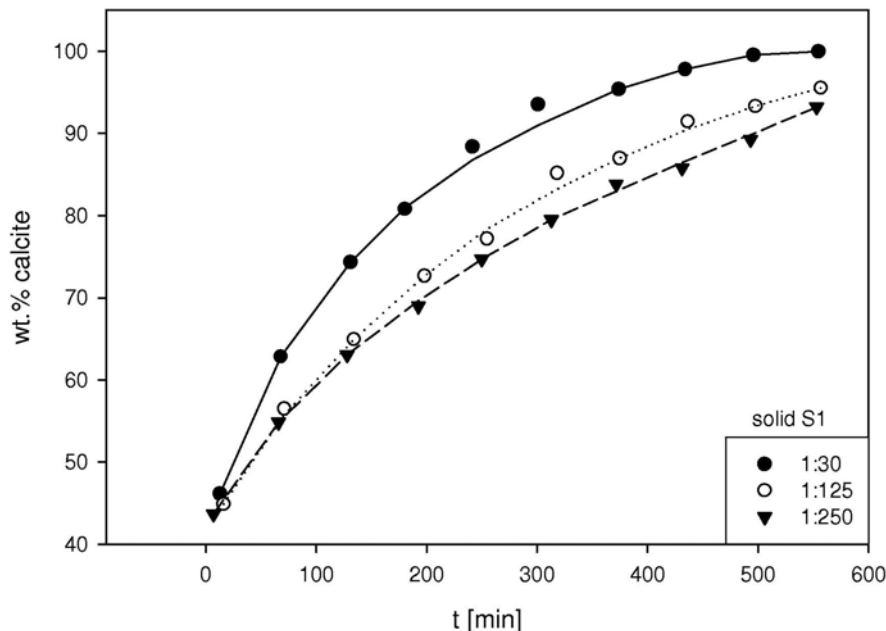
Figure 5.1: Time dependent change in calcite concentration for different solid-to-solution mass ratios (experiments vattrans01 – 03; for details see Table 5.1).
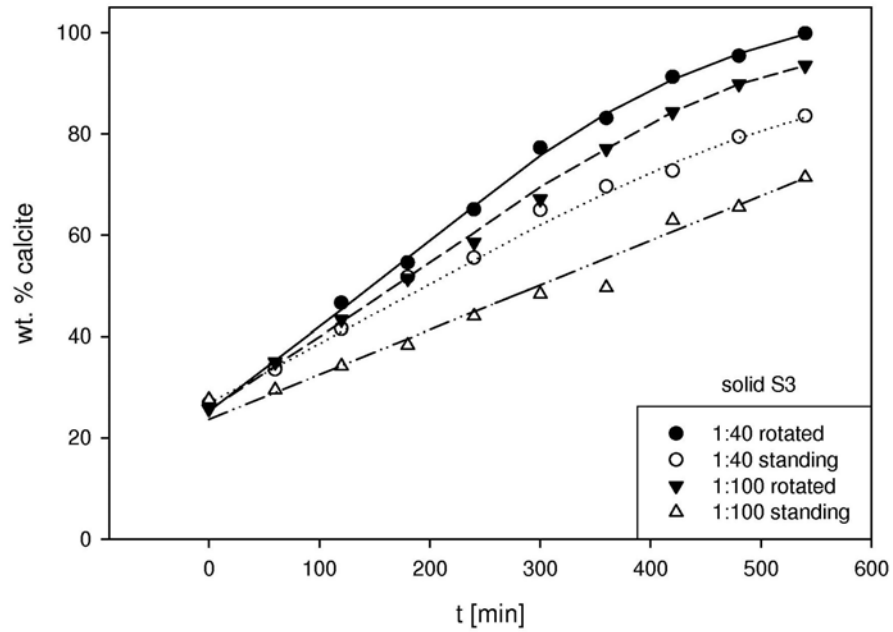
Figure 2: Time dependent change in calcite concentration for different solid-to-solution mass ratios, in rotated and non-rotated experiments (vattrans04 – 07; for details see Table 5.1).
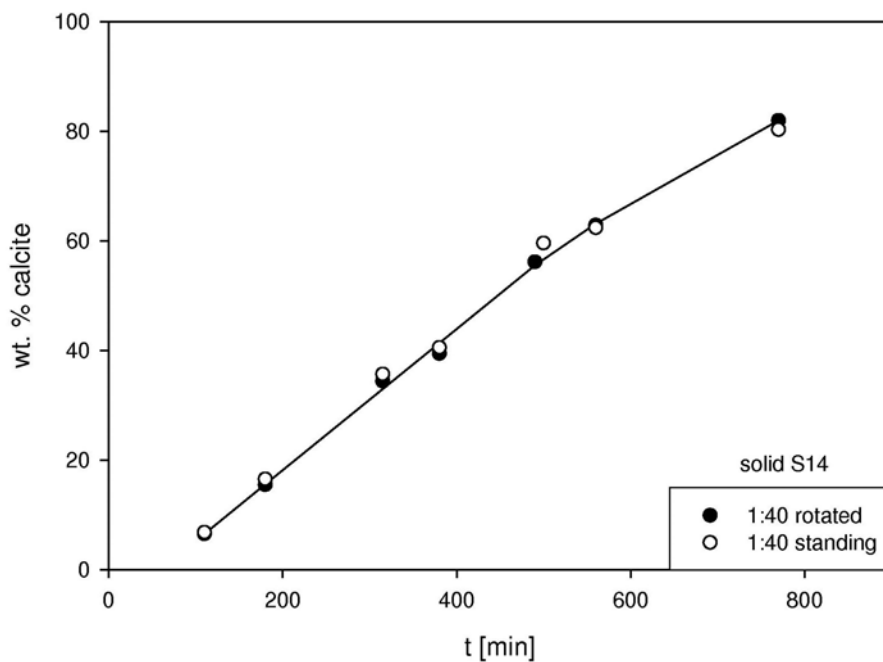
Figure 5.3: Time dependent change in calcite concentration for rotated and non-rotated experiments (vattrans08 and 09; for details see Table 5.1).

The transformation rate (R_x in $g_{calcite}$ g_{tot}^{-1} s^{-1}.) for every sampling interval dt_x was calculated using the smoothed XRD data from experiments vattrans01 – 09 (Figure 5.1 - Figure 5.3),

$$R_x = \frac{dw_x \cdot 100}{w_t \, dt_x} \tag{5.1}$$

where dw_x denotes the mass of calcite produced during the time interval dt_x relative to the total solid mass. The results of these calculations are presented in Figure 5.4. The data show that the transformation of vaterite into calcite can be divided into two stages. Up to approximately 60 wt. % calcite, the transformation rate remains nearly constant, whereas at higher relative calcite concentrations, a decrease in transformation rate can be observed.
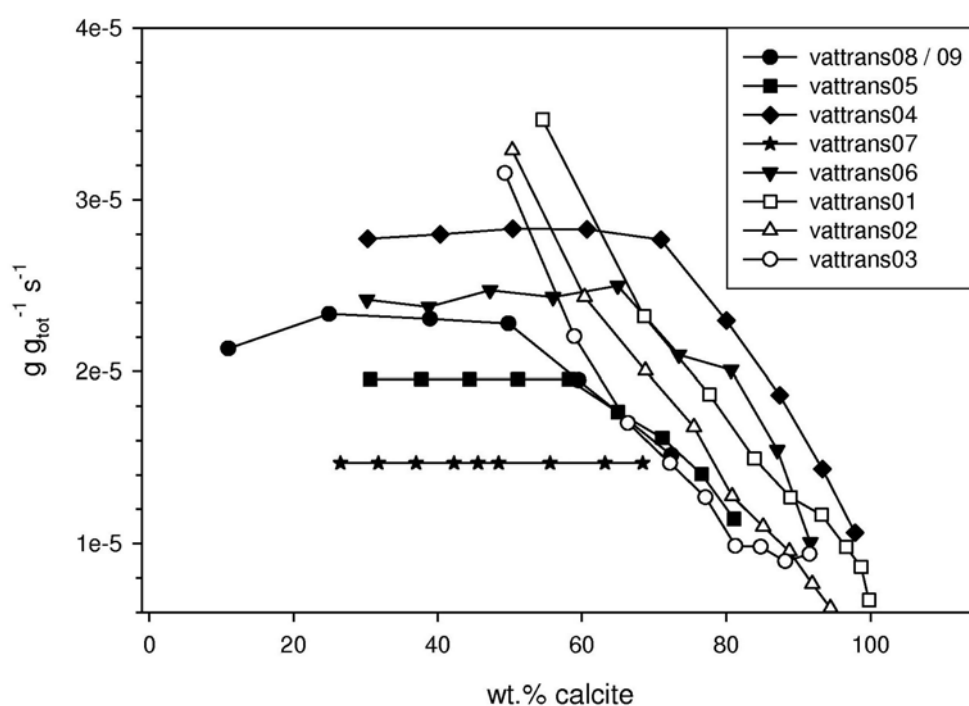
Figure 5.4: Vaterite to calcite transformation rates for the transformation experiments vattrans01 - 09.

5.3.1.2 Transformation Followed by "Inflection Point" Method

In the experiments of type exp3 the pH and $[Ca^{2+}]$ of the solution was monitored. The measured pH increased rapidly (within ~3 minutes) after the addition of vaterite (at time = 0, Figure 5.5), followed by a continuous decrease characterized by a distinct inflection point. The time between addition of vaterite and the inflection point in the curve (x in Figure 5.5) was used as a measure of the time scale of the transformation of vaterite into calcite (Table 5.3). The measured $[Ca^{2+}]$ increased,

except for a drop in concentration that coincided with the inflection point of the pH curve.
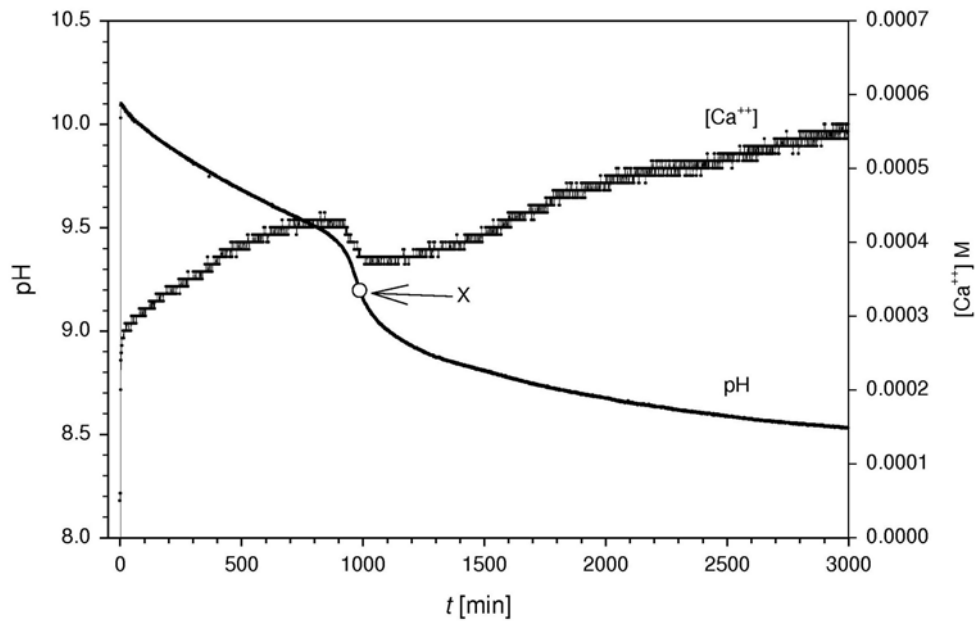
Figure 5.5: Typical changes in the solution pH and Ca^{2+} concentration during the vaterite to calcite transformation (experiment vatdis08), x indicates the inflection point.

Table 5.3: Time scales of vaterite to calcite transformation in experimental series exp3 (for experimental details see Table 5.2).

experiment (solid)	transformation time (h:min)	Experiment (solid)	transformation time (h:min)
vatdis01 (S14)	16:51	vatdis07 (S1)	41:29
vatdis02 (S14)	16:27	vatdis08 (S3)	14:03
vatdis03 (S14)	16:51	vatdis09 (S3)	14:56
vatdis04 (S14)	16:51	vatdis10 (S3)	11:56
vatdis05 (S14)	16:32	vatdis11 (S3)	11:35
vatdis06 (S1)	42:11		

5.3.2 Morphological Changes (SEM)

5.3.2.1 End-Member Morphologies

Vaterite powders used in these experiments consisted of ~60 to ~100 nm particles forming clusters (aggregates) of approximately 4 µm in size. A detailed description of the different vaterite samples used can be found in Chapter 4. The typical morphology of calcite crystals formed from vaterite after transformation are the rhombohedrons shown in Figure 5.6. Strong stirring (900 rpm) during the transformation process led to rhombohedrons exhibiting pentagonal faces (Figure 5.7). Clearly separated calcite crystals, as shown in Figure 5.6 and 5.7, were rarely observed when the solution was stirred during transformation. Stirring typically resulted in the formation of aggregates: Figure 5.8 shows aggregates of calcite rhombohedrons, while Figure 5.9 shows aggregates of calcite crystals with pentagonal faces.
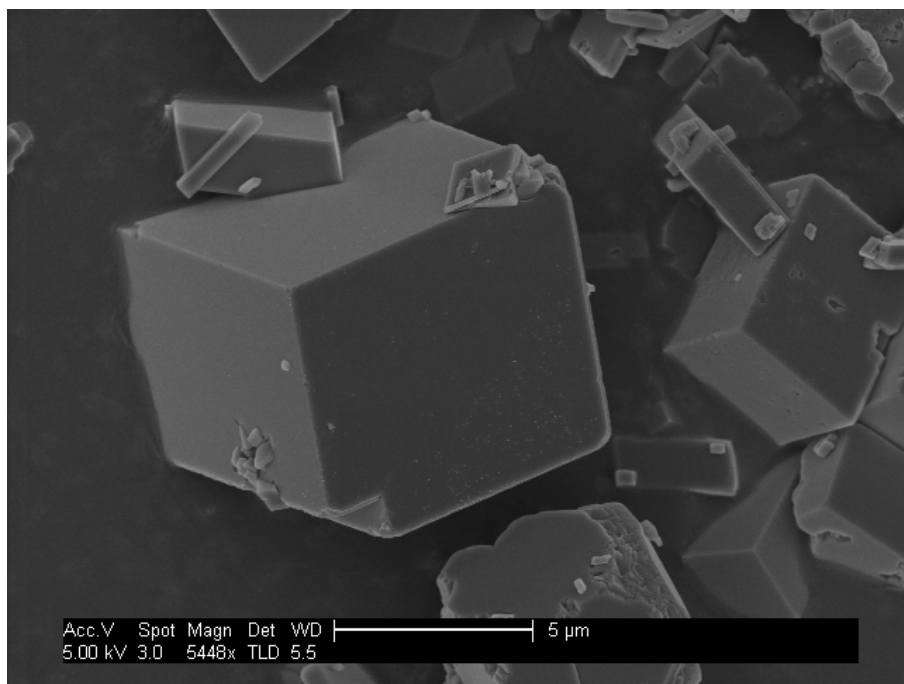
Figure 5.6: Picture of a typical calcite rhombohedron, taken at the end of experiment vatdis03 (300 rpm).
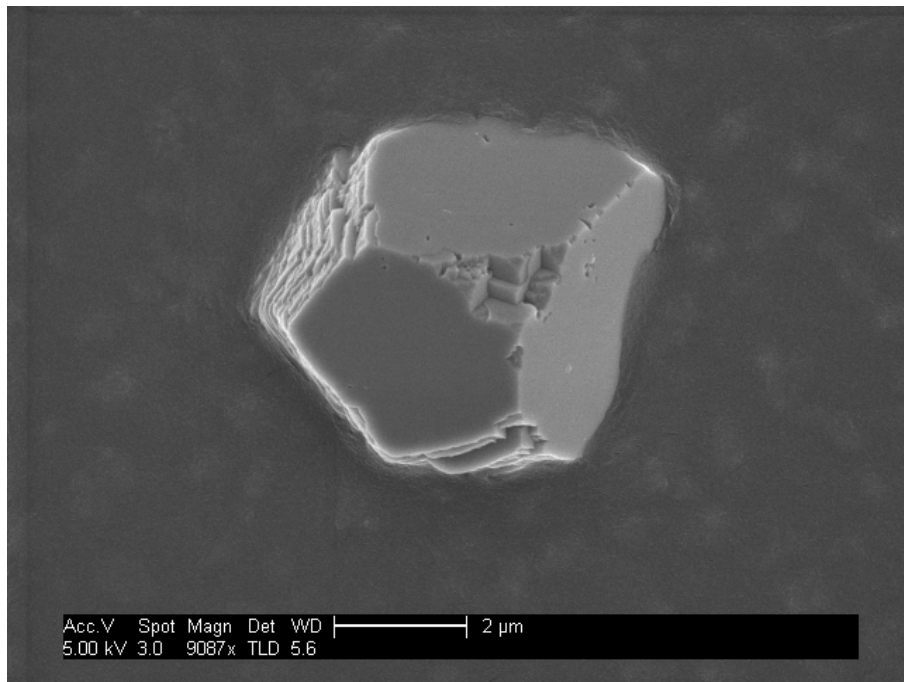
Figure 5.7: Calcite crystal (grown under strong stirring) showing pentagonal faces. Picture taken at the end of experiment vatdis05 (900 rpm).
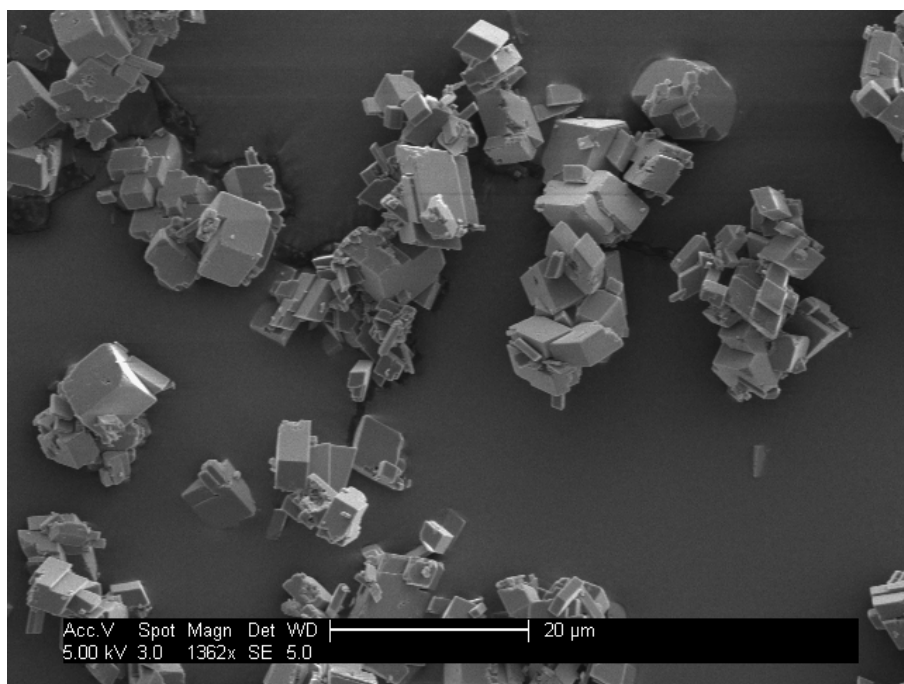
Figure 5.8: Aggregation of calcite rhombohedrons. Picture taken at the end of experiment vatdis01.
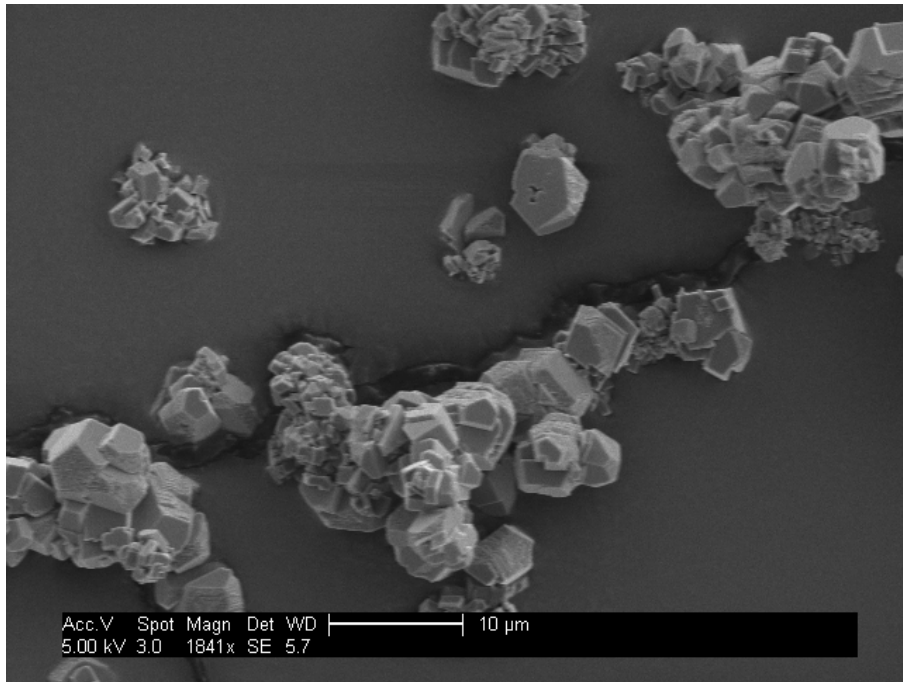
Figure 5.9: Aggregates of calcite crystals showing pentagonal planes. Picture taken at the end of experiment vatdis05.

5.3.2.2 Morphologies Observed during Transformation

The change in morphology during the transformation process was followed for solid S3 in the course of experiment vatdis08. Figure 5.10 identifies the positions of the sampling points (sp) during the transformation process, as well as the observed morphologies (higher magnifications of the SEM micrographs in Figure 5.10 can be seen in the Appendix). In the following the characteristic morphologies are described.

In the suspension, a few calcite rhombohedrons could be recognized early (sp1) during the transformation process (Appendix, Figure 5.18). With ongoing transformation (sp2), these calcite crystals grew into larger ones (Appendix, Figure 5.19).
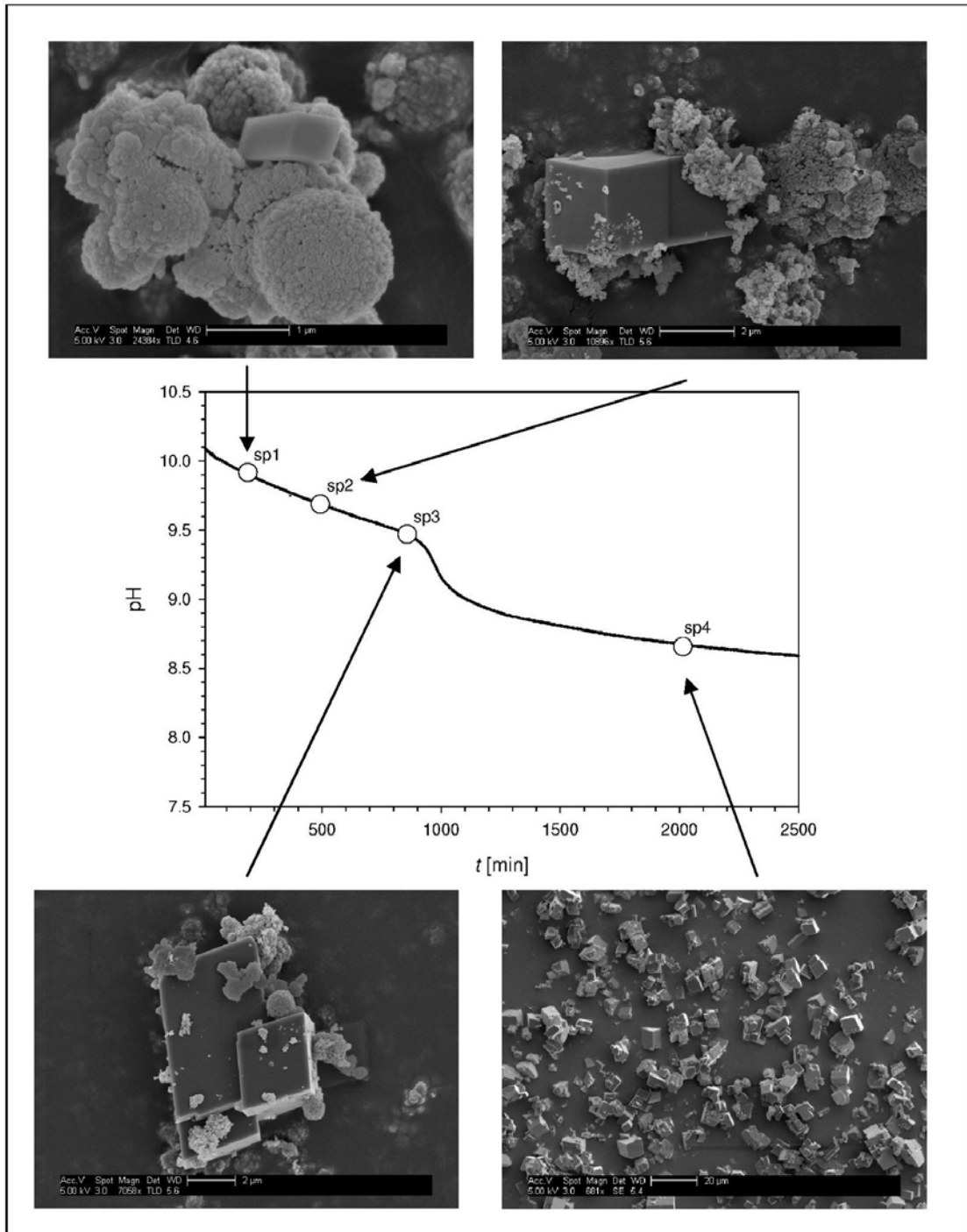
Figure 5.10: Morphological changes observed during the transformation of vaterite into calcite (vatdis08, solid S3).

At sampling point sp3, shortly before the pH inflection point (point x, Figure 5.5), spherical vaterite aggregates were still present in the suspension (Appendix, Figure 5.20 and Figure 5.21). The morphology of the crystals ~2000 min after the start of the experiment (sp4) was characterized by aggregated calcite having an average size of approximately 10 μm (Appendix, Figure 5.22).

In contrast to the morphologies observed in the previously described experiment, Figure 5.11 shows a SEM picture taken during transformation of solid S1 (experiment vattrans01 after 100 min reaction time), an experiment that was not stirred. Different morphologies can be observed in a single sample. The original solid (a, Figure 5.11) coexists with aggregates where small cubes are visible at the surface (b, Figure 5.11), as well as particles where the small cubes have coalesced, giving rise to larger cubic morphologies (c, Figure 5.11). Finally, one also observes calcite crystals with smooth surfaces (d, Figure 5.11).
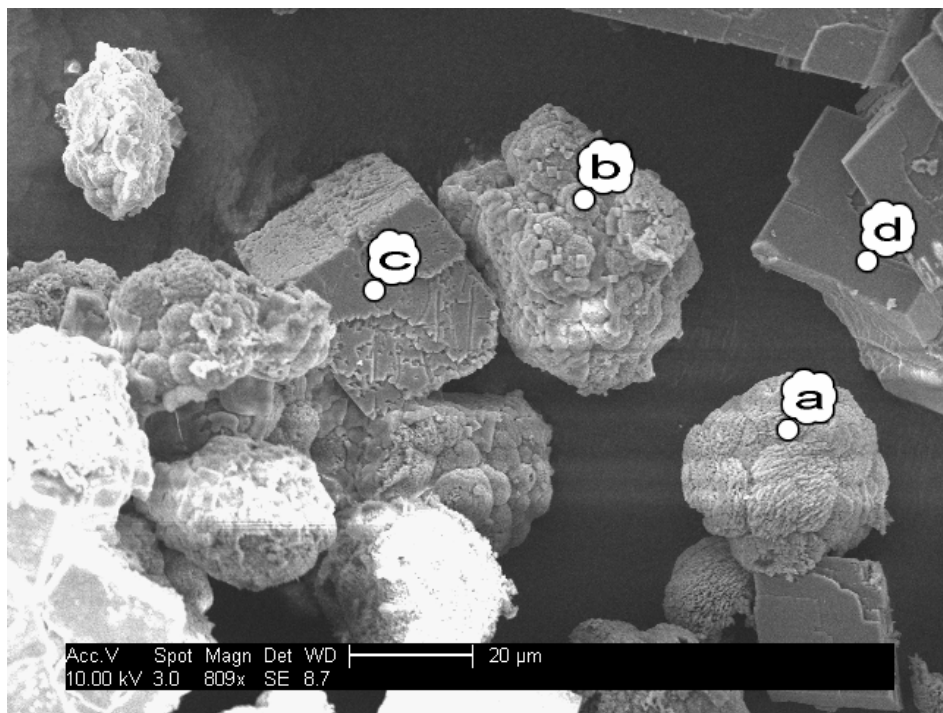
Figure 5.11: SEM photograph taken during the transformation of solid S1 (experiment vattrans01, after 100 min reaction time), unstirred.

XRD analysis indicated that the suspension shown in Figure 5.11 contained approximately 70 wt. % of calcite. A thin section of this sample was prepared for EBSD analysis as described in Section 5.2.1 (Figure 5.12). In the center of the picture a framboidal aggregate directly attached to a solid cubic crystal can be seen. Measurements by means of EBSD show the same crystallographic orientation along the lines marked as A----B (Figure 5.12). This indicates that the cubic particles are single crystals of calcite. A magnification of the framboidal aggregate in the center of Figure 5.12 is shown in Figure 5.13: it exhibits small spheres as well as larger, morphologically distinct, solid structures. These solid structures seem to emerge out

of the smaller spherical particles. EBSD analysis indicate that they consist of calcite. The round particles are most likely vaterite. It was not possible to perform EBSD measurements directly on the spherical particles, because a flat polished surface is necessary for phase identification. But the fact that the bulk of the solid contained 70% calcite and 30% vaterite (XRD), and identification of the larger structures as calcite, suggest that the spherical particles are vaterite.
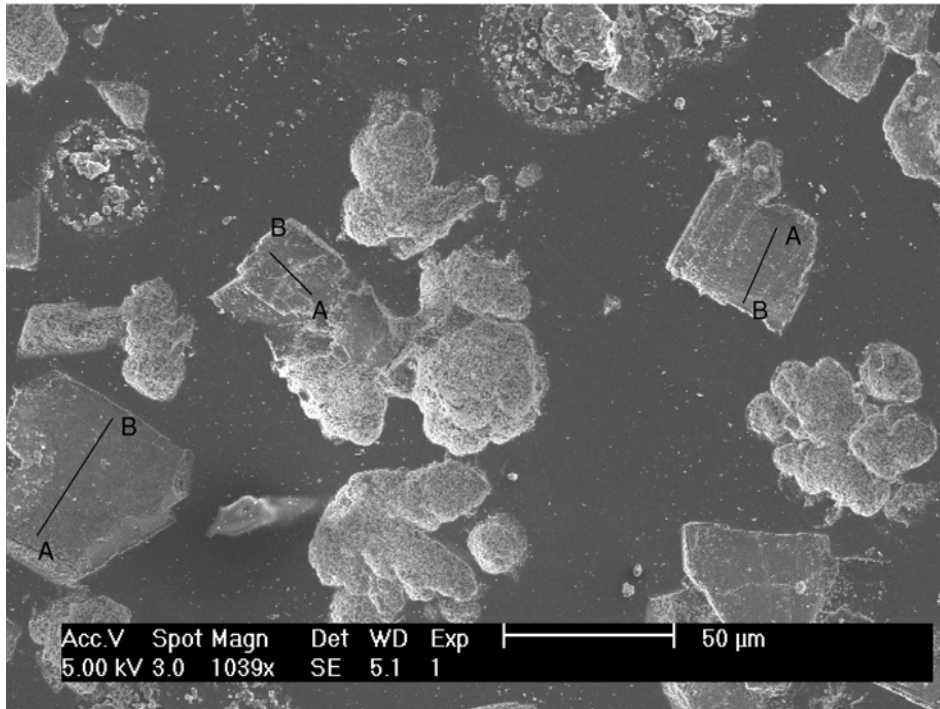
Figure 5.12: Thin section of solid S1 (taken after 100 min. of reaction time during experiment vattrans1, containing approximately 70 wt. % of calcite). Lines A ---B indicate the position of the EBSD measurements.
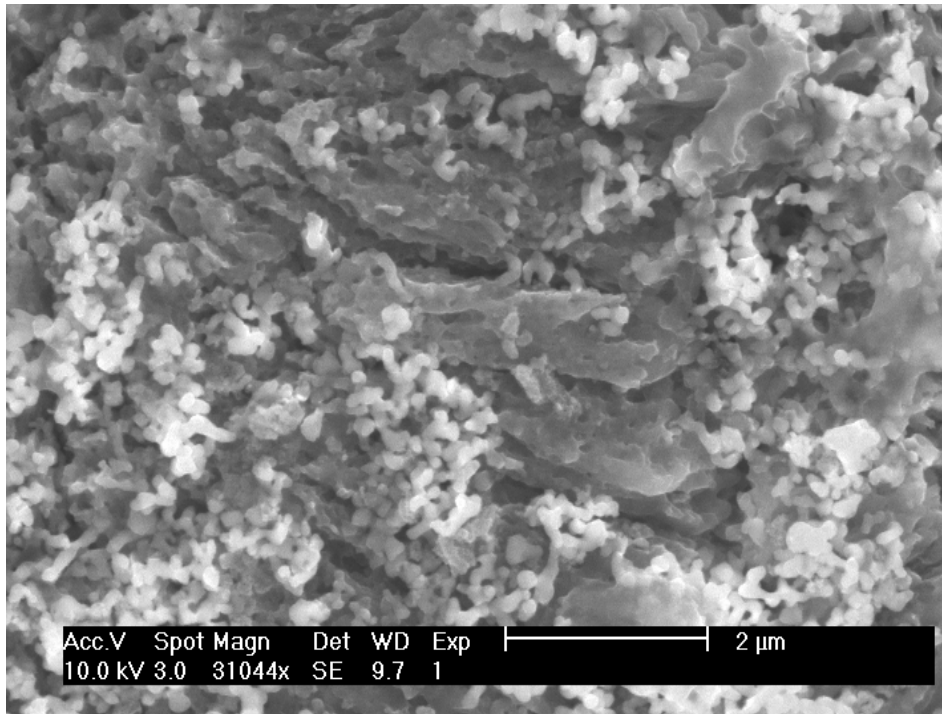
Figure 5.13: Magnification of the framboidal structure seen in the center of Figure 5.12.

5.4 Discussion

5.4.1 Transformation Pathway (SEM Observations)

Visual inspection of the SEM micrographs indicates that vaterite dissolves homogeneously throughout the suspension during the transformation process. Calcite growth, however, occurs in two distinctly different modes: (a) growth of crystals outside the vaterite framboids (Appendix, Figure 5.18 -Figure 5.22), and (b) growth within the vaterite framboids (Figure 5.11 -Figure 5.13). Growth mode (a) is consistent with the vaterite to calcite transformation pathway described in the literature (Kralj et al., 1997). As a result of the dissolution of vaterite, the solution surrounding the framboids becomes oversaturated with respect to calcite, hence creating necessary conditions for the nucleation and subsequent growth of calcite crystals onto the vaterite aggregate. The initial stage of this transformation is nicely illustrated by Figure 5.18, where a calcite crystal is seen growing on a vaterite framboid.

Growth mode (b) has, to my knowledge, not been described previously. As shown by Figure 5.11, the transformation process involves the progressive conversion of the original vaterite framboid into a single calcite crystal. The latter transformation pathway seems to be initiated from within "loosely" packed vaterite aggregates. (Figure 5.13), while calcite growth mode (a) is observed for "densely" packed aggregates (Note: the two types of aggregates are compared in Figure 4.9 and 4.10). As discussed in Chapter 4, it is difficult to synthesize vaterite aggregates of uniform morphology. Thus, variable mixtures of growth modes (a) and (b) can be expected in the transformation experiment.

Different transformation pathways may explain why experimental conditions, such as the solid-to solution ratio or stirring of the suspension, may differently affect the transformation kinetics. For example, the transformation time of S3 seems to depend on stirring rate, while this is not the case for S14 (Table 5.3.). Thus, differences in the structure and packing of the original vaterite aggregates may have a large impact on the rate of transformation into calcite.

5.4.2 Rate Controlling Processes

Three processes are involved in the solution-mediated crystal transformation: (1) dissolution of vaterite, (2) transport of ions through solution (diffusion), and (3) calcite growth (for details on these processes, see section 2.3.3). Which of these processes is rate limiting is still controversial. Some authors state that the dissolution of vaterite is the rate limiting process (Han et al., 2006; Kitamura, 2001; Spanos and Koutsoukos, 1998), whereas others identify calcite growth as the rate limiting process (Kralj et al., 1997; Ogino et al., 1987). To shed light on the question which of these processes controls transformation kinetics, the three possible processes will be discussed using the data obtained in this study.

5.4.2.1 Vaterite Dissolution

The solution composition monitored during the transformation of vaterite to calcite exhibits several characteristics that give insight into the underlying processes. First, upon addition of vaterite to the beaker, pH and $[Ca^{2+}]$ increase instantaneously (within 3 minutes) to a pH of 10.1 and ~0.25 mM. Even though the aqueous system is

not closed (the 200 ml solution is in contact with a 130 ml headspace over an 50 cm^2 exchange area, and the headspace is connected to the atmosphere via holes designed for electrode insertion), rapid vaterite dissolution causes the solution to reach closed-system equilibrium with vaterite (pH = 10.11, [Ca^{2+}] = 0.38 mM, Visual Minteq). The difference in the measured Ca^{2+} concentration and the calculated equilibrium value is most likely due to the delayed initial response of the ion-sensitive electrode. After a period of steady decrease in pH (approx. 16 hrs in Figure 5.5), a distinct drop in pH, coinciding with a decrease in Ca^{2+}, is observed. Subsequently, Ca^{2+} increases again and the system moves towards pH and Ca levels that correspond to a system in equilibrium with atmospheric pCO$_2$ and with calcite (pH ~ 8.3, [Ca^{2+}] ~ 0.7 mM).

In a closed system, where vaterite dissolution is fast and thus not rate limiting, one would expect a constant pH of 10.1. The solution would stay close to saturation for vaterite, and because of the identical stoichiometry of calcite and vaterite, all precipitating ions would be delivered from vaterite dissolution. Hence, the dissolved Ca^{2+} concentration would be constant as well until all vaterite is dissolved. At that point, the continued precipitation of calcite would draw down the aqueous concentration of Ca^{2+} and CO$_3{}^{2-}$, until $\Omega_{calcite}$ = 1 is reached. The observed trends in solution composition deviate from those predicted for a close system, because of the exchange of CO$_2$ between the aqueous and gas phases in the experimental set-up.

To simulate the process of vaterite dissolution, calcite precipitation and exchange of CO$_2$ with the gas phase, a model was implemented, encompassing kinetic expressions of the above 3 processes, as well as chemical speciation in the aqueous phase. Starting from equilibrium with vaterite, and assuming a constant atmospheric pCO$_2$ in the headspace, the solution is speciated in each time-step, given the total masses of C, H and Ca in solution, and a background electrolyte of 0.1M KCl. Speciation is based on mass action (equilibration between species) and mass balance (conservation of mass) equations, and can formally be described in terms of linearly independent chemical components (see Morel and Hering, 1993 for details):

$$a_j = K_j \prod_i^n a_i^{v_{ji}} \, , \qquad\qquad (5.2)$$

where v is the stoichiometric coefficient (positive for products, negative for reactants), a the activity, K the thermodynamic equilibrium constant, n is the number of components and the subscripts i and j identify the components and species, respectively. Mass conservation is established by expressing the (known) total mass of component (T_i) in terms of the concentrations of the species:

$$Y_i \equiv T_i - \sum_j^m v_{ji}[S_j] = 0 , \tag{5.3}$$

where m is the number of species and [S] the species concentration. Concentrations and activities are related via $a = \gamma[S]$, where there activity coefficient γ is calculated using the Davies equation (Langmuir, 1997). The aqueous species distribution is solved iteratively as a root-finding problem using a Newton-Raphson algorithm. Details on the implementation and derivation of the Jacobian matrix are given in Tadanier and Eick (2002).

Kinetic transport and reactions are implemented as follows. Diffusive exchange of CO_2 between solution and headspace depends on the concentration difference between solution and headspace across a diffusive exchange length (Morel and Hering, 1993):

$$R_{diff} = \frac{A_{ex}D_c}{V_{sol}dz}\left(CO_2^{atm} - CO_2^f\right) \tag{5.4}$$

where A_{ex} is the solution-gas exchange area, V_{sol} the solution volume, D_c the diffusion coefficient, dz the diffusive boundary layer thickness, CO_2^{atm} and CO_2^f the CO_2 concentrations in the gas and the fluid phase, approximated as (pCO_2/Henry constant), and ($0.997*H_2CO_3^*$), respectively (Zeebe and Wolf-Gladrow, 2001). Precipitation of calcite is represented by the rate law:

$$R_{prec} = k_{prec}\left(\frac{a_{Ca^{2+}}a_{CO_3^{2-}}}{K_{sp}^{calcite}} - 1\right)H_{prec} \tag{5.5}$$

where k_{prec} is a rate constant, K_{sp} denotes the solubility of calcite, and H_{prec} is 0 if the solution is undersaturated with respect to calcite, else 1. Dissolution is allowed for both vaterite and calcite, depending on the saturation state.

$$R_{diss}^{i} = k_{diss}^{i} \left(1 - \frac{a_{Ca^{2+}} a_{CO_3^{2-}}}{K_{sp}^{i}} \right) H_{diss}^{i} \tag{5.6}$$

with distinct dissolution and solubility constants for calcite and vaterite, indicated by superscript i. H_{diss} is 1 except if the solution is oversaturated, or if the solid is not present. Combined, these rates give rise to the following conservation equations:

$$\frac{dDIC}{dt} = R_{diff} + R_{diss}^{vaterite} + R_{diss}^{calcite} - R_{prec}$$

$$\frac{dH_T}{dt} = 2R_{diff} \tag{5.7}$$

$$\frac{dCa_T}{dt} = R_{diss}^{vaterite} + R_{diss}^{calcite} - R_{prec}$$

where DIC is dissolved inorganic carbon, H_T total dissolved hydrogen concentration and Ca_T total dissolved calcium concentration in the system. Note that H_T is affected by the phase exchange of the acid CO_2.

Poorly known parameters include the diffusive boundary thickness, and the reaction rate constants. The vaterite precipitation rate is adjusted to allow all vaterite to dissolve by the time the pH drop occurs (the inflection point in Figure 5.5). dz is estimated to be on the order of ≥40 μm (Morel and Hering, 1993), and set to 120 μm. For calcite, precipitation and dissolution near saturation is assumed to proceed at equal rates with respect to Ω, i.e. k_{prec}(calcite) = k_{diss}(calcite). Due to its more crystalline nature, the rate constant of calcite is arbitrarily set to 1/10 of the rate constant for vaterite. This parameterization results in a close reproduction of the measurements with the model. Thus the combination of these 3 processes seems to adequately explain the observed temporal solution compositional dynamics (Figure 5.14). In particular, model simulations give rise to near-saturation for vaterite (not shown), whose dissolution is driven by the removal of Ca and CO_3 via calcite

precipitation. Gas exchange then is a major cause for the tailing off towards the end of the experiment.
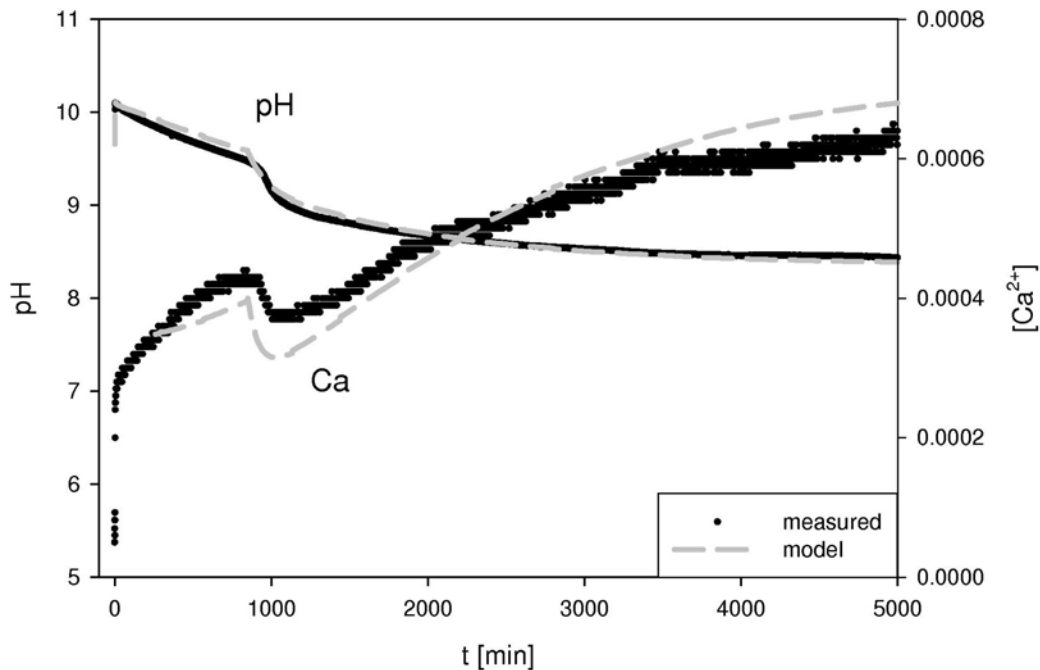
Figure 5.14: Measured (black dots) versus calculated (gray dashed) [Ca^{2+}] (M) and pH development during vaterite to calcite transformation.

In summary, model calculations imply near saturation conditions with respect to vaterite before the inflection point is reached. This, together with the observation that at the inflection point almost no vaterite is left (Figure 5.10), clearly indicate that the dissolution of vaterite is not rate limiting for the transformation into calcite.

5.4.2.2 Transport Limitations

The vaterite to calcite transformation within a vaterite aggregate itself (Figure 5.13), and the transformation outside the aggregate (Figure 5.18 and 5.19), represent the two possible end-member scenarios of the transformation process. Transformation inside a relatively loosely packed aggregate, such as observed in Fig. 5.13 and characterized by diffusion distances on the order of a few nm, represents a situation in which diffusion is not regarded as a rate limiting process. If, on the other hand, the transformation occurs outside the aggregate, diffusion limitation can not be excluded a priori, if the dissolving and precipitating particles are spatially separated

over larger distances (several µm). To assess the potential for such transport limitation, diffusive exchange rates between evenly distributed vaterite and calcite particles are estimated. Lasaga (1998) has presented a simple model for the transformation of one mineral phase into another (Figure 2.10). Assuming that the chemical composition near the mineral surfaces approach their respective solubilities, the rate J at steady state matches the diffusion exchange and can be calculated by:

$$J = \frac{D}{L_r}(C_{eq}^B - C_{eq}^A)A_d$$

(5.8)

where C_{eq}^A and C_{eq}^B are the equilibrium concentrations of the minerals, D is the diffusion coefficient in the solution, A_d the exchange area and L_r the diffusion length (see also Section 2.4). The latter is the characteristic length scale above which – at a given rate transformation rate J and exchange area – diffusion is limiting.

The length scale estimate derived from Equation 5.8 can be compared to the length scale associated with the experimental condition. As the solids were kept in suspension, an order of magnitude estimate of the characteristic distance between the particles is given by

$$L_d = \sqrt[3]{\frac{V}{n}}$$

(5.9)

where V is the volume of the solution and n the number of calcite crystals in the experiment. The number of particles is estimated from analysis of SEM images (for details, see Section 4.2.2), which show average sizes of calcite crystallites at the end of the experiment on the order of 5 to 20 µm. Assuming cubic geometry, n is then obtained for a given solid density (2.7g cm^{-3}) and the known total solid mass in the system.

Image analysis also indicates that, due to the much smaller particle size, vaterite surface area exceeds that for calcite even at vaterite to calcite mass ratios as low as 1:1000, i.e. nearly throughout the entire transformation process. Hence, the exchange area A_d is approximated by the calcite surface area. To estimate A_d in a

system where the calcite surface area increases with time, two end-member scenarios were considered. (1) The calcite crystals precipitate simultaneously during the transformation process. In that case, the number of particles stays constant during growth. (2) One crystal growth after the other. In the latter case the number of crystals would increase with time. Figure 5.15 shows the temporal evolution of the two surface area estimates during growth to a known final crystal size. As the difference between these two end-member scenarios are small compared to the above simplifying assumptions, only the constant *n*–scenario is considered below.
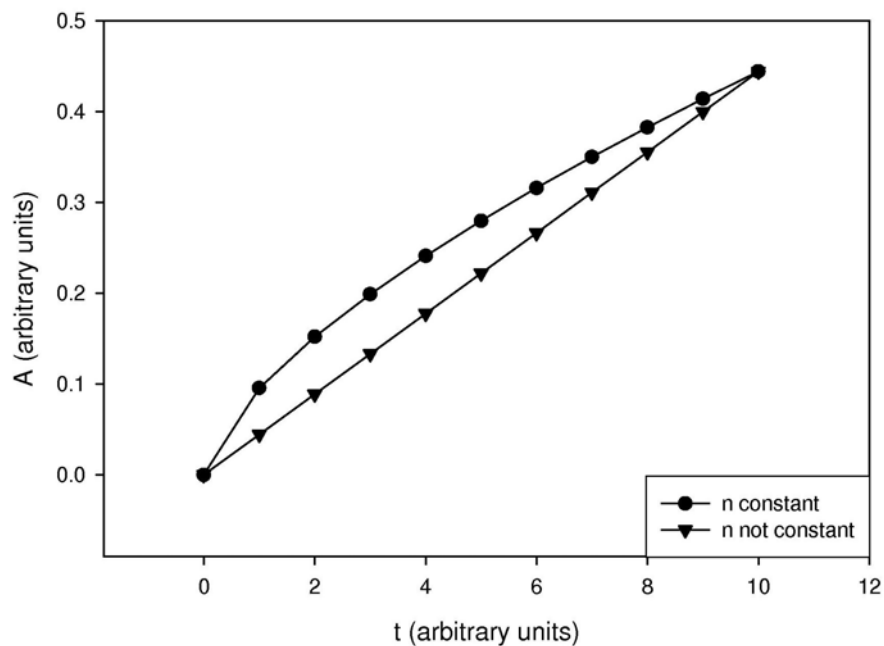
Figure 5.15: Development of surface area during the growth of calcite crystals (treated as cubes). In the case of "n constant", a constant amount of cubes growth simultaneously. In scenario "n not constant", the cubes grow to a specified diameter (5 μm) before the next cube starts to grow.

The expressions for the above two length scales, L_d and L_r, can be combined to assess whether diffusion limitation is a possibility in our settings. If the distribution scale, (L_d), is smaller than the diffusion length ,L_r, needed to sustain the measured transformation rates, then diffusion is likely not limiting. Formally, diffusion limitation is expected at $L_r/L_d < 1$. Combining Equations 5.8 and 5.9 and reformulating in terms of the experimentally known quantities, one obtains:

$$L_r/L_d = n^{4/3} \cdot D \cdot (C_{eq,vaterite} - C_{eq,calcite}) \cdot 6 \cdot L_{crystal}^2 \cdot \mathrm{MW}/(R \cdot V_{tot}^{1/3} \cdot g_{tot}) \qquad (5.10)$$

where $L_{crystal}$ is the size of the crystal, D the diffusion coefficient, C_{eq} the concentration in equilibrium with a mineral phase, MW molecular weight of $CaCO_3$, R the transformation rate in g_{CaCO3} precipitating per g total solid in the system (g_{tot}) and time, V_{tot} the suspension volume, and n is the number of crystals (g_{tot} / ρ_{CaCO3} / $L^3_{final\ crystal}$). C_{eq} is estimated as the concentration in equilibrium with the (infinite) solid calcite and vaterite, respectively, in a closed system. In our setting, concentration differences for Ca^{2+} and CO_3^{2-} are comparable (0.16 vs. 0.12 mM) and an arbitrary choice of Ca^{2+} does not affect the general findings. $L_{crystal}$ varies over the course of the experiment, and it is assumed that an initial mass of 5% calcite is equally distributed over the n crystals.
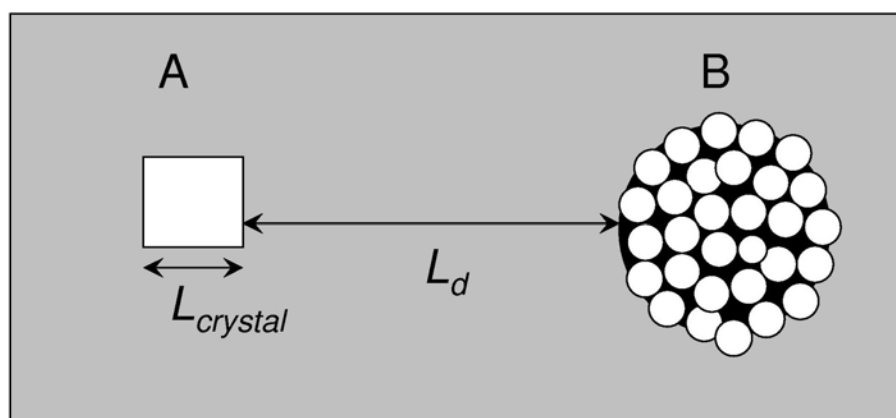
Figure 5.16: Schematic diagram illustrating the situation in which the dissolving (B) and precipitating (A) particle are spatially separated, over the distance L_d. $L_{crystal}$ is the diameter of the crystal, which increases during growth, leading consequently to an increase in calcite surface area A_d. In this scenario, it is assumed that no transformation inside the aggregate (black area) occurs.

A rough estimate of the geometrical arrangement (Figure 5.16) present in our experiments indicates that within the range of measured reaction rates, observed crystal sizes and solid to solution ratios, diffusion limitation occurs at a low solid to solution ratio (Figure 5.17). At a given rate and solid mass in the system, the final crystal size determines the number of crystals. The larger their number, the closer on average sources (vaterite) and sinks (calcite) are spaced, a situation able to support high diffusion fluxes (compare (a, c) in Fig. 5.17). Similarly, at a given rate expressed as g precipitate per gram total solid and time (and not per area), an increasing solid to solution ratio leads to a decrease in average distance between vaterite and calcite, loosening constraints set by diffusional exchange (compare (a, b) in Fig 5.17).
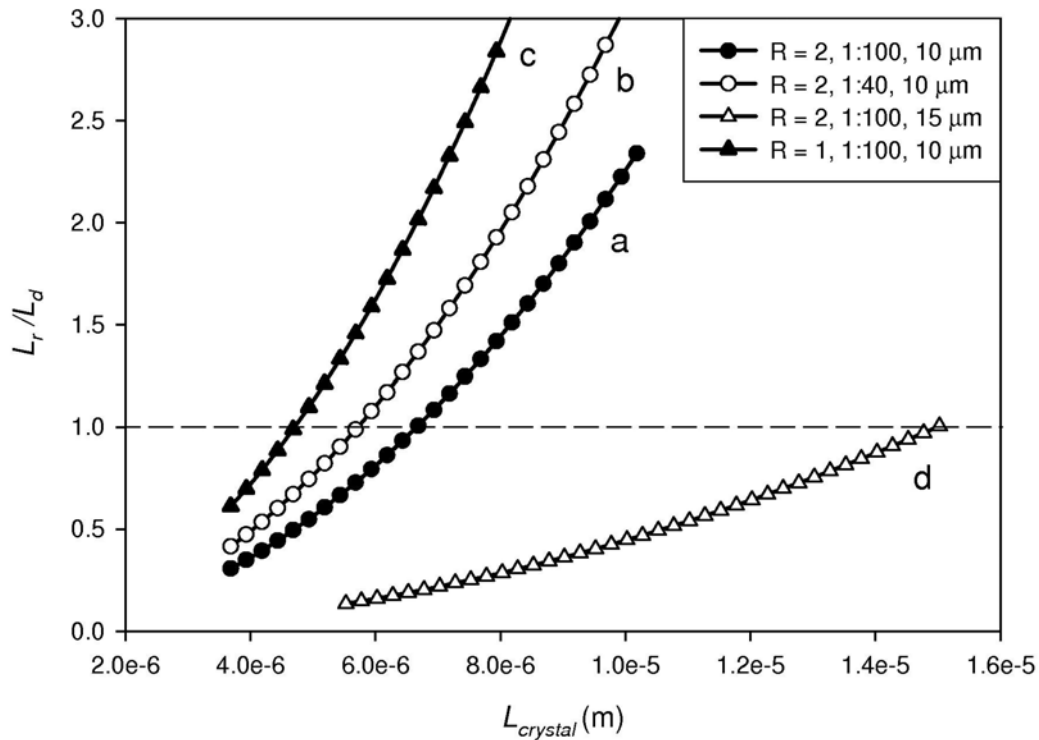
Figure 5.17: Potential for diffusion limitation as a function of crystal size and transformation rate. A value of $L_r/L_d < 1$ indicates possible diffusion limited growth (R is given in 10^{-5} g g^{-1} s^{-1}).

This analysis shows that under the experimental conditions, in particular at low solid to solution ratios, diffusion can become rate limiting, if the transformation is not occurring predominantly inside the aggregate itself.

The available data do not allow unambiguous identification of growth location. Visual analysis of individual particles suggest transformation within aggregates (Figure 5.13) in some cases, while others (Figure 5.19) may be indicative of separate locations of vaterite dissolution and calcite growth. This ambivalence is also supported by the observed effect of stirring: Experiments vatdis01 – 05 (Table 5.3) show increased rates under stirred conditions, presumably due to reduced diffusion distances, while in experiments vatdis08 - 11 (Tabble 5.3) no effect was observed. Overall, the evidence suggests that for densely packed vaterite aggregates, transport limitation may play an important role in the transformation process.

5.4.2.3 Calcite Growth

The discussion on the rate limiting processes of vaterite to calcite transformation so far has been restricted to the range between ~10 wt. % (the initial amount of calcite present in the solids) and ~60 wt. % of calcite formed. It does not

apply to the very onset of transformation, which requires the nucleation of calcite. Concerning the final phase of transformation (≥ 60 wt. % calcite), it is most likely not rate-limited by vaterite dissolution until the very last moment.

Only when nearly all vaterite is gone, the solution composition remains close to equilibrium with respect to vaterite (Section 5.4.3.1). Until ~60 wt. % of calcite, the transformation rate is constant (Figure 5.4). The calcite supersaturation of a solution saturated with respect to vaterite is ~3.7. At this relatively low supersaturation, spiral growth is normally expected (Christoffersen and Christoffersen, 1990) for large calcite crystals. The transformation occurring within the aggregate (Figures 5.11 – 5.13) is characterized by the presence of many small calcite crystallites exhibiting rough surfaces with many kink- and step-sites (see *Chapter 2)*. This may explain the high growth rates of calcite even at a relative low supersaturation. With progressive transformation of the calcite into larger crystals their surfaces smoothen (Figure 5.11 b, d). Therewith the decrease in transformation rate after ~60 wt. % of calcite may reflect a switch in growth mechanism probably caused by a change in growth mechanism, accompanying the "flattening" of the calcite surfaces. However, calcite growth has to be a potential rate controlling process in the experiments presented, since vaterite dissolution can be excluded (Section 5.4.2.1) and diffusion limitation is only possible in experiments characterized by very low solid to solution ratios (Section 5.4.2.2).

5.5. Conclusion

This study details the transformation of vaterite into calcite. The process is documented by monitoring changes in solution composition and solid phase morphology. XRD analysis shows a continuous disappearance of vaterite, while two distinct growth modes for calcite are observed using SEM. Here we document for the first time that the transformation of loosely packed framboidal vaterite aggregates starts "inside" the aggregate itself. With ongoing transformation a more solid morphology develops, resulting in the typical romboheral calcite crystals. Our findings

highlight the importance of combining morphological observations with techniques that measure macroscopic phase changes.

Because of the large surface area to volume ratios of the initial vaterite, the transformation process is not rate-limited by the dissolution of vaterite. This is consistent with the transformation rates derived from XRD analysis between ~10 to ~60 calcite wt. %, and with model simulations with respect to the dissolving crystal, which indicate rapid vaterite dissolution and near-saturation conditions of the solution composition. The observation that, at least in some of the experiments, stirring causes changes in the transformation rate implies that diffusion limitation plays a role during vaterite to calcite transformation. This is supported by order-of-magnitude calculations, which show that diffusion becomes rate limiting at low solid to solution ratios.

When the transformation reaches ~60 wt. % of calcite, the transformation rate starts to decrease, because of annealing of the calcite crystallites into larger single crystals. This annealing causes a decrease of the calcite surface area, and, possibly, a change in growth mechanism due to the decreasing surface roughness. This may causes calcite growth to become rate limiting.

5.6 Appendix
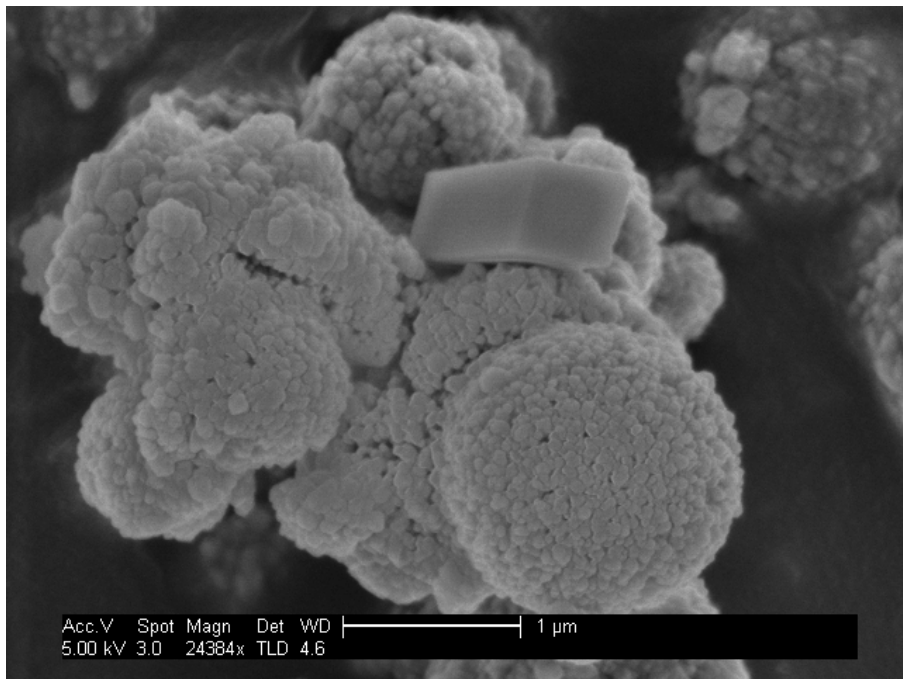
Figure 5.18: _vatdis08_; SEM image taken 200 min (sp1 in Figure 5.10) after the solid S3 was added to the solution.
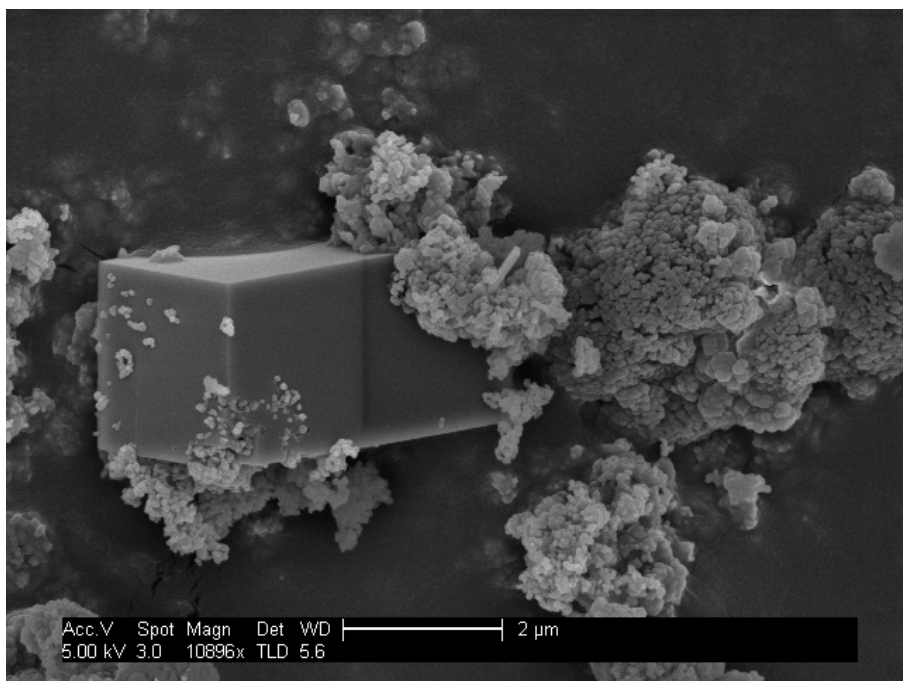
Figure 5.19: _vatdis08_; SEM picture taken 500 min after the solid S3 was added to the solution (sp2 in Figure 5.10).
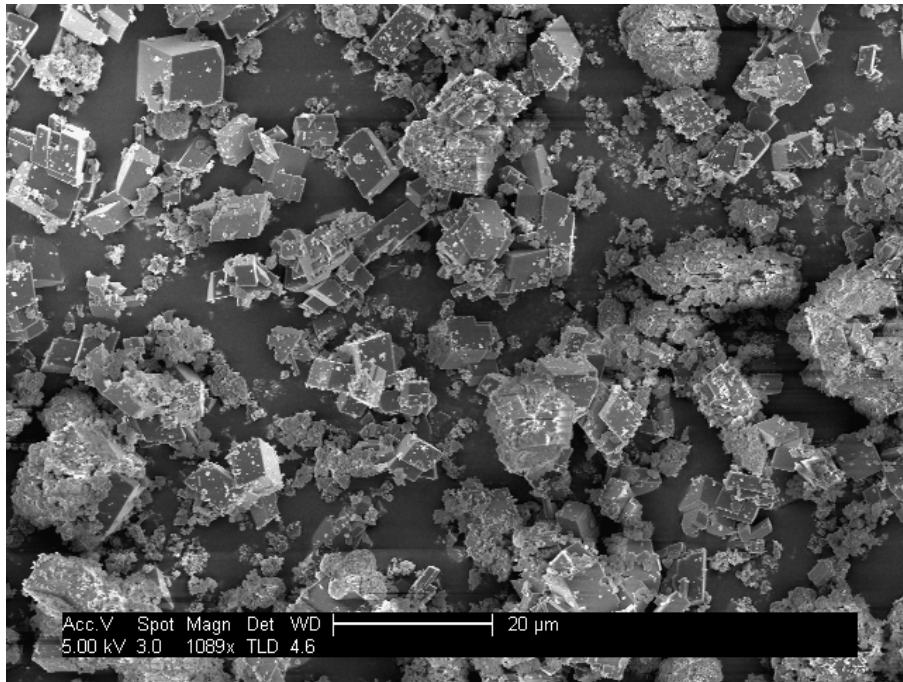
Figure 5.20: _vatdis08_; SEM picture taken 800 min after the solid S3 was added to the solution (sp3 in Figure 5.10).
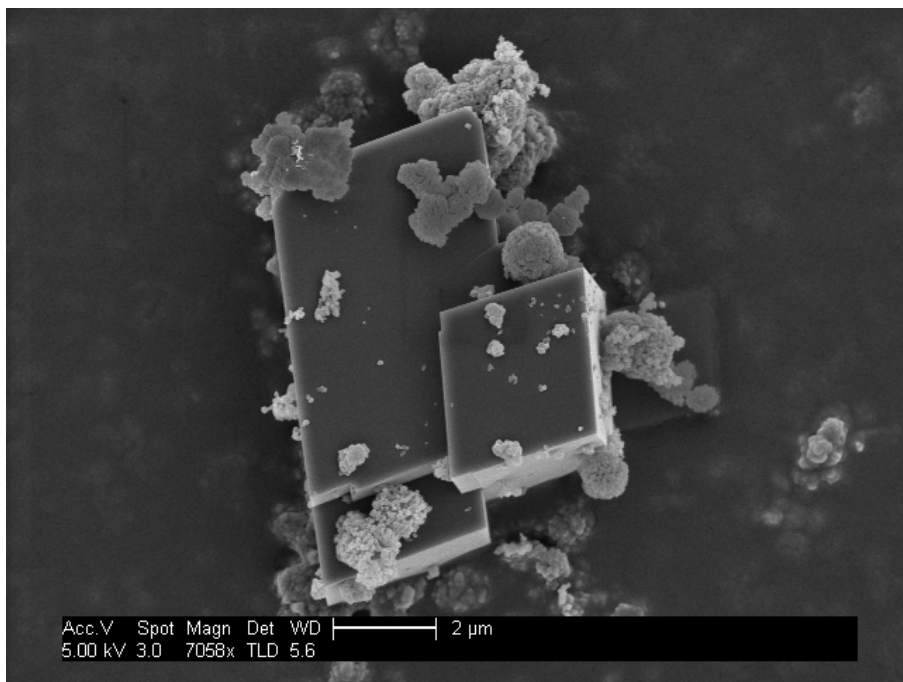
Figure 5.21: _vatdis08_; SEM picture taken showing a detailed view of the particles shown in Figure 5.20.
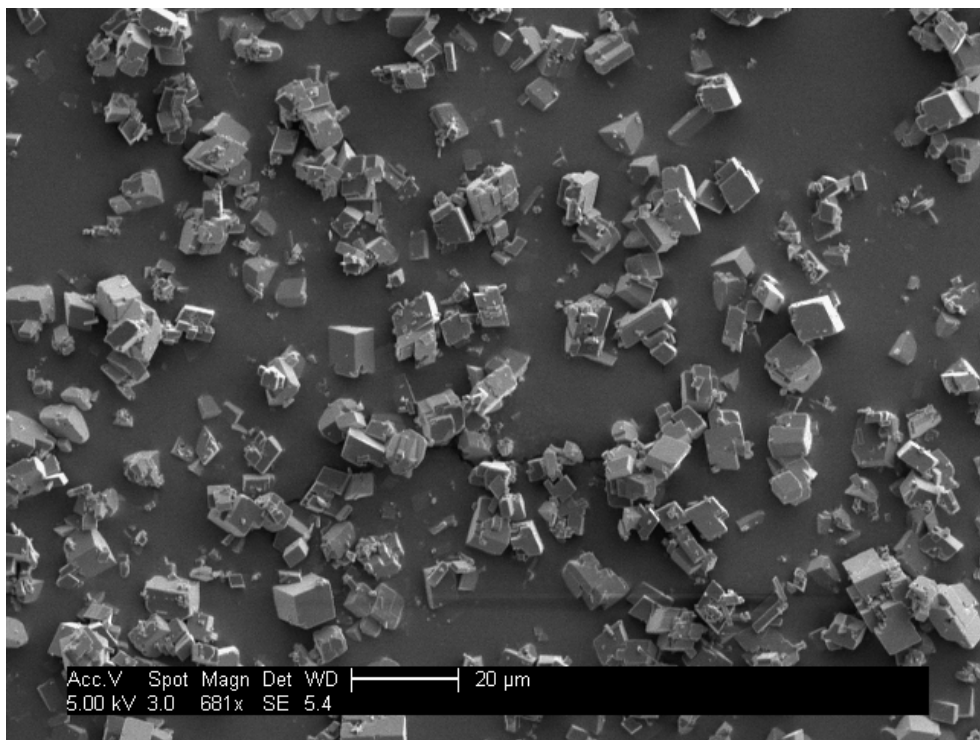
Figure 5.22: _vatdis08_; SEM picture taken ~2000 min after the solid S3 was added to the solution (sp4 in Figure 5.10).

6 Dependence of Calcite Growth Rate and Sr Partitioning on Solution Stoichiometry: Non-Kossel Crystal Growth

6.1 Introduction

Calcite is one of the most abundant and reactive minerals at the Earth's surface. It is a major component of the global carbon budget (Morse and Mackenzie, 1990), and it affects the fate of many organic and inorganic constituents in the environment through sorption processes (Langmuir, 1997). Furthermore, calcite is an important industrial material, although its formation may represent a nuisance in industrial processes (scale formation). Many studies have been devoted to the effects of physico-chemical parameters, such as temperature, pressure, pH, ionic strength and supersaturation, on the precipitation of calcite from aqueous solution, as well as on trace element partitioning and isotope fractionation during calcite formation (Lemarchand et al., 2004; Rimstidt et al., 1998).

Divalent metal ions of similar ionic radius as Ca^{2+} may be incorporated as impurities into calcite during mineral precipitation. The concentrations of trace metals, e.g., Mg, Sr or Ba, in biogenic calcite are used as palaeo-proxies for the reconstruction of past environmental conditions (e.g. Boyle, 1981; Boyle, 1988; Lea and Boyle, 1989), while sorption to calcite may represent an important pathway for the immobilization of hazardous metals, e.g., Cd and radionuclides (Curti, 1997). A variety of studies have shown that the growth rate influences the removal of aqueous trace metals by calcite (Rimstidt et al., 1998).

Kinetic descriptions of calcite growth based on classical crystal growth theory relate the rate of calcite precipitation to the degree of supersaturation, $\Omega = IAP/K$, where K is the solubility product of calcite, and IAP = $\{Ca^{2+}\}\{CO_3^{2-}\}$ the ion activity

product in the solution (Nielsen, 1964; Nancollas and Reddy, 1971; Nielsen, 1984; Nielsen and Toft, 1984; Teng et al., 2000; many others). Besides Ω, the aqueous composition may also affect the growth rate of carbonate minerals via the solution stoichiometry (Zuddas and Mucci, 1994; Sternbeck, 1997). However, in published studies, the degree of supersaturation with respect to calcite and the concentration ratio of dissolved Ca^{2+} to CO_3^{2-} ions generally vary together (Christoffersen and Christoffersen, 1990; Lemarchand et al., 2004; Lorens, 1981; Tesoriero and Pankow, 1996; van der Weijden et al., 1997). This hinders a separate evaluation of the effects of the solution stoichiometry and ion activity product on calcite growth kinetics.

In this study, growth rates of single calcite crystals were measured as a function of solution stoichiometry, at fixed pH and fixed degree of supersaturation. To create Ca^{2+} to CO_3^{2-} concentration ratios both larger and smaller than one, the experiments were conducted at fairly high pH (10.2). Furthermore, the incorporation of trace amounts of Sr during calcite precipitation was monitored, in order to determine how the solution to solid partitioning of this cation depends on the growth kinetics and Ca/CO_3 solution composition. Strontium was selected because of the high solubility of $SrCO_3$, and because the ionic radius of Sr^{2+} is close to that of Ca^{2+}, therefore minimizing the effects of the trace metal cation on the growth rate of calcite.

6.2 Theoretical Background

6.2.1 Crystal Growth Kinetics and Solution Stoichiometry

Kossel (1927) and Stranski (1928) developed a crystal growth model wherein a growth unit (GU) can attach to six distinct surface sites (Figure 2.3). These sites differ in their potential energy with respect to attachment of a GU. Because the attachment to a kink site (KiS) does not alter the number of bonds available at the mineral surface, it represents the energetically most favourable site for the incorporation of GU into the crystal lattice. Hence, a possible mechanism for growth of a crystal from a liquid or vapor phase involves the following succession of steps: (i) adsorption of a GU onto the crystal surface, (ii) diffusion to a step, and (iii) incorporation into a kink site (Figure 2.3).

Depending on the degree of supersaturation, Ω, different growth modes may dominate, e.g., layer growth, spiral growth, two-dimensional nucleation, which itself can be subdivided in different modes, e.g. layer-by-layer and multilayer (Markov, 2003). All these modes have in common that the growth rate can be described in terms of the attachment and detachment frequencies of GUs to and from all possible surface sites. The resulting rate equations are typically simplified and only account for lattice site(s) that dominate growth, in general the kink sites (KiS, Figure 2.3).

In the original model of Kossel and Stranski, the so-called Kossel crystal consists of a cubic lattice composed of a single chemical species, the GU (Zhang and Nancollas, 1990). Strictly speaking, the model of Kossel and Stranski applies to elemental or molecular crystals, and Ω is equal to the ratio of the activity of the GU in the fluid phase and the corresponding equilibrium value. For the precipitation from aqueous solution of a mineral such as calcite, crystal growth involves the alternating incorporation into the lattice of cations and anions (Figure 6.1). In this case, the growth rate also depends on the relative abundances of the cations and anions in solution, in addition to Ω. Several researchers have extended the original Kossel crystal growth model to describe the precipitation of multicomponent non-Kossel crystals from aqueous solution (Chernov, 2001; Chernov et al., 2006; Zhang and Nancollas, 1998).
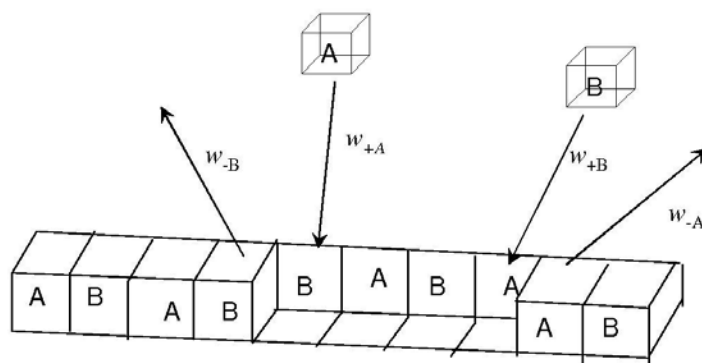
Figure 6.1: When growth requires incorporation of alternative ions, A and B, the attachment (w_+) and detachment (w_-) frequencies of both ions, influences the growth rate.

One of the few studies in which the predictions of non-Kossel crystal growth theory are directly compared to experimental data is that of Chernov et al. (2006). These authors measured the effect of solution stoichiometry on the step propagation

velocities of $CaC_2O_4 \cdot H_2O$ and $MgC_2O_4 \cdot 2H_2O$ by means of atomic force microscopy (AFM). They observed that, at constant degree of supersaturation, the step rates measured on various crystal faces reached their maximum values when the concentration ratio of cation to anion in solution, r, equalled one. Furthermore, the rates decreased symmetrically away from $r = 1$, that is, $v_k(r) = v_k(1/r)$. Both observations are in agreement with non-Kossel crystal growth theory, if the frequency factors describing attachment of the cation and anion are the same. As remarked by Chernov and co-workers, "this symmetry exists in spite of fact that the Ca^{2+} and Mg^{2+} ions on the one hand and the $C_2O_4^{2-}$ on the other have different size, shape and spatial symmetry".

6.2.2 Trace Element Partitioning

The distribution of a trace metal, for example Sr, between calcite and the aqueous phase from which the mineral forms can be described by a partition coefficient D_{Tr}, defined as,

$$D_{Tr} = \frac{[Tr]_s / [Tr]_l}{[M]_s / [M]_l}$$

(6.1)

where [Tr] and [M] are the molar concentrations of the trace (strontium) and major (calcium) element in the solid (s) and liquid (l) phase, respectively. The partition coefficient represents a phenomenological coefficient (Morse and Bender, 1990), and is distinct from the thermodynamic distribution constant, $K_{D_{Tr}}$. The latter is defined in terms of the activity coefficients of the trace and major ions in both phases at thermodynamic equilibrium (McIntire, 1963).

Rimstidt et al. (1998) have estimated the values of $K_{D_{Tr}}$ for incorporation into calcite of many elements by fitting a large dataset from the literature. Their work, and many other experimental investigations (Kitano et al., 1971; Kitano and Oomori, 1971; Lorens, 1981; Mucci, 1986; Mucci and Morse, 1983; Pingitore and Eastman, 1984; Temmam et al., 2000; Tesoriero and Pankow, 1996) have shown that the difference between the thermodynamic distribution constant, $K_{D_{Tr}}$, and the empirical

partition coefficient, D_{Tr}, reflects kinetic effects, in particular the growth rate of the host crystal. For trace elements with $K_{D_{Tr}} > 1$, measured D_{Tr} values are generally lower than the equilibrium value, and vice versa for $K_{D_{Tr}} < 1$. When the growth rate tends to zero ("growth at equilibrium"), D_{Tr} approaches $K_{D_{Tr}}$.

6.3 Materials and Method

Growth rates were determined on calcite single crystals of known mass, each placed in a separate flow-through reactor. The solutions flown through the reactors were characterized by two different supersaturations and variable $[Ca^{2+}]$ to $[CO_3^{2-}]$ ratios, but constant pH. At the end of an experiment, each crystal was weighted to determine the mass of calcite grown during the experiment. Measurement of Sr incorporation was carried out by laser ablation inductively coupled plasma mass spectrometry (LA-ICP-MS).

6.3.1 Crystal Growth Experiments

6.3.1.1 Seed Material

Calcite seed crystals were produced from an Iceland spar. The latter had a size of approximately 5 cm x 5 cm x 2 cm. It was cleaved manually using a small flat chisel to produce crystals of approximately 1–1.5 mm^3 (Figure 6.2A). Crystals showing little damage (as shown in Figure 6.2A) were handpicked under a binocular and cleaned in an ultrasonic bath to remove loose particles. The soaking solution was a calcite-saturated aqueous solution prepared from reverse osmosis water (conductivity < 0.067 µS) and Suprapure® (Merck®) calcite powder. The crystals were then stored for 2 months in the saturated Suprapure® calcite solution, to provide equilibrated surfaces for growth. Prior to the experiments, the crystals were washed with ethanol to avoid precipitation from water droplets during drying. The crystals were then dried in an oven at 40°C for 1 hour, weighted on a Mettler Toledo® UMX2

micro-balance, with a resolution of 0.1 µg, and transferred into the flow-through reactors. Each reactor contained a single crystal.
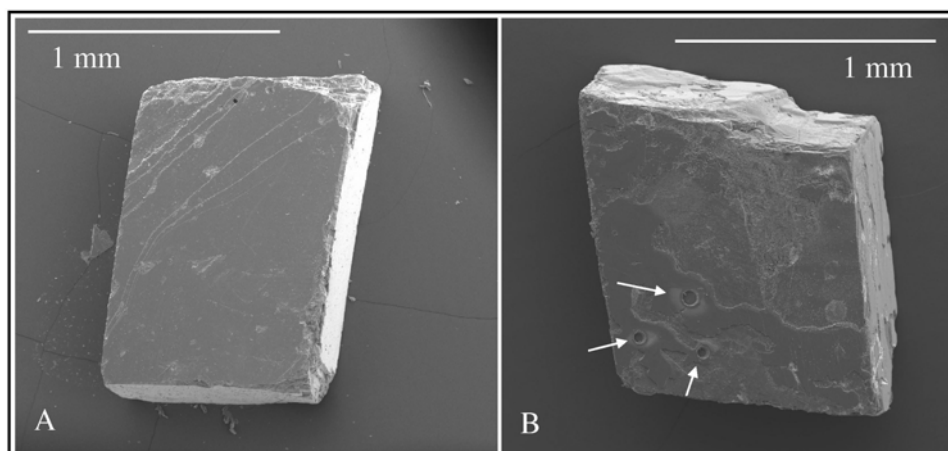
Figure 6.2: Scanning electron micrograph A shows a typical calcite crystal used as seed material in the flow-through reactor experiments. Micrograph B shows a calcite seed with an overgrowth collected at the end of a precipitation experiment. In the lower left corner three ablation holes are visible, produced during the LA-ICP-MS analysis (arrows).

6.3.1.2 Crystal Growth Experiments

Reactors with an inner diameter of 5 mm and a depth of 15 mm were built out of Teflon® (Figure 6.3). The reactor inlet was connected to a 50 mm long Tygon® tubing (I.D. = 1.6 mm, O.D. = 4.8 mm), which collected solutions coming from two separate reservoirs via a Y-connector. One solution contained the Ca^{2+} ions, the other the CO_3^{2-} ions. Tedlar® bags where used as solution reservoirs, to avoid the formation of a headspace while the solutions were pumped out of the bags. Flow was adjusted to 10 µl min^{-1} with a 16 channel Watson Marlow® (S205) peristaltic pump, and found to remain constant from the measurement of outflow volumes. Tubing wall thickness and bag material were chosen to minimize gas exchange with the atmosphere (Tedlar® bags were originally designed for gas sampling). For each reactor inflow solution composition, four replicates were run by connecting 4 reactors to one set of bags. All experiments were performed in a thermostated laboratory at 20°C.
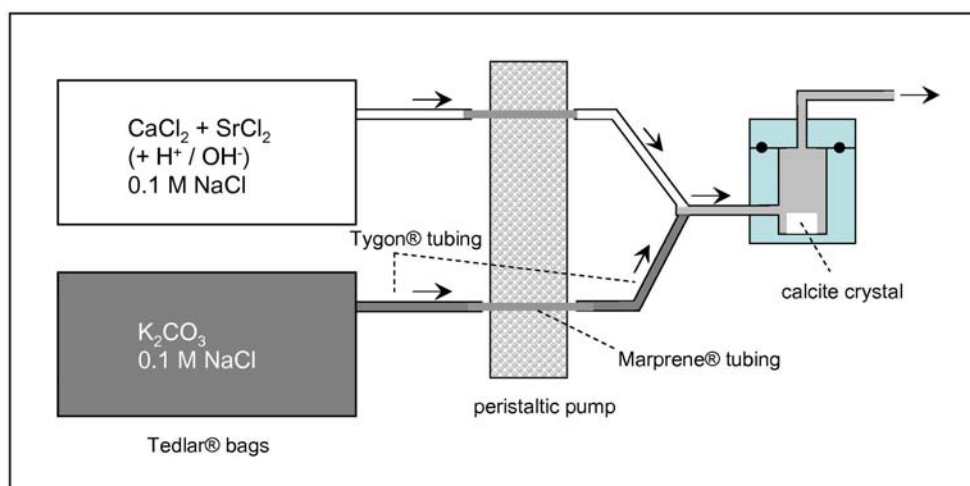
Figure 6.3: Experimental setup. Flow was maintained by a peristaltic pump, and Ca^{2+} and CO_3^{2-} solutions in Tedlar® bags were mixed prior to entering the flow-through reactor. The latter contains a single calcite seed crystal.

The Ca^{2+} and CO_3^{2-} solutions were prepared by dissolving Merck® Suprapure® $CaCl_2 \cdot 4H_2O$ and K_2CO_3 in filtered (0.2 µm pore size) reverse osmosis water (conductivity < 0.067 µS), with 0.1 M NaCl as background electrolyte. Strontium was added to the Ca^{2+} solution as $SrCl_2$. The Ca:Sr ratios were on the order of 100:1. The equilibrium chemical speciation of the inflow solution obtained after mixing of the Ca^{2+} and CO_3^{2-} solutions was calculated using Visual Minteq V. 2.40 (Gustafsson, 2004). The calculations showed that all inflow solutions, except one (reac001), were undersaturated with respect to $SrCO_3$.

A pH of around 10 was selected for the inflow solutions. At this pH, CO_3^{2-} is a major dissolved carbon species, which facilitated the preparation of stoichiometric $[Ca^{2+}]$ to $[CO_3^{2-}]$ ratios ranging from less than one to greater than one, while maintaining constant ionic strength. In addition, to produce a pH around 10, only small additions of acid to the Ca^{2+} solution were required, thereby avoiding corrosion of the stainless steel Y connector used for mixing the Ca^{2+} and CO_3^{2-} solutions. Table 1 lists the compositions of the 12 different reactor inflow solutions. Based on the measured calcite growth rates, less than 1% of the Ca^{2+} and CO_3^{2-} ions supplied via the inflow precipitated in the reactors. Therefore, the solution composition inside the reactor was assumed to be equal to that of the inflow solution.

Table 6.1: Inflow solution compositions for the precipitation experiments using the flow-through reactors. The table lists the measured (ICP-OES) total concentrations of Ca and Sr, as well as the (free) ion concentrations, $[Ca^{2+}]$ and $[CO_3^{2-}]$, calculated using Visual Minteq. Also given are the reciprocals of the stoichiometric solution ratios, $1/r$, and the degrees of supersaturation with respect to calcite, Ω..

Experiment	[Ca] mmol L^{-1} (ICP-OES)	[Sr] µmol L^{-1} (ICP-OES)	pH (mean)	$[CO_3^{2-}]$ mmol L^{-1} (calc.)	$[Ca^{2+}]$ mmol L^{-1} (calc.)	$1/r$ (calc.)	Ω (calc.)
reac004n	15.6±0.4	n.d.	10.2±0.1	0.037	14.180	0.003	19
reac005	1.77±0.06	21.8.+0.1	10.2±0.1	0.211	1.559	0.14	14
reac001	0.88±0.02	57.9±0.2	10.2±0.1	0.444	0.737	0.6	14
reac007	0.38±0.02	3.9±0.2	10.1±0.1	1.501	0266	5.6	16
reac006n	0.20±0.03	1.9±0.1	10.2±0.1	4.563	0.088	52	17
reac002a	0.160±0.003	n.d.	10.2±0.1	4.432	0.078	57	14
reac008	2.01±0.02	20.2±0.2	10.2±0.1	0.073	1.895	0.04	6
reac003	0.58±0.02	7.80±0.06	10.1±0.1	0.222	0.524	0.42	5
reac003n	0.58±0.02	7.78±0.07	10.1±0.1	0.235	0.424	0.45	5
reac009	0.15±0.02	n.d.	10.2±0.1	0.936	0.115	8.1	5
reac002bn	0.086±0.001	n.d.	10.2±0.1	2.185	0.054	40	5
reac002b	0.086±0.002	n.d.	10.2±0.1	2.366	0.052	45	5

Dissolved Ca^{2+} and Sr^{2+} concentrations were measured in four replicates by inductively coupled plasma – optical emission spectroscopy (ICP-OES). Dissolved inorganic carbon (DIC) was measured in duplicates on a Shimadzu$^{®}$ TOC550 analyzer. The pH of the inflow solution was checked before connecting the tubing to the reactor. The measured pH values matched the expected value of 10.15±0.1 (Table 6.1), confirming the 1:1 mixing ratio of the Ca^{2+} and CO_3^{2-} solutions. The pH of the outflow was also periodically measured and found to remain stable and equal to the inflow pH.

6.3.1.3 Determination of Calcite Growth Rates

At the end of an experiment, the crystal was removed from the reactor, washed with ethanol and dried for 1 h in the oven at 40°C, before weighing. The transfer to and from the reactor and balance was done by means of a Teflon$^{®}$ beaker with an inner diameter of 5 mm. No tools were used to pick up the crystal in order to avoid any breakage. Growth rates (R) were calculated as:

$$R = \left(\frac{(mt_1 - mt_0)}{mt_0} \right) 100 / t_1 \qquad (6.2)$$

where mt_0 and mt_1 are the initial and final crystal masses, respectively, and t_1 the duration of the growth experiment.

6.3.3 Sr Concentrations in Calcite Overgrowth

After the growth experiments, crystals were ablated using a deep ultra-violet-wavelength laser (193 nm, Lambda Physik excimer laser with GeoLas 200Q optics), which is essential for carbonate minerals, as they do not absorb laser radiation well at higher wavelengths (Jackson et al., 1992). Ablation was performed in a helium atmosphere at a pulse repetition rate of 6 Hz with an energy density at the sample surface of 2 J cm^{-2}. The aperture was set to make craters of 80 μm in diameter. A relatively low energy was used to increase the analysis time in the CaCO$_3$ overgrowth, before the bottom of the ablation crater reached the original crystal. The ablated material was analyzed with respect to time (and hence depth) using a quadrupole ICP-MS instrument (Micromass Platform ICP). Calibration was performed against NIST (U.S. National Institute of Standards and Technology) SRM 610 glass using the concentration data of Pearce et al. (1997), with Ca as an internal standard at a constant concentration of 40 wt %. Inter-elemental fractionation (Mank and Mason, 1999) was insignificant at the low depth/diameter ratio of the ablation craters produced in this study (typical ablation craters can be seen in Figure 6.2B).

A collision and reaction cell discussed in detail by Mason and Kraan (2002) was used to reduce spectral interferences on the minor isotopes of Ca (^{42}Ca, ^{43}Ca and ^{44}Ca). Multiple isotopes (^{24}Mg, ^{26}Mg, ^{27}Al, ^{55}Mn and ^{88}Sr) were used where possible to confirm accurate concentration determinations. Relative analytical error, based on repeated analyses of an independently calibrated in-house carbonate standard was ±4% for Sr. The Mg and Mn counts were used to identify the transition between the overgrowth and the original crystal, as both elements were virtually absent in the overgrowth, but present at constant levels (~700 ppm Mg, ~100 ppm Mn) in the seed crystals. A typical ablation spectrum is shown in Figure 6.4.
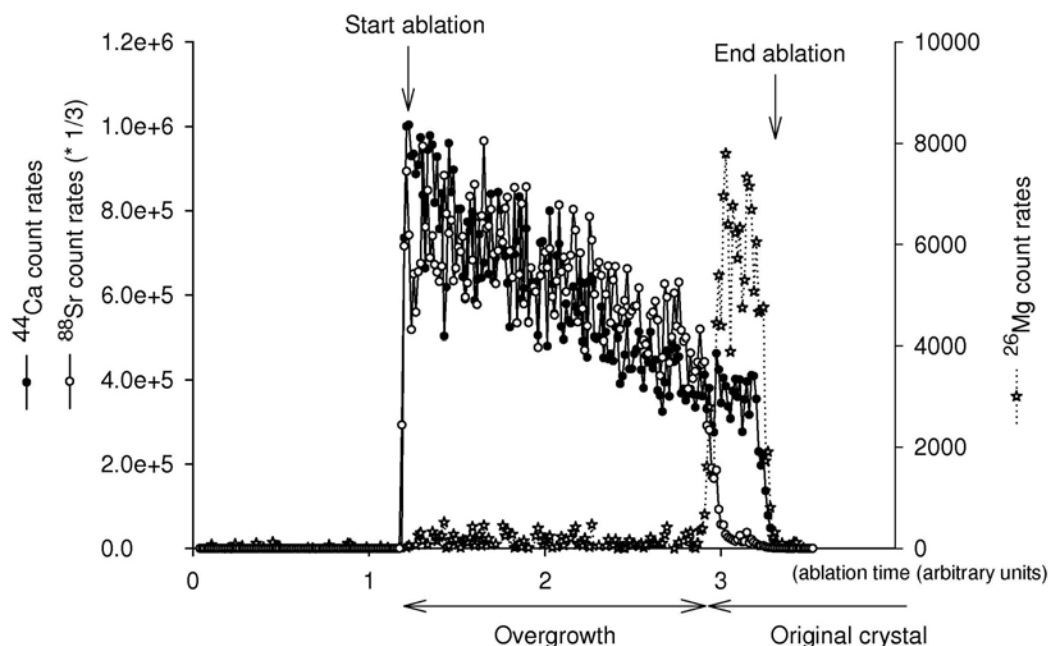
Figure 6.4: Typical ablation profile through a calcite crystal collected after a growth experiment with Sr-containing inflow solution. The Mg and Sr counts clearly distinguish the original seed crystal from the newly formed calcium carbonate layer. Both Ca and Sr counts decrease during the ablation as the bottom of the ablation crater steadily becomes deeper. The ratio of Sr to Ca, however, remains constant, indicating a homogeneous composition of the calcium carbonate overgrowth. Mg is present at concentrations of about 600 ppm in the original crystal, but is absent from the reaction fluids.

6.4 Results and Discussion

6.4.1 Growth Rates and Solution Stoichiometry

The calcite crystal growth rates determined with the single-crystal method vary by a factor of about 15 (Table 6.2). Although the growth kinetics depend on both the degree of supersaturation and the solution stoichiometry, most of the variability of the measured rates is due to changes of the concentration ratio $r = [Ca^{2+}]/[CO_3^{2-}]$ (Figure 6.5). At the experimental pH (10.2±0.1), and for both degrees of supersaturation (Ω = 5±1, 15±2), the rates decrease symmetrically away from $r = 1$. To our knowledge, this is the first time a growth rate optimum for a stoichiometric solution composition (r = 1) is reported for calcite.

Table 6.2: Initial and final crystal weights, plus the total durations of the growth experiments..

Experiment	Crystal	mt_0 (µg)	mt_1 (µg)	Duration (t_1) (h)
reac004n	B05	5222	5255	266
	B20	5102	5141	266
	B27	5568	5622	266
	B28	5133	5192	266
reac005	A14	2968	3338	821
	A15	2060	2400	821
	A18	2994	3362	821
	A21	2496	2925	819
reac001	003	3511	4456	723
	004	3803	4813	601
	010	3157	4202	771
	015	3662	4445	771
reac007	C01	3612	3992	612
	C12	3542	3975	612
	C13	3524	3936	612
	C21	3802	4142	612
reac006n	B15	4643	5156	1266
	B18	4841	5050	1266
	B26	4611	4802	1266
	B32	4836	5036	1266
reac002a	A08	2919	2976	841
	A13	2955	3014	841
	A20	2429	2498	841
	A24	3347	3412	841
reac008	C03	2923	3014	1045
	C06	3001	3072	1045
	C09	2854	2937	1045
reac003	007	1862	2838	1969
	014	4047	5432	1969
	017	3550	4750	1969
	020	2416	3539	1961
reac003n	B10	2684	3301	1079
	B29	2967	3738	1079
	B30	2913	3980	1079
	B38	2909	3470	1079
reac009	C11	3012	3527	1736
	C17	3235	3789	1736
	C08	3423	3905	1736
reac002bn	B02	3949	4072	1079
	B11	4069	4209	1079
	B29	3521	3632	1079
	B24	3583	3672	1079
reac002b	011	2769	2861	1369
	012	3433	3549	1369
	016	3196	3317	1369
	018	3594	3710	1369
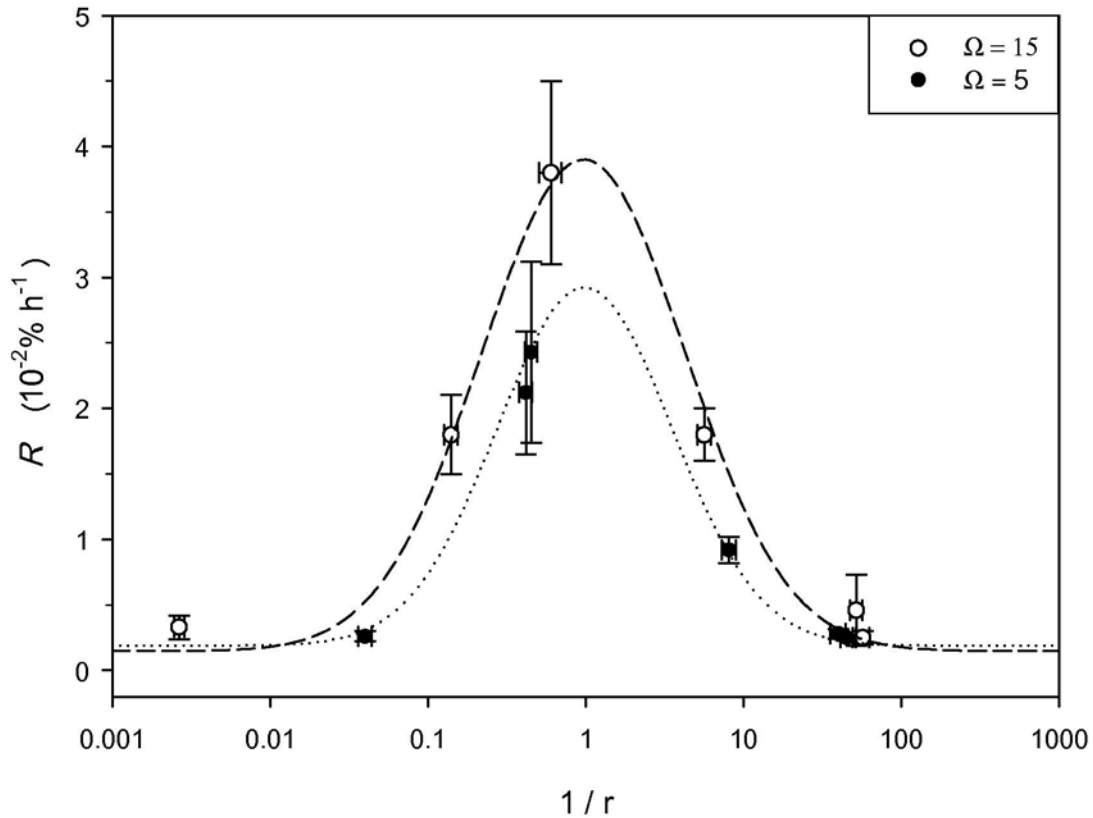
Figure 6.5: Growth rate versus the inverse of the solution $[Ca^{2+}]/[CO_3^{2-}]$ ratio, r, for two different degrees of supersaturation with respect to calcite (error bars denote standard deviations).

A number of authors have recognized that the growth rate of calcite and other divalent metal carbonates should depend on the relative abundances of metal and carbonate ions (Zuddas and Mucci, 1994; Sternbeck, 1997; Lebron and Suarez, 1998). However, the effects of supersaturation and solution stoichiometry are rarely assessed separately, because in most growth studies changes in r coincide with changes in Ω during the experiments (Christoffersen and Christoffersen, 1990; Nilson and Sternbeck, 1999; van der Weijden et al., 1997). In addition, experiments are generally conducted under conditions where $[Ca^{2+}] >> [CO_3^{2-}]$, thereby excluding the range of r in which the rate optimum is observed.

In an unpublished study, Winter and Burton (1992) found that the precipitation rate of calcite increased by more than one order of magnitude when r decreased from 2×10^5 to 1, while Ω was kept constant (reported in Zuddas and Mucci, 1994). This result implies that a potential rate optimum must occur at $r \leq 1$, which is consistent with our data. However, to fully characterize the effect of solution stoichiometry, growth kinetics must also be measured in solutions where $[Ca^{2+}] < [CO_3^{2-}]$. The most straightforward approach is to work at high pH, as done in the

present study, because CO_3^{2-} then represents a significant fraction of the dissolved inorganic carbon.

The symmetric rate dependence on solution stoichiometry in Figure 6.5 is similar to those observed by Chernov et al. (2006) for step propagation rates on calcium oxalate monohydrate ($CaC_2O_4 \cdot H_2O$) and magnesium oxalate dihydrate ($MgC_2O_4 \cdot 2H_2O$). For instance, at a constant supersaturation of Ω = 2.6, the propagation of [001] steps on the (100) face of $CaC_2O_4 \cdot H_2O$ drops by a factor of about 6 when the solution ratio, r = $[Ca^{2+}]/[C_2O_4^{2-}]$, increases from 1 to 10, or decreases from 1 to 0.1. At r values greater than 10, or smaller than 0.1, little further change in the step rate is observed. Chernov and coworkers interpreted the observed effect of r on the growth kinetics of $CaC_2O_4 \cdot H_2O$ and $MgC_2O_4 \cdot 2H_2O$ within the framework of the non-Kossel crystal growth theory for binary salts (Zhang and Nancollas, 1998). According to the theory, the attachment frequencies of the cation and anion to kink sites at the mineral surface are proportional to the respective concentrations in solution. A symmetric rate distribution is predicted when the proportionality constants, or frequency factors, are the same for the cation and anion.

Identical frequency factors for the incorporation of cation and anion into kink sites are rather unexpected, as also remarked by Chernov et al. (2006). The slower dehydration of the cation is often assumed to be rate-limiting for surface reaction-controlled growth of salt-type minerals (Nielsen, 1984). However, this would result in a rate optimum at r > 1, which is not the case. Possibly, the net negative surface charge of calcite at the high pH of our study (Van Cappellen et al., 1993) facilitates the incorporation of Ca^{2+} ions into the lattice, and results in comparable frequency factors for the attachment of Ca^{2+} and CO_3^{2-} ions. A logical extension of the work presented here would therefore be to determine the dependence of the calcite growth rate on r over a range of pH and, therefore, a range of surface charge and surface speciation.

Most natural waters are characterized by $[CO_3^{2-}]$ to $[Ca^{2+}]$ ratios much smaller than one. For example, r values for surface ocean waters are on the order of 100 (Zeebe and Westbroek, 2003), while in freshwater and marine sediment pore waters r typically varies between 50 and 2000 (Cai et al. 2000, Jahnke & Jahnke 2004, Mueller et al. 2003). Hence, the solution stoichiometries of these waters fall mostly outside the range of r where a strong effect on calcite growth kinetics is expected

(Figure 6.5). Changes in solution composition then mainly affect the growth rate via the degree of supersaturation. This, however, may no longer be the case for biologically mediated calcite precipitation. Organisms such as marine calcifying algae actively regulate Ca^{2+} transport from the surrounding seawater to the site of calcification through cell physiological processes (Langer et al., 2006a). In the highly controlled cell environment, r may differ significantly from the value in the bulk medium. Solution stoichiometry may therefore provide calcifying organisms with an additional means to control the mineralization process.

6.4.2 Sr Partition Coefficients

The LA-ICP-MS ablation spectra of the calcite overgrowths show the expected high ^{88}Sr and low ^{26}Mg signals (Figure 6.4). Average Sr partitioning coefficients derived from the ^{88}Sr and ^{44}Ca counts and the solution composition are listed in Table 6.3. The distribution coefficients increase with the calcite growth rate (Figure 6.6). As for the growth rate itself, most of the observed variability in D_{Sr} reflects differences in the $[Ca^{2+}]/[CO_3^{2-}]$ solution ratio among the experiments, rather than differences in the degree of supersaturation.

Table 6.3: Crystal growth rates and Sr partition coefficients. The growth rates are calculated from the measured weight increases of the calcite crystals during the growth experiments (Table 2). The Sr/Ca molar ratios are derived from the LA-ICP-MS measurements. The number of measurements (n_m), as well as the number of crystals (n_c) grown per inflow solution composition, are given (n.d.: not determined).

Experiment	$R\ 10^{-2}$ $(10^{-2}\ \%\ h^{-1})$	R nmol cm^{-2} min^{-1}	Sr/Ca mmol mol^{-1}	n_m/n_c	D_{Sr}
reac004n	0.33±0.09	5.9	n.d.	---	---
reac005	1.8±0.3	49.3	0.7±0.2	2/1	0.07±0.02
reac001	3.8±0.7	85.9	14±2	8/2	0.21±0.03
reac007	1.8±0.2	40.4	1.2±0.3	3/2	0.12±0.02
reac006n	0.5±0.3	8.9	0.20±0.05	4/2	0.02±0.01
reac002a	0.25±0.05	6.7	n.d.	---	---
reac008	0.27±0.04	7.03	0.3±0.01	1/1	0.03
reac003	2.1±0.5	52.2	1.51±0.05	2/2	0.11±0.05
reac003n	2.4±0.7	65	1.44±0.03	2/2	0.11±0.01
reac009	0.9±0.1	16.8	n.d.	---	---
reac002bn	0.28±0.04	6.3	n.d.	---	---
reac002b	0.25±0.02	6.1	n.d.	---	---
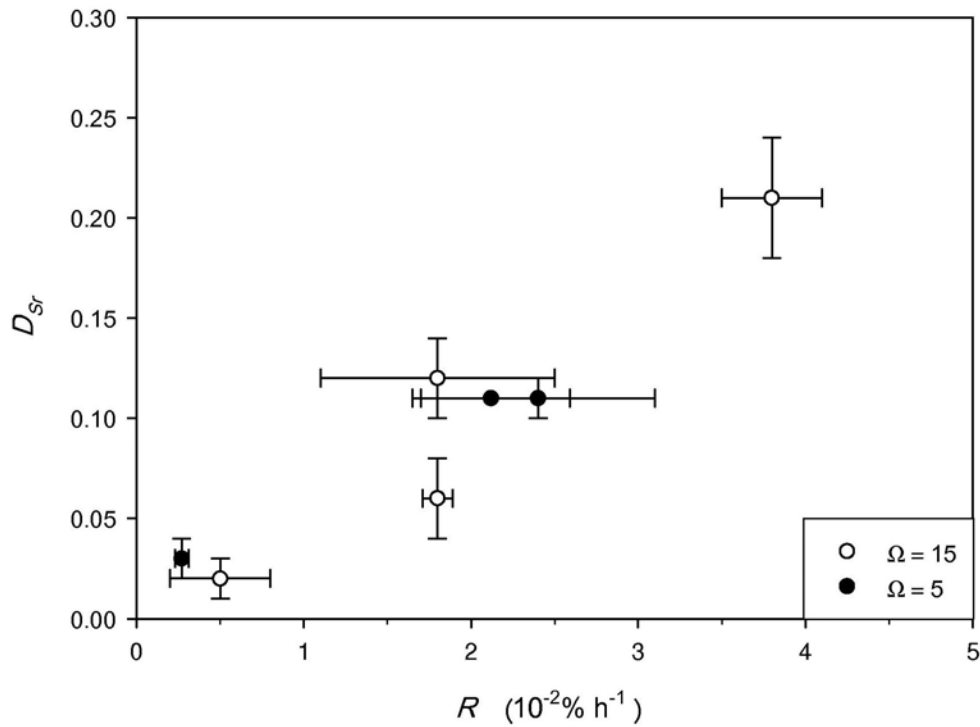
Figure 6.6: Distribution coefficient for Sr versus calcite growth rate for two different degrees of supersaturation (error bars denote standard deviations).

A positive correlation of D_{Sr} and the growth rate of calcite has also been reported by Tesoriero and Pankov (1996). These authors, however, used calcite powder as seed material instead of single crystals. Because of much higher mineral surface areas, precipitation rates in the experiments of Tesoriero and Pankov were up to two orders of magnitude faster than measured here. Nonetheless, the two studies yield trends between D_{Sr} and the growth rate that are in reasonable agreement, when normalizing the growth rates to the geometric surface areas of the two different calcite seed materials used (Figure 6.7).

In both studies, the lowest values of D_{Sr} are on the order of 0.02, which corresponds to the equilibrium value, $K_{D_{Sr}}$ (Rimstidt et al., 1998). According to Tesoriero and Pankov, their highest incorporation of Sr ($D_{Sr} = 0.14$) is partially due to formation of discrete inclusions of $SrCO_3$. Similarly, our highest value of D_{Sr} (0.21) corresponds to the experiment in which the solution was supersaturated with respect to $SrCO_3$ ($\Omega = 3$). If the two highest D_{Sr} values are excluded, the combined data set in Figure 6.7 implies a saturation plateau for Sr incorporation around $D_{Sr} \approx 0.12$. A maximum D_{Sr} value around 0.12 has been proposed by Stoll et al. (2002), based on

the surface enrichment model for trace elements of Watson (1996) and Watson and Liang (1995).
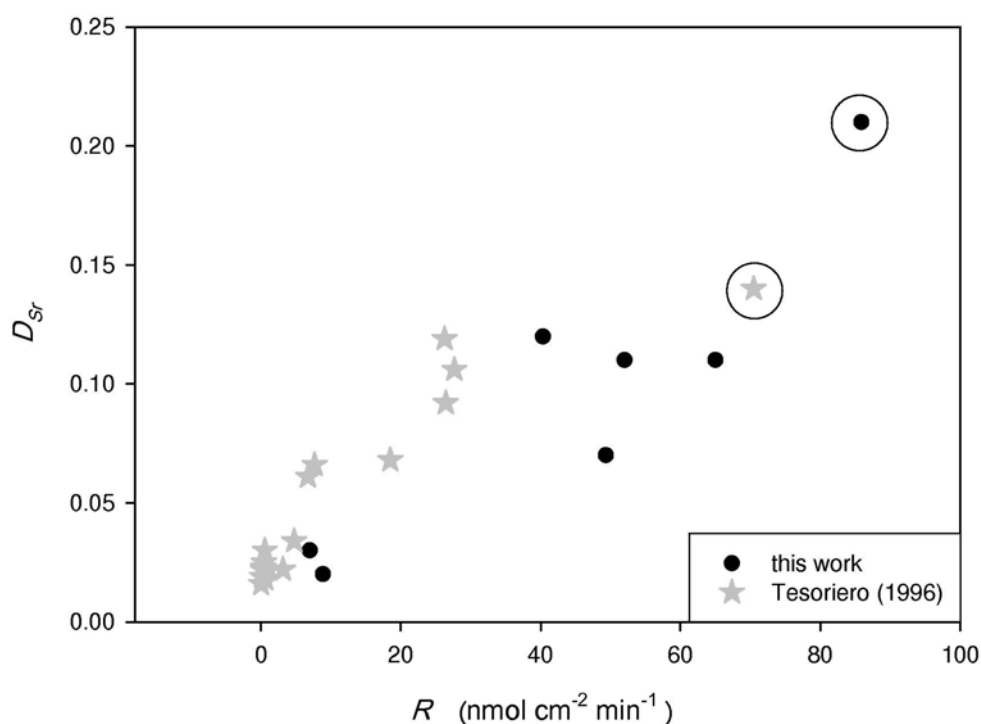
Figure 6.7: Comparison of D_{Sr} values obtained in this study and in Tesoriero and Pankow (1996), plotted *versus* the calcite growth rates normalized to the surface areas of the seed materials. The encircled data points may be affected by the precipitation of $SrCO_3$. See text for detailed discussion.

6.5 Conclusions

Calcite growth experiments carried out at constant pH and supersaturation demonstrate that the growth kinetics depend on solution stoichiometry. The growth rate is maximal in a stoichiometric solution, i.e., when $r = [Ca^{2+}]/[CO_3^{2-}] = 1$, and decreases symmetrically away from $r = 1$. The effect of solution stoichiometry is most pronounced for values of r between 0.1 and 10. Within this range, an increasing departure from $r = 1$ may lead to a decrease in the growth rate, even if the degree of supersaturation of the solution actually increases. The symmetric rate distribution around $r = 1$ suggests similar frequency factors for the attachment of cation and anion to kink sites at the mineral surface, under the high pH (10.2) conditions of this study.

The incorporation of strontium in calcite increases with increasing growth rate. The Sr distribution coefficients obtained here for single crystals are consistent with values in earlier studies using suspended calcite powders, when normalizing the growth rate to the calcite surface area. The Sr/Ca ratio in calcite thus reflects the combined effects of the supersaturation and stoichiometry of the aqueous phase on the crystal growth kinetics. Both supersaturation and solution stoichiometry at the site of calcite formation are potentially modulated by cellular processes in calcifying organisms, and may therefore contribute to the "vital effect" on Sr/Ca ratios.

References

Aizenberg, J., Hanson, J., Koetzle, T. F., Weiner, S., and Addadi, L., 1997. Control of macromolecule distribution within synthetic and biogenic single calcite crystals. *J. Amer. Chem. Soc.* **119**, 881 - 886.

Albright, J. N., 1971. Vaterite stability. *Am. Mineral.* **56**, 620 - 624.

Allen, T., 1999. *Surface area and pore size determination*. Kluwer Academic.

Baitalow, F., Wolf, G., and Schmidt, H. G., 1998. Thermochemical investigations of calcium carbonate phase transitions I. Thermal activated vaterite-calcite transition. *J. Therm. Anal. Calorim.* **52**, 5-16.

Beattie, P., Drake, M., Jones, J., Leeman, W., Longhi, J., McKay, G., Nielsen, R., Palme, H., Shaw, D., Takahashi, E., and Watson, B., 1993. Terminology for trace-element partitioning. *Geochim. Cosmochim. Acta* **57**, 1605 - 1606.

Beniash, E., Aizenberg, J., Addadi, L., and Weiner, S., 1997. Amorphous calcium carbonate transforms into calcite during sea urchin larval spicule growth. *Proc. R. Soc. Lond. B* **164**, 461 - 465.

Bischoff, J. L., 1968. Catalysis, inhibition, and the calcite-aragonite problem. II. The vaterite-aragonite transformation. *Amer. J. Sci.* **266**, 80-90.

Bischoff, J. L., Fitzpatrick, J. A., and Rosenbauer, R. J., 1993. The solubility and stabilization of ikaite ($CaCO_3 \bullet 6H_2O$) from 0°C: Environmental and paleoclimatic implications for thinolite tufa. *The Journal of Geology* **101**, 21 - 33.

Boyle, E. A., 1981. Cadmium, zinc, copper, and barium in foraminifera tests. *Earth Planet. Sci. Lett.* **53**, 11-35.

Boyle, E. A., 1988. Cadmium: chemical tracer of deepwater paleoceanography. *Paleoceanogr.* **3**, 471-489.

Brečević, L. and Nielsen, A. E., 1989. Solubility of amorphous calcium carbonate. *J. Cryst. Growth.* **98**, 504 - 510.

Brečević, L., Nothig-Laslo, V., Kralj, D., and Popovic, S., 1996. Effect of divalent cations on the formation and structure of calcium carbonate polymorphs. *J. Chem. Soc. Faraday Trans.* **92**, 1017-22.

Buchardt, B., Seaman, P., Stockmann, G., Vous, M., Wilken, U., Duwel, L., Kristiansen, A., Jenner, C., Whiticar, M. J., Kristensen, R. M., Petersen, G. H., and Thorbjorn, L., 1997. Submarine columns of ikaite tufa. *Nature (London)* **390**, 129-130.

Burton, W. K., Cabrera, N., and Frank, F. C., 1951. The growth of crystals and the equilibrium structure of their surfaces. *Philos. Trans. Roy. Soc. London. Ser. A.* **243**, 299 - 358.

Butler, I. B. and Rickard, D., 2000. Framboidal pyrite formation via the oxidation of iron (II) monosulfide by hydrogen sulphide. *Geochim. Cosmochim. Acta* **64**, 2665-2672.

Butler, J. N., 1982. *Carbon Dioxide Equilibria and Their Application.* Addison-Wesley Publishing Company.

Carlström, D., 1963. A crystallographic study of vertebrate otolith. *Biol. Bull.* **125**, 441 - 463.

Cheary, R. W. and Coelho, H., 1996. Xfit. In: Program XFIT deposited in the CCP14 Powder Diffraction Library, E. P. S. R. C., Darsbury Laberotory,Warrington UK. Internet address http://gserv1.dl.ac.uk/CCP/CCp14/index.html.

Chernov, A. A., 2001. Crystal growth science between the centuries. *J. Mater. Sci .- Mater. Electron.* **12**, 437-449.

Chernov, A. A., Petrova, E. V., and Rashkovich, L. N., 2006. Dependence of the CaOx and MgOx growth rate on solution stoichiometry. Non-Kossel crystal growth. *J. Crystal Growth* **289**, 245-254.

Christoffersen, J. and Christoffersen, M. R., 1990. Kinetics of spiral growth of calcite crystals and determination of the absolute rate constant. *J. Crystal Growth* **100**, 203-211.

Curti, E., 1997. Coprecipitation of radionuclides: basic concepts, literature review and first applications. *PSI-Bericht* Nr. 97-10.

Dickens, B. and Brown, W. E., 1970. Crystal structure of calcium carbonate hexahydrate at about ~ -120°. *Inorg. Chem.* **9**, 480-6.

Dickinson, S. R., Henderson, G. E., and McGrath, K. M., 2002. Controlling the kinetic versus thermodynamic crystallisation of calcium carbonate. *J. Crystal Growth.* **244**, 369-378.

Dickinson, S. R. and McGrath, K. M., 2001. Quantitative determination of binary and tertiary calcium carbonate mixtures using powder X-ray diffraction. *Analyst (Cambridge, U. K.)* **126**, 1118-1121.

Dingley, D. J. and Randle, V., 1992. Microtexture determination by electron back-scatter diffraction. *Journal of Materials Science (Historical Archive)* **27**, 4545-4566.

Elfil, H. and Roques, H., 2001. Role of hydrated phases of calcium carbonate on the scaling phenomenon. *Desalination* **137**, 177 - 186.

Euvrard, M., Filiatre, C., and Crausaz, E., 2000. A cell to study in situ electrocrystallization of calcium carbonate. *J. Crystal Growth.* **216**, 466-474.

Falkowski, P. and Raven, J., 1997. *Aquatic Photosynthesis.* Blackwell Science, Oxford.

Fernandez-Gonzalez, A. and Prieto, M., 1999. Concentric zoning pattern in crystallizing (Cd,Ca)CO_3 solid solution from aqueous solutions. *Mineral. Mag.* **63**, 331 - 343.

Fischbeck, R. and Müller, G., 1971. Monohydrocalcite, hydromagnesite, nesquehonite, dolomite, aragonite, and calcite in speleothems of the Fränkische Schweiz, Western Germany. *Contrib. Mineral. Petrol.* **33**, 87-92.

Fleischer, M., 1969. Occurrences of CaCO3•H2O and its naming. *Science* **166**, 1309.

Friedman, G. M. and Schultz, D. J., 1995. Precipitation of vaterite ($CaCO_3$) during oilfield drilling. *Mineral. Mag.* **59**, 353-4.

Gauldie, R. W., 1996. Effects of temperature and vaterite replacement on the chemistry of metal ions in the otoliths of *Oncorhynchus tshawytscha. Can. J. Fish. Aquat. Sci.* **53**, 2015-2026.

Gibson, R. E., Wyckoff, R. W. G., and Merwin, H. E., 1925. Vaterite and μ-calcium carbonate. *Amer. J. Sci.* **10**, 325 - 333.

Giralt, S., Julia, R., and Klerkx, J., 2001. Microbial biscuits of vaterite in lake Issyk-Kul (Republic of Kyrgyzstan). *J. Sediment. Res.* **71**, 430-435.

Gussone, N., Langer, G., Thoms, S., Nehrke, G., Eisenhauer, A., Riebesell, U., and Wefer, G., 2006. Cellular calcium pathways and isotope fractionation in Emiliania huxleyi. *Geology* **34**, 625-628.

Gustafsson, J. P., 2004. Visual Minteq ver. 2.40. KTH, (http://www.lwr.kth.se/English/OurSoftware/vminteq/index.htm), Stockholm, Sweden.

Halliday, A. N., 2006. The origin of the Earth – What's new? *Elements* **2**, 205 - 210.

Han, Y. S., Hadiko, G., Fuji, M., and Takahashi, M., 2006. Crystallization and transformation of vaterite at controlled pH. *J. Crystal Growth.* **289**, 269-274.

Heide, F., 1924. Über den Vaterit. *Centralblatt für Mineralogie*, 641 - 651.

Hobbs, M. Y. and Reardon, E. J., 1999. Effects of pH on boron coprecipitation by calcite: Futher evidence for nonequilibrium partitioning of trace elements. *Geochim. Cosmochim. Acta* **63**, 1013 - 1021.

Houghton, J. T., Ding, Y., Griggs, D. J., Noguer, M., Linden, P. J. V. d., Dai, X., Maskell, K., and Johnson, C. A., 2001. *Climate Change: The Scientific Basis: Contribution of Working Group 1 to the Third Asessment Report of the Intergovernment Panel of Climate Change*. Cambridge University Press, Cambridge.

Jackson, S. E., Longerich, H. P., Dunning, G. R., and Fryer, B. J., 1992. The application of laser-ablation microprobe-inductively coupled plasma-mass spectrometry (LAM-ICP-MS) to in situ trace element determination in minerals. *Canadian Mineral.* **30**, 1049 - 1064.

Johnston, J., Merwin, H. E., and Williamson, E. D., 1916. The several forms of calcium carbonate. *Amer. J. Sci.* **41**, 473 - 512.

Kamhi, S., 1963. On the structure of vaterite $CaCO_3$. *Acta Cryst.* **16**, 770-772.

Kanakis, J. and Dala, E., 2000. The crystallization of vaterite on fibrin. *J. Crystal Growth.* **219**, 277 - 282.

Kashchiev, D., 2000. *Nucleation.* Butterworth-Heinemann.

Katsifaras, A. and Spanos, N., 1999. Effect of inorganic phosphate ions o n the spontaneous precipitation of vaterite and on the transformation of vaterite to calcite. *J. Crystal Growth.* **204**, 183 - 190.

Kitamura, M., 2001. Crystallization and transformation mechanism of calcium carbonate polymorphs and the effect of magnesium ion. *J. Colloid. Interf. Sci.* **236**, 318-327.

Kitano, Y., Kanamori, N., and Oomori, T., 1971. Measurements of distribution coefficients of strontium and barium between precipitate and solution - Abnormally high values of distribution coefficients measured at early stages of carbonate formation. *Geochem. J.* **4**, 183 - 206.

Kitano, Y. and Oomori, T., 1971. The coprecipitation of uranium with calcium carbonate. *J. Oceanogr. Soc. Japan* **27**, 34 - 42.

Kleber, I., Bautsch, J., and Bohm, H.-J., 1990. *Einführung in die Kristallographie.* Verlag Technik GmbH Berlin.

Kossel, W., 1927. Zur Theorie des Kristallwachstums. *Nachrich. Ges. Wiss. Göttingen, Math.-phys. Klasse*, 135 -143.

Kralj, D. and Brecevic, L., 1995. Dissolution kinetics and solubility of calcium carbonate monohydrate. *Colloids Surf., A* **96**, 287 - 293.

Kralj, D., Brecevic, L., and Kontrec, J., 1997. Vaterite growth and disssolution in aqueous solution III. Kinetics of transformation. *J. Crystal Growth.* **177**, 248 - 257.

Kralj, D., Brecevic, L., and Nielsen, A. E., 1990. Vaterite growth and dissolution in aqueous solution I. Kinetics of crystal growth. *J. Crystal Growth.* **104**, 793 - 800.

Kralj, D., Brecevic, L., and Nielsen, A. E., 1994. Vaterite growth and dissolution in aqueous solution II. Kinetics of disolution. *J. Crystal Growth.* **143**, 169 - 276.

Langer, G., Gussone, N., Nehrke, G., Riebesell, U., Eisenhauer, A., Kunert, H., Rost, B., Trimborn, S., and Thoms, S., 2006a. Coccolith strontium to calcite ratios in *Emiliania huxleyi*: The dependence on seawater strontium and calcium concentrations. *Limnol. Oceanogr.* **51**, 310 - 320.

Langer, G., Gussone, N., Nehrke, G., Riebesell, U., Eisenhauer, A., and Thoms, S., 2006b. Calcium isotope fractionation during coccolith formation in *Emiliania huxleyi*: Independence of growth and calcification rate. *Geochem. Geophys. Geosys (in review).*

Langmuir, D., 1997. *Aqueous Environmental Geochemistry.* Prentice Hall.

Lasaga, A. C., 1998. *Kinethic Theory in Earth Sciencees.* Princeton University Press.

Lea, D. and Boyle, E., 1989. Barium content of benthic foraminifera controlled by bottom-water composition. *Nature* **338**, 751-753.

Lea, D. W. and Boyle, E. A., 1990. Barium in planctic foraminifera. *Geochim. Cosmochim. Acta* **55**, 3321-3331.

Lea, D. W., Martin, P. A., Chan, D. A., and Spero, H. J., 1995. Calcium uptake and calcification rate in the planctonic foraminifer *Orbulina universa*. *J. Foramin. Res.* **25**, 14-23.

Lea, D. W. and Spero, H. J., 1992. Experimental determination of barium uptake in shells of the planctonic foraminifera *Orbulina universa* at 22°C. *Geochim. Cosmochim. Acta* **56**, 2673-2680.

Lebron, I. and Suarez, D. L., 1998. Kinetics and mechanisms of precipitation of calcite as affected by P_{CO2} and organic ligands at 25°C. *Geochim. Cosmochim. Acta* **62**, 405-416.

Lemarchand, D., Wasserburg, G. J., and Papanastassiou, D. A., 2004. Rate-controlled calcium isotope fractionation in synthetic calcite. *Geochim. Cosmochim. Acta* **68**, 4665.

Lenaz, D. and Miletic, M., 2000. Vaterite otoliths in some freshwater fishes of the Lower Friuli Plain (NE Italy). *Neues Jahrbuch fur Mineralogie, Monatshefte* **11**, 522-528.

Linck, G., 1903. Die Bildung der Oolithe und Rogensteine. *Neues Jahrb. Mineral.* **16**, 495 - 513.

Lorens, R. B., 1981. Sr, Cd, Mn and Co distribution coefficients in calcite as a function of calcite precipitation rate. *Geochim. Cosmochim. Acta* **45**, 533-561.

Ma, H. Y. and Lee, I. S., 2006. Characterization of vaterite in low quality freshwater-cultured pearls. *Materials Science and Engineering: C* **26**, 721-723.

Mackenzie, J. E., 1923. Calcium carbonate hexahydrate. *J. Chem. Soc., Trans.* **123**, 2409 - 2417.

Mank, A. G. K. and Mason, P. R. D., 1999. A critical assessment of laser ablation ICP-MS as an analytical tool for depth analysis in silica-based glas samples. *Journal of Analytical Atomic Spectroscopy* **14**, 1141 - 1153.

Manoli, F., Kanekis, J., Malkaj, P., and Dalas, E., 2002. The effect of aminoacids on the crystal growth of calcium carbonate. *J. Crystal Growth.* **236**, 363 - 370.

Manoli, F., Koutsopoulos, S., and Dalas, E., 1997. Crystallization of calcite on chitin. *J. Crystal Growth.* **182**, 116-124.

Markov, I. V., 2003. *Crystal Growth for Beginners*. World Science Publishing Co.

Marland, G., 1975. The stability of CaCO3·6H2O (ikaite). *Geochim. Cosmochim. Acta* **39**, 83 - 91.

REFERENCES

Mashiotta, T. A., Lea, D. W., and Spero, H. J., 1997. Experimental determination of cadmium uptake in shells of the planctonic foraminifera *Orbulina universa* and *Globigerina buloides*: Implications for surface water paleoreconstructions. *Geochim. Cosmochim. Acta* **61**, 4053-4065.

Mason, P. R. D. and Kraan, W. J., 2002. Attenuation of spectral interferences during laser ablation inductively coupled plasma mass spectroscopy (LA-ICP-MS) using an rf only collision and reaction cell. *Journal of Analytical atomic Spectroscopy* **17**, 858 - 867.

McIntire, W. L., 1963. Trace element partition coefficients - a review of theory and applications to geology. *Geochim. Cosmochim. Acta* **27**, 1209 - 1264.

Morel, F. M. M. and Hering, J. G., 1993. *Principles and Applications of Aquatic Chemistry*. John Wiley & Sons.

Morse, J. W. and Bender, M. L., 1990. Partition coefficients in calcite: Examination of factors influencing the validity of experimental results and their application to natural systems. *Chem. Geol.* **82**, 265-277.

Morse, J. W. and Mackenzie, F. T., 1990. *Geochemistry of Sedimentary Carbonates*. Elsevier, Amsterdam.

Mucci, A., 1986. Growth kinetics and composition of magnesian calcite overgrowth precipitated from seawater: Quantitative influence of orthophosphate ions. *Geochim. Cosmochim. Acta* **50**, 2253 - 2265.

Mucci, A. and Morse, J. W., 1983. The incorporation of Mg^{2+} and Sr^{2+} into calcite overgrowths: influences of growth rate and solution composition. *Geochim. Cosmochim. Acta* **47**, 217-233.

Nancollas, G. H. and Reddy, M. M., 1971. The crystallization of calcium carbonate. II. Calcite growth mechanism. *J. Colloid Interface Sci.* **37**, 824-830.

Nielsen, A. E., 1964. *Kinetics of Precipitation*. Pergamon Press.

Nielsen, A. E., 1984. Electrolyte crystal growth mechanism. *J. Crystal Growth.* **67**, 289 - 310.

Nielsen, A. E. and Toft, J. M., 1984. Electrolyte crystal growth kinetics. *J. Crystal Growth.* **67**, 278 - 288.

Nilsson, O. and Sternbeck, J., 1999. A mechanistic model for calcite crystal growth using surface speciation. *Geochim. Cosmochim. Acta* **63**, 217 - 225.

Noethig-Laslo, V. and Brecevic, L., 1998. Mode and sites of incorporation of divalent cations in vaterite. *J. Chem. Soc. Faraday Trans.* **94**, 2005-2009.

Noethig-Laslo, V. and Brecevic, L., 2000. An EPR study of primary paramagnetic centers in Cd2+-doped vaterite. *PCCP* **2**, 5328-5332.

Ostwald, W., 1897. Studien über die Bildung und Umwandlung fester Körper. *Zeitschrift für Physikalische Chemie* **22**, 289 - 330.

Ogino, T., Suzuki, T., and Sawada, K., 1987. The formation and transformation mechanism of calcium carbonate in water. *Geochim. Cosmochim. Acta* **51**, 2757 - 2767.

Paquette, J. and Reeder, R. J., 1995. Relationship between surface structure, growth mechanism, and trace element incorporation in calcite. *Geochim. Cosmochim. Acta* **59**, 735 - 749.

Pauly, H., 1963. "Ikaite" a new mineral from Greenland. *Arctic* **16**, 263-4.

Pearce, N. J. G., Perkins, W. T., Westgate, J. A., Gorton, M. P., Jackson, S. E., Neal, C. R., and Chenery, S. P., 1997. A compilation of new and published major and trace element data for NIST SRM 610 and NIST SRM 612 glass reference materials. *Geostandards Newsletter* **21**, 115 - 144.

Pilson, M. E. Q., 1998. *An Introduction to the Chemistry of the Sea*. Prentice Hall.

Pingitore, N. E. and Eastman, M. P., 1984. The experimental partitioning of Ba^{2+} into calcite. *Chem. Geol.* **45**, 113-120.

Plummer, L. N. and Busenberg, E., 1982. The solubilities of calcite, aragonite and vaterite in Co_2-H_2O solutions between 0 and 90°C, and an evaluation of the aqueous model for the system $CaCO_3$-CO_2-H_2O. *Geochim. Cosmochim. Acta* **46**, 1011-1040.

Prieto, M., Fernandez-Gonzalez, A., Putnis, A., and Fernandez-Diaz, L., 1997. Nucleation, growth, and zoning phenomena in crystallizing $(Ba,Sr)CO_3$, $Ba(SO_4,CrO_4)$, $(Ba,Sr)SO_4$, and $(Cd,Ca)CO_3$ solid solution from aqueous solution. *Geochim. Cosmochim. Acta* **61**, 3383 - 3397.

Putnis, A., 1995. *Introduction to Mineral Sciences*. Cambridge University Press.

Reeder, R. J., 1996. Interaction of divalent cobald, zink, cadmium, and barium with the calcite surface during layer growth. *Geochim. Cosmochim. Acta* **60**, 1543-1552.

Rimstidt, J. D., Bolag, A., and Webb, J., 1998. Distribution of trace elements between carbonate minerals and aqueous solutions. *Geochim. Cosmochim. Acta* **62**, 1851-1863.

Rock, P. A. and Gordon, A. Z., 1976. Determination of Gibbs energies for solid-solid phase transitions in electrochemical double cells without liquid junction: calcite, aragonite, and vaterite. *J. Amer. Chem. Soc.* **98**, 2364-5.

Russel, A. D., Emerson, S., Nelson, B. K., Erez, J., and Lea, D. W., 1994. Uranium in foraminiferal calcite as a record of seawater uranium concentrations. *Geochim. Cosmochim. Acta* **58**, 671-681.

Sawada, K., 1998. Mechanisms of crystal growth of ionic crystals in solution. Formation, transformation, and growth inhibition of calcium carbonates. In: Ohtaki, H. (Ed.), *Crystallization Processes*. John Wiley & Sons.

Scheffer and Schachtschabel, 1992. *Lehrbuch der Bodenkunde*. Ferdinat Enke Verlag, Stuttgart.

Schneider, R. R., Schulz, H. D., and Hensen, C., 2000. Marine Carbonates: Their Formation and Destruction. In: Schulz, H. D. and Zabel, M. Eds.), *Marine Geochemistry*. Springer.

Spanos, N. and Koutsoukos, P. G., 1998. The transformation of vaterite to calcite: effect of the conditions of the solutions in contact with the mineral phase. *J. Crystal Growth.* **191**, 783 - 790.

Spero, H. J., Bijma, J., Lea, D. W., and Bemis, B. E., 1997. Effect of seawater carbonate concentration on foraminiferal carbon and oxygen isotopes. *Nature* **390**, 497-500.

Sternbeck, J., 1997. Kinetics of rhodochrosite crystal growth at 25°C : The role of surface speciation. *Geochim. Cosmochim. Acta* **61**, 785 - 793.

Stoll, H. M., Rosenthal, Y., and Falkowski, P., 2002. Climate proxies from Sr/Ca of coccolith calcite: calibrations from continuous culture of *Emiliania huxleyi. Geochim. Cosmochim. Acta* **66**, 927-936.

Stranski, I. N., 1928. Zur Theorie des Kristallwachstums. *Zeitschrift für physikalische Chemie (Leipzig)* **136**, 259 - 278.

Stumm, W., 1992. *Chemistry of the Solid-Water Interface.* John Wiley & Sons.

Sundquist, E. T. and Visser, K., 2005. The geologic history of the carbon cycle. In: Schlesinger, W. H. (Ed.), *Biogeochemistry*. Elsevier, Amsterdam.

Sutor, D. J. and Wooley, S. E., 1968. Gallstone of unusual composition: calcite, aragonite, and vaterite. *Science* **159**, 1113-1114.

Taylor, G. F., 1975. The occurance of monohydrocalcite in two small lakes in the South-East of South Australia. *Am. Mineral.* **60**, 690 - 697.

Temmam, M., Paquette, J., and Vali, H., 2000. Mn and Zn incorporation into calcite as a function of chloride aqueous concentration. *Geochim. Cosmochim. Acta* **64**, 2417-2430.

Teng, H. H., Dove, P. M., and Yoreo, J. J. D., 1999. Reversed calcite morphologies induced by microscopic growth kinetiks: Insight into biomineralization. *Geochim. Cosmochim. Acta* **63**, 2507 - 2512.

Tesoriero, A. J. and Pankow, J. F., 1996. Solid solution partitioning of Sr^{2+}, Ba^{2+}, and Cd^{2+} to calcite. *Geochim. Cosmochim. Acta* **60**, 1053 - 1063.

Tsuno, H., Kagi, H., and Akagi, T., 2001. Effects of trace lanthanum ion on the stability of vaterite and transformation from vaterite to calcite in an aquatic system. *Bulletin Chem. Soc. Japan* **74**, 479-486.

Tsuno, H., Kagi, H., and Akagi, T., 2002. High yield of vaterite precipitation induced by trace lanthanum ion from a supersaturated solution of calcium carbonate at 50.degree.C. *Chem. Lett.*, 960-961.

Tullett, S. G., Board, R. G., and Love, G., 1976. Vaterite deposition during eggshell formation in the cormorant, gannet and shag, and in 'shell less' eggs of the domestic fowl. *Acta Zoologica* **57**, 79-87.

Turnbull, A. G., 1973. A thermodynamical study of vaterite. *Geochim. Cosmochim. Acta* **37**, 1593 - 1601.

Van Cappellen, P., 1990. The formation of marine apatite: A kinetic study. PhD thesis, Yale University.

Van Cappellen, P., Charlet, L., Stumm, W., and Wersin, P., 1993. A surface complexation model of the carbonate mineral-aqueous solution interface. *Geochim. Cosmochim. Acta* **57**, 3505-3518.

van der Gaans, 2003. Personal communication

van der Weijden, R. D. and Comans, R. N. J., 1995. Interactions between cadmium and calcite. 5. Precipitation and heavy metal immobilization resulting from carbonation of filtrated bottom ash leaches. PhD, Utrecht.

van der Weijden, R. D., van der Heijden, A. E., Witkamp, G. J., and van Rosmalen, G. M., 1997. The influence of total calcium and total carbonate on the growth rate of calcite. *J. Crystal Growth.* **171**, 190-196.

Vater, H., 1897. XXI. Über den Einfluss der Lösungsgenossen auf die Krystallisation des Calciumcarbonates. *Zeitschr. f. Kristallographie* **27**, 477 - 504.

Vater, H., 1899. XXV. Beitrag zur Kentniss der Umsetzungen zwischen Calciumcarbonat und Alkalisulfat sowie über die Bildung der Alkalicarbonate in der Natur. *Zeitschr. f. Kristallographie* **30**, 373 - 386.

Vecht, A. and Ireland, T. G., 2000. The role of vaterite and aragonite in the formation of pseudo-biogenic carbonate structures: Implications for Martian exobiology. *Geochim. Cosmochim. Acta* **64**, 2719 - 2725.

Wada, N., Yamashita, K., and Umegaki, T., 1995. Effects of divalent cations uppon nucleation, growth and transformationof calcium carbonate polymorphs under conditions of double diffusion. *J. Crystal Growth.* **148**, 297 - 304.

Watson, E. B., 1996. Surface enrichment and trace-element uptake during crystal growth. *Geochim. Cosmochim. Acta* **60**, 5013-5020.

Watson, E. B. and Liang, Y., 1995. A simple model for sector zoning in slowly grown crystals: Implications for growth rate and lattice diffusion, with emphasis on accessory minerals in crustal rocks. *Am. Mineral.* **80**, 1179 - 1187.

Winter D. J. and Burton E. A. (1992) Experimental investigation a_{Ca}/a_{CO_3} ratio on the kinetics of calcite precipitation: implication for the rate equation and trace element incorporation. *GSA Abstr. Preg A37* (abstr.).

Wittmann, K. J. and Ariani, A. P., 1996. Some aspects of fluorite and vaterite precipitation in marine environments. *Marine Ecology* **17**, 213-219.

Wolf, G., Königsberger, E., Schmidt, H. G., Königsberger, L. C., and Gamsjäger, H., 2000. Thermodynamic aspects of the vaterite-calcite phase transition. *J. Therm. Anal. Calorim.* **60**, 463-472.

Wolthers, M., 2003. Goechemistry and environmental mineralogy of the iron-sulfur-arsenic system. PhD Thesis, Utrecht University.

Wray, J. L. and Daniels, F., 1957. Precipitation of calcite and aragonite. *J. Am. Chem. Soc.* **79**, 2031-4.

Zeebe, R. E. and Westbroek, P., 2003. A simple model for the $CaCO_3$ saturation state of the ocean: The ''Strangelove,'' the ''Neritan,'' and the ''Cretan'' Ocean. *Geochem. Geophys. Geosys.* **4**, doi:10.1029/2003GC000538.

Zeebe, R. E. and Wolf-Gladrow, D., 2001. *CO_2 in Seawater:Equilibrium, Kinetics, Isotopes*. Elsevier Science B.V., Amsterdam.

Zhang, J. and Nancollas, G. H., 1990. Kink densities along a crystal surface step at low temperatures and under non equilibrium conditions. *J. Crystal Growth.* **106**, 181-190.

Zhang, J. and Nancollas, G. H., 1992. Influence of calcium/sulfate molar ratio on the growth rate of calcium sulfate dihydrate at constant supersaturation. *J. Crystal Growth.* **118**, 287-294.

Zhang, J. and Nancollas, G. H., 1998. Kink density and rate of step movement during growth and dissolution of an AB crystal in a nonstoichiometric solution. *J. Colloid. Interf. Sci.* **200**, 131-145.

Zuddas, P. and Mucci, A., 1994. Kinetics of calcite precipitation from seawater: I. A classical chemical kinetics description for strong electrolyte solutions. *Geochim. Cosmochim. Acta* **58**, 4353-4362.

Summary and Perspective

This thesis focuses on two aspects of calcite precipitation from aqueous solution. In the first part (*Chapters 4* and *5*), the precipitation from the precursor phase vaterite is investigated, whereas the second part (*Chapter 6*) deals with the effects of solution stoichiometry on the growth rate and the incorporation of Sr.

The morphology of vaterite precipitated by bubbling CO_2 through a $CaCl_2$ solution is framboidal aggregates. It is not possible, even when using the identical experimental setup and conditions, to reproduce aggregates having identical morphology. The density of the aggregates and crystallite size can vary significantly between batches. The differences between batches result in "loosely" "and "densely" packed aggregates, having different specific surface areas.

For the aggregates used in this study, a transformation of vaterite aggregates into calcite may occur entirely within the aggregate itself. It was further shown that the transformation rate is not limited by the dissolution of vaterite, in contrast to some reports in the literature of a rate limiting role of vaterite dissolution. These contradicting findings are most probably caused by differences in aggregate density and surface area, of the starting materials used. This illustrates that the initial vaterite morphology can control the transformation rate of vaterite to calcite. Furthermore, it was shown that the transformation can be partly diffusion limited, which has not previously been described in the literature. When the transformation reaches ~60 wt. % of calcite, the transformation rate starts to decrease, because of annealing of the calcite crystallites into larger single crystals. This annealing causes a decrease of the calcite surface area, and, possibly, a change in growth mechanism due to the decreasing surface roughness.

Seeded calcite growth experiments were conducted at fixed pH (10.2) and two degrees of supersaturation (Ω = 4, 15), while varying the Ca^{2+} to CO_3^{2-} solution ratio over several orders of magnitude. The calcite growth rate and the incorporation of Sr in the growing crystals strongly depended on the solution stoichiometry. At constant degree of supersaturation, the growth rate was highest when the solution concentration ratio, r = [Ca^{2+}] / [CO_3^{2-}], equaled one, and decreased symmetrically with increasing or decreasing values of r. This behavior is consistent with the kink growth rate theory for non-Kossel crystals, assuming that the effective integration frequencies at kink sites are the same for the cation and anion. The Sr partition coefficient, D_{Sr}, ranged from 0.02-0.12, and correlated positively with the calcite growth rate.

The effect of the [Ca^{2+}] to [CO_3^{2-}] stoichiometric coefficient helps explain large variability in calcite growth rate equations proposed in the literature. A logical continuation of the work presented here would be to conduct variable [Ca^{2+}] to [CO_3^{2-}] ratio experiments at lower pH. The role of solution stoichiometry on calcite dissolution also deserves to be investigated.

A good example of ongoing research on the relation between growth rate and trace element partitioning in biomineralization, is strontium incorporation into the calcite of *Emiliania huxleyi*. Combining the knowledge obtained from inorganic precipitation with knowledge on cell physiological processes, it is possible to demonstrate that Sr incorporation in *Emiliania huxleyi* can not be explained solely on the basis of the calcite growth kinetics. Therefore, a conceptual model has been developed whereas fractionation occurs within the cell during Sr transport from seawater to the site of calcification (Langer et al., 2006a). Applying a similar approach we also demonstrated that Ca isotope fractionation in *Emiliania huxleyi* most probably also occurs during the transport through the cell (Gussone et al., 2006; Langer et al., 2006b).

Samenvatting en vooruitblik

Dit proefschrift gaat in op een aantal aspecten van kalkneerslag teneinde een beter begrip te krijgen van biomineralisatie. Na een inleidend eerste hoofdstuk wordt in hoofdstuk 2 de theorie van kristalgroei beschreven en geeft hoofdstuk 3 een overzicht van kalkachtige materialen.

In het tweede deel worden met name twee aspecten van het neerslaan van Calciet uit waterige oplossingen behandeld. In hoofdstuk 4 en 5 wordt het neerslaan van een voorlopige fase van het mineraal Vateriet onderzocht. Hoofdstuk 6 richt zich op de effecten van de stoichiometrie van de oplossing op de groeisnelheid van de kristallen en op de inbouw van Strontium.

De vorm van het Vateriet dat neergeslagen wordt bij CO_2 doorborreling van een oplossing van $CaCl_2$ is een framboosvormig aggregaat. Het blijkt zelfs onder volstrekt identieke omstandigheden niet mogelijk een reproduceerbaar aggregaat te verkrijgen. De dichtheid van de aggregaten en de afmetingen van de kristalletjes varieert sterk tussen verschillende experimenten. Deze verschillen bestaan in losser of vaster gepakte kristallen waardoor er een verschil in beschikbaar oppervlak is. De in deze studie beschreven Vateriet aggregaten kunnen zich in zichzelf geheel omzetten in Calciet. Voorts is aangetoond dat de omzettingssnelheid niet wordt begrensd door de oplosbaarheid van Vateriet in tegenstelling tot vermelding in de literatuur van een snelheidsbeperkende rol voor de oplosbaarheid van Vateriet. Deze tegenstrijdige bevindingen worden waarschijnlijk veroorzaakt door de aggregaatdichtheid en het specifieke oppervlak van het uitgangsmateriaal. Dit illustreert dat de initiële vorm van de Vateriet de omzettingssnelheid naar Calciet beïnvloedt. Bovendien is aangetoond dat de omzetting tevens ten dele begrensd wordt door de diffusiesnelheid in de oplossing. Dit is niet eerder beschreven in de literatuur.

Als de omzetting een waarde bereikt van ongeveer 60% Calciet begint de omzettingssnelheid af te nemen. Dit wordt veroorzaakt door rekristallisatie van de Calciet tot grotere kristallen wat een kleiner specifiek oppervlak tot gevolg heeft en tevens een afname van de oppervlakteruwheid.

Calciet groei experimenten met enten zijn uitgevoerd bij een vaste pH (10,2) en twee graden oververzadiging (Ω = 4,15), waarbij de ratio van Ca^{2+} tot CO_3^{2-} in de oplossing over enkele ordes van grootte gevarieerd werd. De groeisnelheid van de Calciet en de inbouw van Strontium hingen sterk af van de stoichiometrie van de oplossing. Bij een constant niveau van oververzadiging was de groeisnelheid het hoogst als de concentratieverhouding r=[Ca^{2+}]/[CO_3^{2-}] gelijk aan één was en de snelheid nam symmetrisch af bij zowel toename als afname van deze verhouding r. Dit gedrag voldoet aan de "Kink groeisnelheidtheorie van niet-Kossel kristallen", aannemend dat de effectieve integratie frequenties op "kink"-kristalposities gelijk zijn voor zowel positieve als negatieve ionen. De Strontium verdelingscoëfficiënt D_{sr} had een bereik van 0,02 tot 0,12 en kwam overeen met de Calciet groeisnelheid. Het effect van de stoichiometrische verhouding van [Ca^{2+}] tot [CO_3^{2-}] biedt een verklaring voor de grote verschillen in groeisnelheid van Calciet die in de literatuur vermeld worden.

Een logisch vervolg op de hier gepresenteerde studie is het onderzoek naar de invloed van verhoudingen [Ca^{2+}] tot [CO_3^{2-}] bij lagere pH. De invloed van de stoichiometrie van de oplossing verdient eveneens verder onderzoek. Een goed voorbeeld van onderzoek naar de relatie van groeisnelheid tot opname van spoorelementen bij biomineralisatie is onderzoek naar inbouw van Strontium in de Calciet. Combinatie van de kennis over anorganische neerslagen met kennis van celfysiologische processen maakt het mogelijk aan te tonen dat de inbouw van Strontium in *Emiliania huxleyi* niet alleen op basis van de kinetiek van de kristalgroei van Calciet kan worden verklaard. Hiertoe is een conceptueel model ontwikkeld waarin isotopen fractionering optreedt binnen de cel bij het transport van Strontium vanuit zeewater naar het punt van kristalgroei (Langer et al., 2006a). Met eenzelfde benadering wordt aangetoond dat Calcium isotopen fractionering zeer waarschijnlijk optreedt tijdens transport door de cel (Gussone et al., 2006; Langer et al., 2006b).

Zusammenfassung und Ausblick

Die vorliegende Arbeit befasst sich mit zwei Aspekten der Kalzitfällung aus wässriger Lösung. Im ersten Teil (*Kapitel 4* und *5*), wird die Umsetzung des Kalziumcarbonat Polymorphs Vaterit zu Kalzit näher untersucht. Im zweiten Teil der Arbeit (*Kapitel 6*) wird der Einfluss der Lösungszusammensetzung, genauer gesagt, der Kalzium zu Karbonat Stöchiometrie, auf die Fällungsrate des Kalzits und den Strontiumeinbau untersucht.

Vaterit, welcher durch das Einleiten von CO_2 in eine $CaCl_2$ Lösung gefällt wurde, bildet Aggregate deren Morphologie an das Aussehen einer Himbeere erinnert. Es ist allerdings nicht möglich, selbst bei identischen experimentellen Bedingungen, Aggregate mit identischer Morphologie zu fällen. Vergleicht man die Aggregate der unterschiedlichen Experimente, stellt man fest, dass die Dichte der Aggregate sowie die Größe der einzelnen Kristalle variiert. Die unterschiedliche Dichte der Aggregate führt zu großen Unterschieden in der spezifische Oberfläche.

Es konnte gezeigt werden, dass die Umsetzung des Vaterits zu Kalzit, im Falle der in dieser Studie benutzten Vateritaggregate, innerhalb der Aggregate selbst stattfinden kann. Weiterhin konnte gezeigt werden, dass die Umsetzungsgeschwindigkeit nicht, wie in einigen Studien behauptet, durch die Lösungsgeschwindigkeit des Vaterits limitiert wurde. Der Grund für die unterschiedlichen Ergebnisse, liegt sehr wahrscheinlich in den großen Unterschieden in der spezifischen Oberfläche der Aggregate. Dies veranschaulicht, dass die Morphologie des Vaterits, die Geschwindigkeit der Umsetzung zu Kalzit kontrolliert. Weiterhin konnte zum ersten Mal gezeigt werden, dass diese Umsetzung auch diffusionslimitiert sein kann. Wenn bei der Umsetzung ein Stadium erreicht ist, bei dem ~60% Kalzit vorhanden sind, sinkt die Umsetzungsrate. Dieses Absinken der Umsetzungsrate liegt daran, dass die einzelnen Kristallite miteinander „verschmelzen", was zu einer Verringerung der Oberflächenrauhigkeit des Kalzits führt, was wiederum möglicherweise eine Änderung des Wachstummechanismus zur Folge hat.

Kalzitfällungsexperimente, unter der Verwendung von Kalzitimpfkristallen, wurden bei konstantem pH (10,2) für zwei unterschiedliche Übersättigungen ($\Omega = 4$, 15) durchgeführt, wobei jedoch das Ca^{2+} zu CO_3^{2-} Verhältnis in der Lösung über mehrere Größenordnungen variiert wurde. Dabei hat sich gezeigt, dass die Wachstumsgeschwindigkeit des Kalzits sowie der Strontiumeinbau stark von der Lösungsstöchiometrie abhängen. Bei konstanter Übersättigung wurde die höchste Wachstumsgeschwindigkeit, bei einem $[Ca^{2+}]$ zu $[CO_3^{2-}]$ Verhältnis von $r = 1$ gemessen, wobei die Wachstumsgeschwindigkeit zu größeren und kleineren Werten hin symmetrisch abfiel. Dieses Verhalten ist in Einklang mit der für Nicht- Kossel-Kristalle vorhergesagten „Kanten"- Wachstumsrate, wobei davon ausgegangen wird, dass die effektiven Einbaufrequenzen an einer Kristallkante für Anionen und Kationen identisch ist. Der Verteilungskoeffizient für Sr, D_{Sr}, lag zwischen 0.02 und 0.12, und korrelierte positiv mit der Wachstumsrate.

Der beobachtete Effekt der $[Ca^{2+}]$ zu $[CO_3^{2-}]$ Stöchiometrie auf die Wachstumsgeschwindigkeit des Kalzits hilft die große Bandbreite der in der Literatur beschriebenen Ratengleichungen zu verstehen. Es ist nahe liegend die hier beschriebenen Fällungsexperimente durch Experimente bei geringerem pH zu ergänzen. Die Rolle des $[Ca^{2+}]$ zu $[CO_3^{2-}]$ Verhältnisses auf die Lösung des Kalzit sstellt ein weiteres, sehr interessantes, Untersuchungsgebiet dar.

Ein gutes Beispiel aktueller Forschung, welche den Zusammenhang zwischen der Wachstumsrate und dem Spurenelementeinbau im Rahmen der Biomineralisation untersucht, ist der Strontiumeinbau in den Kalzit welcher von *Emiliania huxleyi* gebildet wird. Durch die Kombination von Kenntnissen aus anorganischen Kalzitfällungsexperimenten, mit dem Wissen über zellphysiologische Prozesse, war es möglich zu zeigen, dass der Strontiumeinbau im Falle von *Emiliania huxleyi* nicht durch die anorganische Fällungskinetik erklärt werden kann. Daraufhin wurde ein Model entwickelt, welches darauf basiert, dass die Strontiumfraktionierung innerhalb der Zelle stattfindet, also während des Transports vom Meerwasser zum Ort der Kalzifizierung (Langer et al., 2006a). In einem ähnlichen Ansatz konnten wir zeigen, dass die Kalziumisotopenfraktionierung im Falle von *Emiliania huxleyi* sehr wahrscheinlich ebenso während des Transports durch die Zelle stattfindet (Gussone et al., 2006; Langer et al., 2006b).

Dankwoord

Bij het schrijven van dit dankwoord besef ik hoeveel mensen mijn werk en sociale leven (twee zaken die nauwelijks te scheiden zijn) beïnvloed hebben gedurende de tijd dat ik aan dit onderzoek gewerkt heb. Hoewel er veel mensen zijn die ik wil bedanken komt op de eerste plaats Kees van der Weijden. Hij is degene die het mogelijk maakte dat ik naar Utrecht kon komen wat geresulteerd heeft in dit proefschrift. Zonder zijn ideeen en inspirerende en kritische discussies zou dit proefschrift niet mogelijk geweest zijn. Zelfs na zijn emeritering ging deze ondersteuning onverminderd voort. In dit verband wil ik ook Philippe Van Cappellen bedanken voor de inspirerende contacten en de hulp die hij mij gedurende de laatste jaren bood.

Hoewel hij in een vroeg stadium van dit onderzoek vertrok wil ik Peter van der Linde bedanken voor de interessante brainstorms die aan onderzoek voorafgaan. Een zeer belangrijk figuur is Pieter Kleingeld. Zijn enthousiasme en interesse in welhaast elk technisch en wetenschappelijk onderwerp leverde veel inspirerende gesprekken waarvan ik heb genoten. Zijn technische ondersteuning maakte de experimenten die hier beschreven zijn mogelijk. Gedurende de experimenten was het ook goed te kunnen vertrouwen op de meetgegevens van Dineke van de Meent en Gijs Nobbe. Zoals ik hierboven al aangaf, is het niet mogelijk de wetenschap te scheiden van het sociale leven. Ik heb met veel plezier deelgenomen aan de koffie pauze. Hier bracht ik mijn eerste Nederlands in praktijk; een taal waarvan ik ben gaan houden.

Ik wil Niels Hartog bedanken voor de geweldige tijd die we samen gehad hebben.Veel collega's zoals Christof Meile, Mariëtte Wolthers en David Rodríguez Aguilera zorgden voor een goede herinnering aan de tijd die ik in Utrecht doorbracht. Helaas kan ik niet over iedereen uitweiden maar wil tenminste hun namen noemen: Katja Heister, Yvonne van Lith, Debby Los, Diana Menzel, Gert-Jan Reichart, Chris Spiers, Kagan Tuncay, Helen de Waard. Guus Loch zal ik zeker niet vergeten. Met hem mocht ik enkele excursies organiseren wat eveneens een prettige ervaring was. Pien van Minnen wil ik bedanken voor de steun bij de veelheid aan administratieve zaken die op mijn pad kwamen.

Toen ik voor het eerst in Nederland kwam werd mij een warm welkom bereid door mijn hospita Maria Vliegen. Zij maakte het mij makkelijk te integreren. Ook de anderen die ik daar ontmoette, Anika van 't Klooster, Michael Benndorf en Hongbo Li werden in de loop der tijd goede vrienden.

Ik verblijf alweer enkele jaren op het AWI in Bremerhaven waar ik mijn onderzoek heb afgerond. Graag bedank ik Jelle Bijma die mij hiertoe de tijd en gelegenheid bood. Met Gerald Langer besteedde ik vele avonden aan discussie over biomineralizatie die me enthousiast en geïnteresseerd hielden in wat ik aan het doen was. Maar ook anderen van het AWI wil ik noemen: Ina Benner, Friedel Hinz, Anja Terbrüggen, Silke Thoms, Dieter Wolf-Gladrow.

Tenslotte, degene die het meest dank toekomt is mijn Moeder. Zonder haar hulp had ik nooit een promotieonderzoek kunnen doen.

Curriculum Vitae

Gernot Nehrke werd op 14 september 1971 in Iserlohn, Duitsland geboren. Van 1981 tot 1986 bezocht hij de Haupt und Realschule in Wald Michelbach en van 1987 tot 1991 het Überwald Gymnasium aldaar. In oktober 1991 begon hij met de studie Mineralogie aan de Universität Heidelberg. De studie werd in 1996 afgerond met een onderzoek naar de callibratie van pyrolyse voor de bepaling van verschillende voorkomens van kwik in vaste stoffen en sedimenten. Van 1996 tot 1997 werkte hij als onderzoeksassistent bij Geomar in Kiel, waar hij deelnam aan de expedities naar de arctis ARK 13/2 en /3 met het onderzoeksschip "Polarstern". In 1997 begon hij als AIO bij de faculteit Aardwetenschappen van de Universiteit Utrecht waar hij werkte aan de verschillende aspecten van de Calcium Carbonaat vorming in waterige oplossingen. Van 2003 tot heden is hij medewerker van het Alfred Wegener Institut für Polar und Meeresforschung in Bremerhaven waar hij werkt aan biomineralizerings mechanismen van mariene calcifiërende organismen.